Search for Invisible Nucleon Decay in SNO+ with Improved Sensitivity

by

Lam Wheng-Kit, Ian

A thesis submitted to the
Department of Physics, Engineering Physics and Astronomy
in conformity with the requirements for
the degree of Doctor of Philosophy in Physics

Queen's University
Kingston, Ontario, Canada
October 2020

Abstract

The water phase of the SNO+ (Sudbury Neutrino Observatory) experiment has completed after the collection of ∼305 days of total livetime worth of data, divided into two main sets. The effective concentration of ^{238}U and ^{232}Th in the water was determined using *in situ* analysis to be, for the second set of data, $\mathrm{gU/gH_2O}$: $(3.64 \pm 0.74_{(\mathrm{stat})} + 1.28_{(\mathrm{syst})} - 0.99_{(\mathrm{syst})}) \times 10^{-15}$ and $\mathrm{gTh/gH_2O}$: $(3.08 \pm 3.22_{(\mathrm{stat})} + 1.60_{(\mathrm{syst})} - 5.00_{(\mathrm{syst})}) \times 10^{-16}$. The water data can also been used to search for "invisible" modes of nucleon decay, and a previous SNO+ publication set world-leading limits on relevant nucleon and dinucleon decay modes except neutron and dineutron decay. This thesis presents a re-analysis of the "invisible" neutron decay mode of that first set of data, which reoptimizes the fiducial volume and develops an improved treatment of the dominant energy systematic uncertainties. This leads to a world-leading lower limit on the "invisible" neutron decay lifetime of 6.91×10^{29} years. A sensitivity analysis shows that including the second set of data that has lower backgrounds is expected to yield a lower limit on the neutron decay lifetime of 1.57×10^{30} years, further improving the result.

Acknowledgments

Perfume and incense bring joy to the heart, and the pleasantness of a friend springs from their heartfelt advice.

Proverbs 27:9

There are many people that guided and supported me along this journey who I want to acknowledge. First and foremost, I would like to thank my supervisor Alex Wright, for taking me under his wing and guided me with utmost patience. My many discussions with Alex have enlightened me on a wide range of topics ranging from physics, to statistics, to chickens. Thank you for showing me what it means to be a physicist, a teacher, and a mentor. To say I learned a lot from you would be an understatement. I am truly fortunate to have you as my supervisor and friend.

I would also like to thank the rest of the SNO+ group at Queens for their guidance and friendship. Thanks Mark Chen for leading the group and for the summer parties! Thanks Peter Skensved, for the casual and technical/coding conversations. Special thanks to Herbert 'Gus' Shurvell from the Department of Art History and Art Conservation, whose guidance was instrumental in my work of developing XRF as a viable QA tool for SNO+. Special thanks to Chuck Hearns, who helped me out extensively in the machine shop. I would like to thank the rest of the SNO+ postdocs

and graduate students for making my time at Queens memorable: Szymon Manecki, Lianpeng Tian, Serena Riccetto, Benjamin Tam, Brian Krar, Mark Anderson, Yan Liu, Satoko Asahi, Ted Zhao, Caleb Miller, Daniel Bartlett, Liz Fletcher. I would also like to thank my office-mates for their company: Matthew Stukel, Alvine Kamaha, Sarah Olson, Dilraj Ghuman.

Being part of an international collaboration like SNO+ means that all our work is intertwined and contributed directly or indirectly to the success of this thesis. For that and for your friendship over the years, I extend a heartfelt thanks to the whole SNO+ collaboration. But I would like to acknowledge a few who were instrumental in the work presented in this thesis. I would like to thank Valentina Lozza for patiently guiding me in my internal backgrounds analysis. I wish to thank Morgan Askins, whose guidance on coding, statistics, and nucleon decay was invaluable for this thesis. A big thank you to members of the tellurium R&D team outside of Queens that I had the pleasure of working with: Lina Anselmo, Dimpal Chauhan, Oleg Chkvorets, Francine St. Jacques, and Doug Horne. Special thanks to Andy Stripay, Maggie Niro and Matt Depatie for introducing me to the wonders of breakfast at Eddies. On a separate note, I would like to thank Chris Jillings, who first hired me as a co-op student which began my exploration into the world of particle physics. I also would say a word of thanks to Nancy Brown, who made me feel at home whenever I am at Sudbury.

Outside of the particle physics circle, I would like to thank David Luong, for the many conversations over hotpot about literally every topic under the sun. Along with

Jeeyoung Nam, Kyunghoon Han, and Carlos Wang, thank you for your friendship since our University of Waterloo days. I also would like to thank my church community at St. Marks Lutheran Church, for their friendship and support throughout my time at Kingston. Last but not least, I would like to thank my family and friends back in Malaysia, who have been supporting me throughout my studies in Canada these past 11 years. Thank you to my parents for their support and encouragement throughout this endeavor. Thanks also to my church community in Malaysia, namely Uncle Wong Choong Meng, who kickstarted my Canadian journey. I am grateful for my girlfriend, Florence Aw. Thank you for your encouragements and being there for me all these years.

S.D.G.

Statement of Originality

Due to being a part of a large collaboration, the results described in this thesis required the efforts of many individuals. However, this thesis focuses on the areas where the author made important contributions.

The author led the internal backgrounds analysis (Chapter 4), with guidance and advice from other members of the collaboration. The nucleon decay analysis presented in Chapter 5 was based on a collaboration publication. However, improvements to the fiducial volume and treatment of the dominant systematics was the author's work, which led to a significant improvement over the published results. The author's work in developing a procedure utilizing XRF (Chapter 6) was an important contribution to the ultimate physics goal of neutrinoless double-beta decay search. It was initially developed in the early stages of tellurium loading research involving surfactants, of which the author also made important contributions (not described in this thesis).

Contents

List of Tables

List of Figures

Chapter 1

Introduction

We must take care of our garden...for when man was put into the garden of Eden, it was with intent to dress it: and this proves that man was not born to be idle.

Candide, Voltaire

Grand Unified Theories (GUTs) are theories that seek to unify the seemingly disparate electroweak and strong nuclear forces within a single framework described by a single Lagrangian. However, this idea of unification is not new. For example, in 1873, James Clerk Maxwell formally developed a mathematical framework unifying electricity and magnetism, demonstrating with the now well-known Maxwell's Equations that electricity and magnetism were different manifestations of the same physical phenomena [1]. In fact, the electroweak force is itself a unification of two seemingly different forces: electromagnetism and the weak nuclear force. This major accomplishment was achieved by Sheldon Glashow, Abdus Salam, and Steven Weinberg in 1968 [2]. The theory relied on the Brout-Englert-Higgs (BEH) mechanism of spontaneous symmetry breaking to explain the electroweak gauge boson masses, which in turn predicted a new particle, the Higgs boson [3], [4]. The Higgs boson was discovered in 2012 and thus provided the final confirmation of the electroweak theory [5].

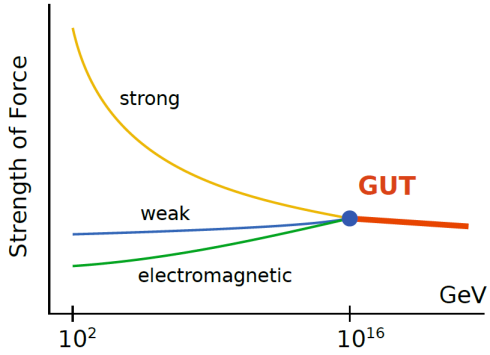

Figure 1.1: Running coupling constants converging at GUT energy [6].

As particle colliders probed higher and higher energies, it was noticed that the coupling constants that govern the strength of these interactions scale with energy (Chapter 94 of [7]). Since these coupling constants have been measured at various energies, it is possible to extrapolate them past current experimental energies, to see if they converge at any point ("unification energy"). Figure 1.1 illustrates this unification. From the plot, the predicted energy scale at which the three forces unify is at around 10^{16} GeV, which is called the 'Grand Unification scale'. According to Grand Unified Theories, when the temperature of the post-Big Bang Universe was greater than 10^{16} GeV, the three forces behaved as a single force. Currently, particle colliders are unable to probe particle interactions at the 10^{16} GeV level, as the most powerful colliders currently operate at the TeV level. However, many GUT models also predict lower energy phenomena, which allows them to be tested by current experiments.

There are numerous GUT models but a common feature is that they predict the decay of nucleons which is usually mediated by a hypothetical massive gauge boson. An interesting feature is that most these decays violate baryon number, which apart

from these theories is regarded as a conserved quantity at any particle interaction vertex [8], [9]. Some models predict that even though baryon number conservation is violated, the difference between baryon number (B) and lepton number (L) could be conserved, $\Delta(B-L)=0$ [10]. On the other hand, some processes like dinucleon decay (simultaneous decay of two nucleons) predict a baryon number violation of two units and leads to $|\Delta(B-L)|=2$ [11]. Baryon number violation is also a prerequisite to baryogenesis, a process that is assumed to have taken place in the early Universe resulting in the current imbalance of matter and antimatter [12]. In addition, baryon number violating processes are also key components for some theoretical extensions to the Standard Model, such as supersymmetry (SUSY) and effective field theory extensions that utilize extra dimensions [13]. Nucleon decay remains so far unobserved experimentally, with successive experiments having set increasingly stringent lower limits on the nucleon decay lifetime [14], [15]. Currently, the most sensitive lifetime limits come from water Cherenkov experiments, since they are easily scalable to the tonne-scale and can easily identify charged particles that could potentially be by-products of nucleon decay. These limits have excluded many GUT models ([16], [17]), but other GUT models remain viable, and experiments to continue to improve limits on nucleon decay are still considered important.

Most nucleon decay models predict the decay of the proton and bound neutron into visible products i.e. decay products that deposit energy into the detector, on the order of 1GeV [16], [15] . An example would be $p \rightarrow \pi^0 + e^+$, which is one of the favored proton decay modes by GUTs based on SU(5) symmetry [8]. An example Feynmann diagram of this process is shown in Figure 1.2. SuperKamiokande has

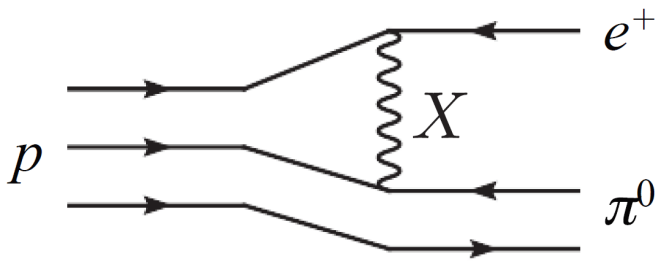

Figure 1.2: Feynmann diagram of a proton decay mode [18]. It should be noted that it is not always possible to draw Feynmann diagrams for every nucleon decay mode that obey conservation rules at each interaction vertex.

performed a search for this decay mode and has set a limit for this particular decay mode of 1.4×10^{34} years [19].

In addition, there are a class of decays called "invisible" nucleon decays predicted by some theories, where the decay products do not deposit their energy in the detector and escape detection, such as $n \to \bar{\nu}\bar{\nu}\nu$ [13]. To search for these types of decays, experiments would have to search for the de-excitation of the excited nucleus remaining after the decay which would mainly be gamma rays [20].

The SNO+ experiment operated as a water Cherenkov detector from May 2017 until December 2017. The experiment is located 2km underground, greatly reducing cosmogenic backgrounds. This allows SNO+ to set competitive limits on lower energy nucleon decay processes, specifically the so-called 'invisible' decay modes introduced above. A detailed description of the SNO+ experiment is given in Chapter 2, along with the other physics goals of the experiment. Chapter 3 describes the common steps in an analysis of the SNO+ data. Since nucleon decay is an extremely rare process, in order to carry out a competitive nucleon decay search, the backgrounds

in the detector have to be properly quantified and understood. A detailed analysis was performed by the author to this end, which is described in Chapter 4.

SNO+ has already published the results of a search for "invisible" nuclean decay modes, which saw world-leading lifetime limits on various "invisible" nucleon decay modes [21]. However, there were some modes, specifically "invisible" neutron and "invisible" dineutron decay, for which the published limits were not world-leading. For this thesis, the author took on the challenge of improving the lifetime limit for the "invisible" neutron decay mode culminating in a new world-leading limit set for this decay mode. This is described in detail in Chapter 5. Even though the focus was only on "invisible" neutron decay, similar gains are expected when this methodology is applied to the other "invisible" decay modes.

The long term plan for SNO+ is ultimately to look for another rare decay, neutrinoless double-beta decay. This is done by studying the decay of ^{130}Te loaded into liquid scintillator, which will replace the water in the detector volume of SNO+. The author developed a methodology to perform relatively quick checks for ^{130}Te in the liquid scintillator using X-Ray Fluorescence (XRF), which is laid out in detail in Chapter 6.

Chapter 2

SNO+ Experiment

Fantastic leaks and where to find them.

B. Tam, 2020

This chapter gives an overview of the SNO+ detector. A description of the detector hardware is given in Section 2.1, which will lead into an overview of the electronics and data acquisition systems in Section 2.2. This chapter concludes with a brief overview of the various operational phases of the SNO+ experiment, along with the physics goals for each phase in Section 2.3.

2.1 Hardware setup

Most of the current SNO+ detector setup was inherited from SNO [22]. The detector is located about 6800 ft (2 km) underground at Vale's Creighton Mine in Sudbury, Ontario, Canada. This provides about 6000 meters water equivalent (m.w.e.) of shielding from cosmic rays. With this shielding, only about 70 muons pass through the detector per day. For comparison, at sea level the rate is about 1 muon/cm^2/min [23].

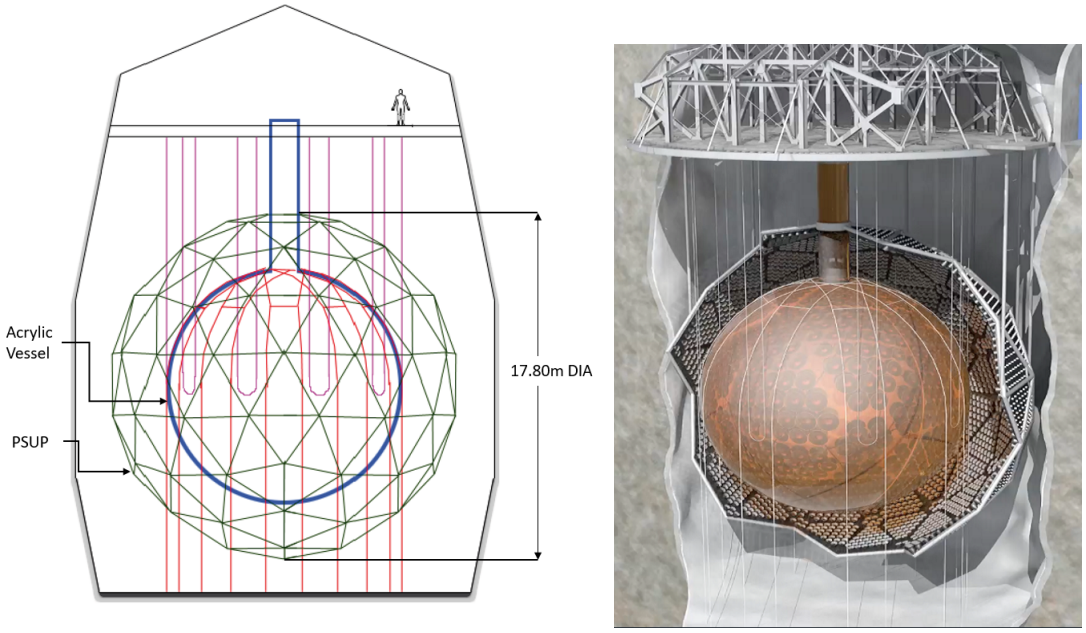

(a) Sketch of the detector setup

(b) Artist impression of the detector setup

Figure 2.1: The SNO+ detector

An image of the detector is shown in Figure 2.1(a). The active volume is contained within a 6m radius acrylic sphere with a 6.8m tall by 1.5m diameter neck. This AV is suspended from a deck at the top of a barrel-shaped cavity that is about 22m in diameter and 34m in height. About 2.9m away from the acrylic sphere is the photomultiplier tube (PMT) support structure (PSUP) which surrounds the whole acrylic vessel (AV). The PSUP is a geodesic structure about 17.8m in diameter and made of stainless-steel. As the name implies, it holds the PMTs in place, facing inward, around the acrylic vessel. A 27cm diameter light concentrator is attached to each PMT to improve light collection efficiency. The PMT-concentrator setup is secured to the PSUP using hexagonal acrylonitrate-butadiene-styrene (ABS) casings.

The bases of the PMTs are encased in plastic housings that are filled with silicone gel to make them water tight. The bases contains TNC connectors from which the signal/power cable can be connected to the electronics above on deck. There are about 9438 PMTs in total. During detector operations, the cavity below the deck and the volume between the PSUP and AV are filled with ultrapure water, about 7400 tonnes in total.

The gap between PSUP and AV is about 2.9m and the gap between the PSUP and cavity is about 2.1m. These gap sizes were chosen because they represent multiple scattering lengths of background gammas coming from the cavity rock as well as the PMTs themselves. Thus the water-filled gaps act as a shield against such backgrounds. As an example, the dominant background isotope is ^{208}Tl which decays into an excited state of ^{208}Pb, which then de-excites releasing four main gammas: 2.61, 3.20, 3.48, and 3.71 MeV. The mass attenuation coefficient of water, μ, for these gamma rays ranges from about 3.40×10^{-2} cm^2/g to 3.97×10^{-2} cm^2/g (going from low energy to high energy)[24]. Considering the density of water of 1 g/cm^3, and that the scattering length λ is related to the attenuation coefficient by $\lambda = \frac{1}{\mu}$, the scattering length of those gammas would be around 25-30 cm. Considering the gap distances mentioned above, a gamma would have to travel at least 7 times its scattering length in order to reach the PSUP from the cavity wall, and at least 9 times to get from PSUP to the AV. Thus, from this rough calculation, we can see that the water in those gaps provide good shielding from backgrounds coming from the cavity wall and the PSUP.

During SNO, due to the difference in density of the heavy water in the AV and the light water in the PSUP and cavity, AV hold-up ropes were used to support the AV. However, in SNO+, the AV will be filled with a type of mineral oil which will function as a scintillator. This creates the reverse problem, where the AV will be less dense than the surrounding water and hence buoyant. The solution is the reverse: hold-down ropes, which wrap over the top of the AV and are anchored into the cavity floor, were installed.

2.2 Electronics and Data Acquisition

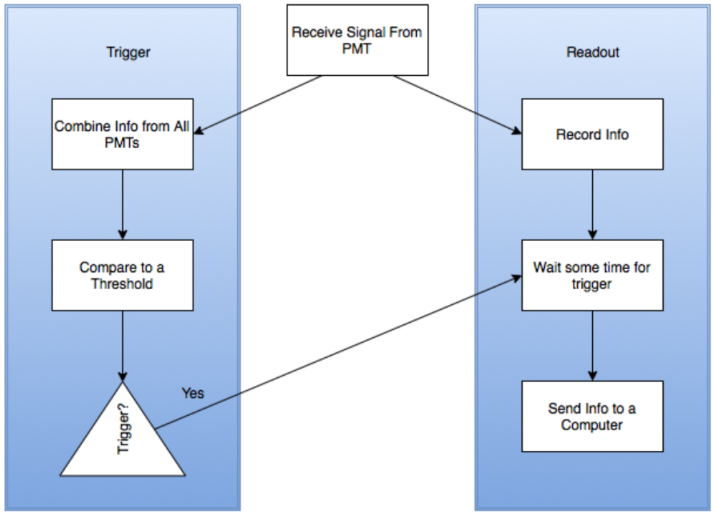

Figure 2.2: Overview of the trigger flow [25].

The overall data acquisition flow from the moment the PMTs detect photons to the recording of the data to disk is summarized in Figure 2.2. The rest of this section is dedicated to elaborating those steps in some detail.

2.2.1 Trigger

Data are recorded using a trigger on the number of PMT hits in an event. In other words, if some PMTs, N, fired within some time window of each other Δt, the event might be of interest and thus should be saved. The values for N and Δt are determined before-hand. Specifically, there are four main triggers for SNO+:

- NHIT100 (N100): Digital pulse that is about 100ns wide. The height of the pulse contributed by each fired PMT is equal. It counts the number of fired PMTs that exceeded the individual PMT threshold within a 100ns time window
- NHIT20 (N20): Similar to N100 but 40ns window instead of 100ns. In SNO, this was 20ns; it was increased to 40ns in SNO+, but the name was never changed.
- ESUMHI: A direct analog sum of the current pulses generated by each hit PMT that exceeded the individual PMT threshold. Therefore, the height of the final summed pulse is proportional to the deposited charge in the PMTs, with some amplification factor.
- ESUMLO: Similar to ESUMHI but with a lower amplification factor.

The transit time of a photon across the detector is around 80 ns so the NHIT100 will allow enough time for light from an event to propagate through the detector medium and contribute to the trigger signal. This is the main trigger for physics events in SNO+.

On the other hand, the NHIT20 signal is meant as more of a diagnostic tool. Keeping in mind the transit time of photons, it can be used to isolate events that happen

in a specific region in the detector by selecting light detected in a 40ns window. This region can be moved from the center of the detector by adjusting individual channel delays.

The two ESUM triggers differ in the amplification factor that is applied. ESUMHI is useful for detecting single photon events, since the high amplification can amplify the weak PMT pulse. Conversely, ESUMLO has a low amplification factor and is used when the PMTs see a very high charge that would saturate ESUMHI. This is useful for isolating electronic breakdowns, since those produce light well above the normal level for a physics event.

2.2.2 Readout

Various information of an event is recorded and stored in memory at the PMT channel-card until a detector trigger is given (or not). If a trigger is given, the event information is then taken from memory and sent to a computer to be written to disk. The main goal of the readout is to provide enough information for each trigger so that physics information can be determined such as particle energy, position, etc. In this regard, a balance has to be achieved between maximizing information and maintaining an achievable data rate. Therefore, the information that is read out from an event are:

- The time (relative to when the detector trigger was given) that the PMT channel threshold was exceeded.
- The size of the PMT pulse which is proportional to the charge and hence the

number of photons detected by that point and depends on length of integration times.

- The PMT identifier, which allows determination of the location of the PMT that got hit in detector space.
- The trigger types and its identifier (Global Trigger ID (GTID))
- The MTC/D Clock Time which is the time between events kept by the synchronous master 50MHz clock.
- The GPS Clock Time which is the absolute time of the event, which is obtained by interfacing and syncing with a GPS system.
- The digitized trigger pulses of ESUMLO events which are generated by a CAEN v1720 waveform digitizer.

2.2.3 Overview of electronics

What has been described so far has been the generation of a detector trigger and the recording of the information extracted from the PMTs. With over 9000 individual PMTs comes the Herculean task of recording information from all of them. This is the task of the electronics hardware which SNO+ inherited most of from the previous SNO experiment. There were some upgrades done for SNO+ in order to handle the increased data rate and light output in scintillator compared to water. Due to the different physics goals, some upgrades were done to parts of the hardware but in general, the data flow is the same.

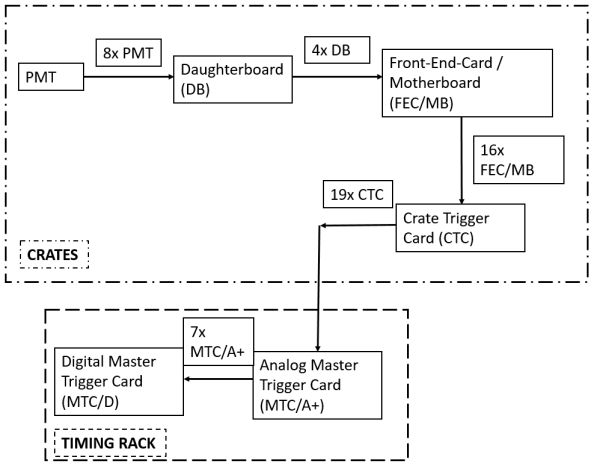

Figure 2.3: Summarizing the signal flow from PMT to data acquisition.

Figure 2.3 shows the data flow from the PMTs firing to when the data is sent to disk.

1. Daughterboards (DB): Sum PMT signals from 8 individual PMTs (i.e. 8 'channels') and generate ESUMHI, ESUMLO, NHIT20, NHIT100 pulses.

2. Front-End-Cards (FECs): Also known as Motherboards (MB), there are four daughterboards on each and they sum all the pulses from each daughterboard, generating summed ESUMHI, ESUMLO, NHIT20, NHIT100 pulses. 16 FECs are grouped into one crate.

3. Crate Trigger Card (CTC): Each crate has its own CTC and its main task is to perform another analog sum of the pulses from each FEC.

4. Timing Rack: Contains 7 Analog Master Trigger cards (MTC/A+). There is one for each of ESUMHI, ESUMLO, NHIT20 and NHIT100. Another three are dedicated to ESUMHI, ESUMLO and NHIT100 for outward looking PMTs

(OWLs), which are pointing outward to the cavity wall from the PSUP. They act as a muon veto system for SNO+. The MTC/A+ is upgraded from the SNO MTC/A in order to handle the increased currents due to higher light output in scintillator.

5. Digital Master Trigger Card (MTC/D): Also located on the timing rack, it takes the signals from each MTC/A+ via an analog-to-digital converter (ADC) and decides if they meet an event threshold. If they do, a global trigger (GT) is given by the MTC/D. A signal is sent to each CTC on the crates, which in turn tells the FECs on that crate to transmit the data held in memory to the XL3.

6. XL3: An interface board which sends the data via ethernet to a central DAQ computer (called the 'nearline') . This is an upgrade from the SNO XL2/1 system, improving the data transfer rate.

More details about electronics can be found in [22], [26], [27] and the SNO+ internal documents [28], [29], [25].

2.3 Phases and Physics Goals of SNO+

This section provides an overview of Cherenkov radiation, which is the detection principle in the water phase of SNO+. Besides nucleon decay, which has been covered in Chapter 1, this section will also give a brief overview of the other water physics goals of SNO+.

2.3.1 Water Phase

As of the writing of this thesis, SNO+ has completed Phase 1: the water phase. In this phase, the AV was filled with ultrapure water, which was the detection medium. The primary means of detection was via Cherenkov radiation, first observed by Pavel Alekseyevich Cherenkov in 1934 [30]. In usual energy loss of a charged particle (m_1) through a medium, it is assumed that m_1 interacts with only one other particle (m_2) at any given time, and the total energy loss is just integrating over many of these interactions along m_1's path. A quantity called the impact parameter, b, quantifies the linear distance between two interacting particles. In this scenario, it is assumed b is on the order of the size of an atom. However, in a dense media, there are many particles influenced by m_1's fields that collectively produce perturbing fields at m_2's location, which in turn modify m_2's response to m_1. This is known as the density effect, first theoretically studied by Fermi (1940). In other words, in dense media, the dielectric polarization of the material alters the fields of the interacting particles from their free-space/vacuum values to those similar to the case of macroscopic fields in a dielectric. The following equation describes the energy deposited by a charged particle as it travels in a dense medium:

$$\left(\frac{dE}{dx}\right)_{b>a} = \frac{2(ze)^2}{\pi v^2} Re \int_0^\infty i\omega\lambda^* a K_1(\lambda^* a) K_0(\lambda a) \left(\frac{1}{\epsilon(\omega)} - \beta^2\right) d\omega \qquad (2.1)$$

where z is the atomic number of the interacting atom, v is the incident particle velocity, ω is the frequency of the perturbed particle, $\epsilon(\omega)$ is the macroscopic dielectric constant, $\beta = \frac{v}{c}$, $\lambda = \frac{\omega^2}{v^2}\left[1 - \beta^2\epsilon(\omega)\right]$, K_0 and K_1 are modified Bessel functions [1].

If we consider the limit $|\lambda a| \gg 1$, the integrand in Equation 2.1 approaches:

$$\left(\frac{ze}{c}\right)^2 \left(-i\sqrt{\frac{\lambda^*}{\lambda}}\right) \omega \left[1 - \frac{1}{\beta^2 \epsilon(\omega)}\right] e^{-(\lambda+\lambda^*)a} \tag{2.2}$$

If λ is has a positive and real part, the expression will vanish exponentially at large distances. In other words, all the energy of the charged particle is deposited near its path. However, if λ is purely imaginary, then the exponential is unity and thus becomes independent of a. This means that some energy escapes away to large distances as radiation. Assuming $\epsilon(\omega)$ is real, λ is purely imaginary if $\beta^2\epsilon(\omega) > 1$. Rewriting this condition, substituting for the definition of β:

$$\begin{aligned} v &> \frac{c}{\sqrt{\epsilon(\omega)}} \\ &> \frac{c}{n} \end{aligned} \tag{2.3}$$

where $n \equiv$index of refraction$\equiv \sqrt{\epsilon(\omega)}$

Thus equation 2.1 can be reduced to the Frank-Tamm formula, used to describe the radiation first observed by Cherenkov:

$$\left(\frac{dE}{dx}\right) = \left(\frac{ze}{c}\right)^2 \int_{\epsilon(\omega)>(\frac{1}{\beta^2})} \omega \left(1 - \frac{1}{\beta^2 \epsilon(\omega)}\right) d\omega \tag{2.4}$$

From the derivations thus far, we can draw a couple of conclusions. First, the emission spectrum is not flat but rather peaked at higher frequencies below the regions where $\epsilon(\omega) > \beta^{-2}$. Together with the definition of λ earlier, this results in short emission wavelengths, which corresponds to the visible blue regime. Secondly, from Equation 2.3, we can see that this phenomena can only happen if the charged particle

is traveling faster than a certain velocity, the speed of light in that medium. If we consider an electron in water, which has an index of refraction of 1.33, this corresponds to about $2.2 \times 10^8 m/s$, which is about 0.25 MeV. In other words, the electron needs to have at least a kinetic energy of 0.25 MeV before it can emit Cherenkov radiation. This automatically provides a rejection to lower energy electrons. Finally, at large distances from the particle's path, the fields become transverse radiation fields, which form an angle relative to the particle's velocity, known as the Cherenkov angle θ_C. This can be derived from the equations above to be:

$$\begin{aligned} cos\theta_C &> \frac{1}{\beta\sqrt{\epsilon(\omega)}} \\ &> \frac{1}{\beta n} \end{aligned}$$

In water, this corresponds to $\theta_C = 41.2^o$ assuming $\beta \sim 1$. Qualitatively, this is like a 'sonic boom' of EM fields as the charged particle travels through the medium, which propagates as a forward cone of light.

For Cherenkov detectors like SNO+, the total number of Cherenkov photons detected in an event can be counted. From this total light yield, the energy of the incident particle can be estimated. Furthermore, the timing and pattern of the hit PMTs can be used to determine the position of the particle and the direction it was traveling.

In order for a Cherenkov detector to detect gamma radiation, the gamma must Compton scatter, off an electron in the water. The scattered electron then travels

through the water and emits Cherenkov radiation. The well-known Compton scattering formula is:

$$\lambda^{'} - \lambda = \frac{h}{m_e c}(1 - cos\theta) \tag{2.5}$$

where λ is the initial wavelength of the photon, $\lambda^{'}$ is the wavelength after scattering, h is the Planck's constant, m_e is the electron rest mass, c is the speed of light and θ is the scattering angle. We can rewrite this in terms of the energy of the photon. For a given incident photon energy, $E_\gamma = \frac{hc}{\lambda}$, the outgoing final state of the photon $E_\gamma^{'}$ can be written as:

$$E_\gamma^{'} = \frac{E_\gamma}{1 + (E_\gamma / m_e c^2)(1 - cos\theta)} \tag{2.6}$$

Maximum possible energy transfer happens in a head-on collision, that is, $\theta = 180^o$. In this case, the equation becomes:

$$E_\gamma^{'} = \frac{E_\gamma}{1 + (2E_\gamma / m_e c^2)} \tag{2.7}$$

From the earlier discussion of Cherenkov radiation, it was determined that in water, the minimum energy an electron has to have is about 0.25 MeV. We can now determine the minimum amount of energy a gamma needs to have in order to transfer that minimum amount to an electron, and thus determine the detection limit of a water Cherenkov detector. Due to conservation of energy, the energy lost by the gamma is transferred to the electron: $E_e = E_\gamma - E_\gamma^{'}$. Substituting $E_e = 0.25 MeV$ and $m_e = 0.511 MeV/c^2$ and solving the resulting quadratic equation yields $E_\gamma = 0.42$ MeV. Therefore, a gamma theoretically needs to have at least 0.42 MeV of energy

to enable a Compton scattered electron to generate Cherenkov radiation and thus be detected. In real life, these numbers will be different due to detector effects but this gives a good order of magnitude estimation of the detector's energy threshold.

Nucleon Decay

The main physics goal of Phase I was to set a limit on some potential nucleon decay processes. Due to the amount of water, and hence the number of nucleons, held in the AV, combined with low intrinsic backgrounds in the water, such a search was possible with sensitivities competitive with global best values. There are decay channels whose decay products deposit visible energy into the detector, such as $p \rightarrow e^+ + e^+ + \mu^-$. The strongest limits on these models are provided by the SuperKamiokande experiment which has 50 kt mass of water and very long exposure [15]. However, some theories predict the decay of nucleons into combinations of three (anti-)neutrinos [13]. SNO set a limit on these so called "invisible nucleon decay" modes (due to decay products not depositing visible energy into the detector but are made visible by the subsequent de-excitation of the daughter nucleus) [31]. However, being filled with heavy water, the solar neutrino neutral current/charged current interaction channels was a major background for nucleon decay search. In the current water phase of SNO+, those interaction channels were absent, and SNO+ could therefore set a better limit than SNO. This search is the major focus of this thesis, and is discussed in more detail in Chapter 5.

Reactor Antineutrinos

Another major physics goal in Phase I is to detect reactor antineutrinos. SNO+ is relatively close to three nuclear reactors at Pickering, Darlington and Bruce, as shown in Figure 2.4. This measurement utilizes the inverse beta decay (IBD) of antineutrinos onto water nuclei in the following reaction:

$$\bar{\nu_e} + p \rightarrow e^+ + n$$

The positron annihilates with energy $E_{e^+} \approx E_\nu - 1.8MeV$. The neutron then thermalizes before capturing on a proton with an average half-life of 200μs in the following process to form deuterium:

$$n + p \rightarrow d + \gamma(2.2MeV)$$

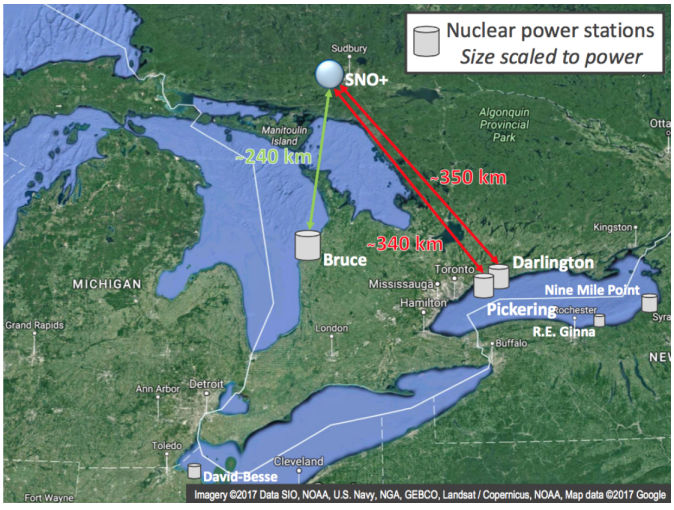

Figure 2.4: Figure shows location of SNO+ relative to the three nuclear reactors.

Due to the time correlation between the positron and the gamma, it is possible to perform a time coincidence search to look for such events. This time coincidence

enables high background rejection. The IBD process can only happen if the neutrino has energy greater than or equal to about 1.8MeV. This threshold is mainly due to the difference in mass between the products (e^+ and n) and the reactants ($\bar{\nu_e}$ and p). The main challenge of this measurement is the detection of the 2.2 MeV gamma. At this low energy, reconstructing the energy of the Compton scattered electron becomes challenging due to the low number of PMTs triggered. The expected interaction rate of reactor anti-neutrino events in the detector is 0.57 events/day, determined using world reactor power data with oscillations applied based on global best fits [32], [33], [34]. Calibration measurements have now demonstrated that SNO+ has good sensitivity to the neutron capture gammas [35].

Solar Neutrinos

It is also possible for SNO+ to measure something that is already relatively well-measured: solar neutrinos. Solar neutrinos are generated in nuclear fusion processes in the core of the sun, and the groundwork for the understanding of these processes was laid by Bahcall [36]. Figure 2.5 shows the various fusion processes in the sun. The ^{8}B solar neutrino flux has already been well measured by SNO and SuperKamiokande [37],[38]. Nevertheless, it is one of the physics goals of SNO+ to make such a measurement, with the aim to add an additional measurement to this quantity and improve the statistical uncertainties of the global average. Even though it is a well-understood measurement, there are not many large experiments capable of making such a measurement with comparable precision. The measurement has been completed successfully and the results have been published [39]. An improved analysis involving a lower

background data set is currently in the works.

Unlike SNO, SNO+ is only sensitive to the elastic scattering (ES) of neutrinos:

$$\nu_x + e^- \rightarrow \nu_x + e^- \tag{2.8}$$

where x is any one of the three neutrino flavors. Even though ES can be undergone by any of the three flavors of neutrinos, it is mainly sensitive to electron neutrinos; the interaction cross-section of electron neutrinos is about six times that of muon or tau neutrinos. This is due to the electron neutrino being able to interact via neutral current and charged current interaction, whereas the other two flavors can only scatter via neutral current. The ES process is highly directional, enabling analysis to show that the neutrinos are indeed coming from the sun.

The start of liquid scintillator filling on May 2019 officially marked the completion of phase I of SNO+. In addition, all the physics goals of this phase of SNO+ have been met. A paper for the nucleon decay search [21] and solar neutrino measurement [39] have been published, and as of the writing of this thesis, an antineutrino search paper is under internal review. The original duration of the water phase was supposed to be about 90 days. The duration of the water phase was about 2 years.

2.3.2 Phase II: Liquid Scintillator Phase

The liquid scintillator to be used by SNO+ is called linear alkylbenzene (LAB). It consists of a hydrocarbon chain attached to a benzene ring [41]. In the industrial

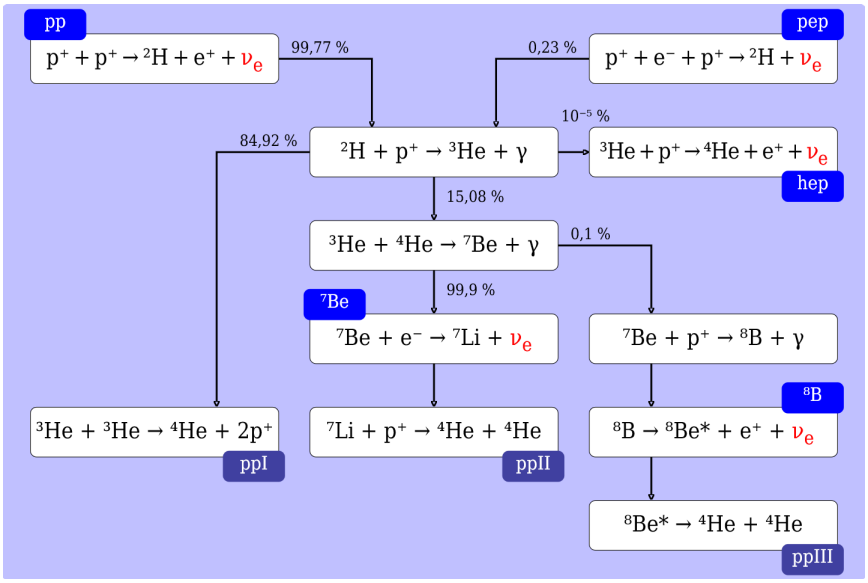

Figure 2.5: Proton-proton fusion chain of solar neutrinos. The neutrinos detected by SNO and in this phase of SNO+ are ^{8}B neutrinos. Neutrinos in the pep chain, are too low in energy for water Cherenkov detectors but could be detected with scintillators. Picture from [40].

sector, it is used as a base material for soaps and laundry detergents. In transitioning from water phase to scintillator phase, a 'displacement' method is used to fill the AV with liquid scintillator. Water is pumped out via a long pipe from the bottom of the AV while LAB is simultaneously added to the top. Due to the density difference between oil and water, the LAB will float on top of the water. This process is continued until the water in the AV is fully replaced with LAB.

Scintillation Mechanism

The mechanics of scintillation is described in detail in Birks [42] (Chapters 3 and 8) and Knoll [43] Chapter 8. The mechanism relies on the π-bonding between the

Figure 2.6: Graphic showing the plane where the π electrons sit relative to the benzene ring.

carbon atoms in the organic scintillator. The electrons involved in the π-bonds (π-electrons) form a delocalized electron cloud above and below the plane of the benzene ring, shown in Figure 2.6. Basically, the π-orbitals can be treated as orbitals of free electrons traveling in a one-dimensional loop around the molecular perimeter.

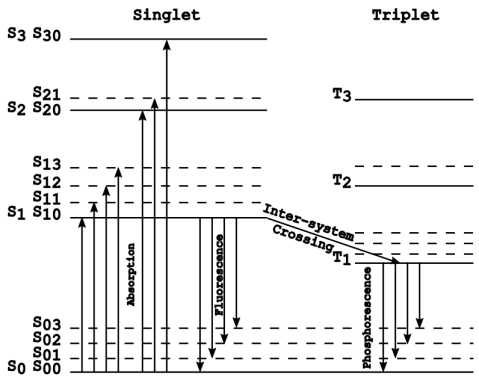

Figure 2.7: Pi-electronic levels of an organic molecule, along with the fluorescence, phosphorescence and delayed fluorescence decay channels. Taken from [42].

Figure 2.7 shows the π-electronic structure of an organic molecule, and a passing charged particle can excite this electronic configuration into any of a few configuration states. There is the spin-0 configuration state (singlet state) and its quantized energy

levels are labeled S_0, S_1, etc. The other configuration is the spin-1 state (triplet state) and its energy levels are labeled T_0, T_1, etc. Each state can be further subdivided into quantized vibrational states. For example, S_{01} would be the ground singlet state with first vibrational state. As the charged particle passes by, its kinetic energy is absorbed by the electrons which move into higher excited states (represented by upward arrows). States higher than S_1 then de-excite down to S_1 through non-radiative internal conversion, and any excited vibrational states also de-excite to zero state. The end result is a population of electrons in the S_{10} state. From here, the de-excitation to ground state S_{00} can take one of three paths, each emitting their own characteristic photons:

1. Prompt fluorescence: the electrons de-excite to one of the vibrational state of the ground electronic state (S_0). The de-excitation time is on the order of nanoseconds.

2. Phosphorescence: Through a mechanism called inter-system crossing, some excited S_{10} states can be converted into triplet states, which only then de-excite to the ground state. Because of this extra step, the de-excitation time is slower than prompt fluorescence, on the order of milliseconds. The wavelength of the photons emitted via this process is also longer than that of prompt fluorescence, due to the triplet state being on a lower energy level than the singlet state.

3. Delayed fluorescence: It is possible for the triplet state to be excited back into S_{10} state before de-exciting. The photons released in this process will be the same wavelength as those from prompt fluorescence but the de-excitation time will be longer.

It is worthwhile to note that the incident particle has to be charged in order for the excitation to occur, such as alpha and beta radiation. For gamma radiation, the gamma has to first interact with the electrons via the usual channels (photoelectric effect, Compton scattering, pair production); the resulting kinetic electrons excite the scintillator.

Physics Goal in Liquid Scintillator Phase

A major physics goal for phase II is to measure the reactor antineutrino flux, this time in liquid scintillator. Due to the dramatic increase in light yield due to scintillation light compared to Cherenkov light, the detection energy threshold is drastically lowered, enabling better detection efficiency of lower energy events and much better energy resolution. In particular, SNO+ would be able to better constrain the value of Δm^2_{12}, which is an important parameter in neutrino oscillation studies. According to the 2019 Particle Data Group update, there is a 2-σ tension between global solar neutrino data and KamLAND reactor data regarding the best fit of Δm_{12} [44]. SNO+ could contribute additional data in order to better understand this tension.

Another major physics goal is detection of pep solar neutrinos. From the solar neutrino production scheme in Figure 2.5, the pep solar neutrinos have a relatively low branching ratio (0.23%) compared to neutrinos coming from ^{8}B. From Figure 2.8, the ^{8}B neutrino energy spectrum is spread across a wide range of energies, whereas the pep solar neutrinos are monoenergetic at slightly higher than 1MeV. Such a search

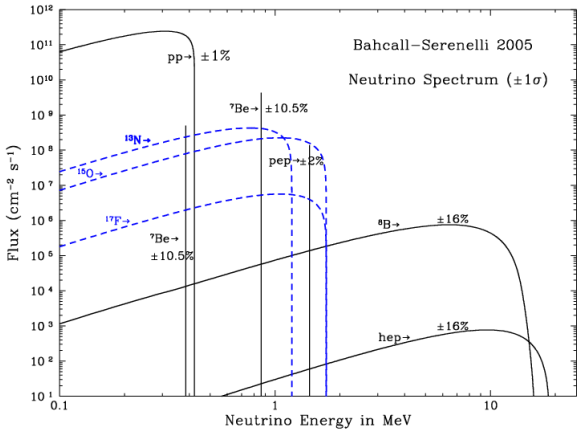

Figure 2.8: Solar neutrino spectrum as estimated by Bahcall.

would be feasible with liquid scintillators due to the high light yield per MeV of particle kinetic energy (around 550 photons/MeV) and low cosmogenic background rates in SNO+.

Due to the penetrating nature of neutrinos, it is possible to study the Earth's interior characteristics by studying the neutrinos that are emitted by processes in the interior. These "geo-neutrinos" are mainly generated by beta decay of ^{40}K, ^{232}Th and ^{238}U, making up almost all the radiogenic heat generated inside the Earth [45]. However, only geo-neutrinos from the beta decay of ^{232}Th and ^{238}U are detectable via inverse beta decay due to having energies above the 1.8 MeV threshold. By detecting and studying these neutrinos, various geological models can be constrained. Currently, there are two other large-volume liquid scintillator neutrino experiments that are capable of detecting geo-neutrinos: KamLAND [46] and Borexino, with Borexino publishing updated values in 2019 [45]. One major goal of the geo-neutrino measurements is to constrain the activity in the mantle, which involves subtracting off the

contribution from the local crust. Having multiple measurements in multiple places makes this easier. In addition, the local crust in Sudbury is the best understood in the world, which helps with local 'direct subtraction' [47].

Core-collapse supernovae (SNe) are among the most energetic astrophysical events in the Universe, releasing energy in the form of photons and neutrinos. However, the neutrinos from a SNe are expected to reach Earth several hours ahead of the photons, due to the neutrinos being able to penetrate out of the SNe core earlier than the photons. The recent SN1987A event was observed in both optical and neutrino channels. Observing SNes are important in the field of neutrino physics, as it is another method to address the long-standing problem of neutrino mass ordering in addition to aiding the study of neutrino oscillations and beyond Standard Model physics [48]. Therefore, the main goal is to detect the burst of neutrinos and determine the position of the SNe. To determine accurately if a supernova has occurred, observations from experiments located at different parts of the Earth are combined into an automated "supernova early warning system". Due to the arrival time delay of neutrinos and photons, this early warning system can provide valuable position information to optical telescopes. SNO+ will have the sensitivity to detect SNe neutrinos and contribute to this area of neutrino physics.

2.3.3 Phase III: Tellurium-Loaded Liquid Scintillator Phase

The major physics goal of this phase is the study of neutrinoless double beta decay ($0\nu\beta\beta$) using ^{130}Te. ^{130}Te is one of handful of isotopes known to undergo double-beta

decay ($2\nu\beta\beta$), a process in which the isotope undergoes beta decay twice simultaneously. For the case of ^{130}Te, the process proceeds as $^{130}\text{Te} \rightarrow {}^{130}\text{Xe} + 2e^- + 2\bar{\nu}_e$ with a Q-value of 2.53 MeV and a half-life of 8.2×10^{20} years. This process is rare due to the energetics of the decay. ^{130}Te has 52 protons and 78 neutrons, an even-even nucleus, which makes them more tightly bound due to pairing compared to odd-odd nuclei. If ^{130}Te were to undergo regular beta decay, it would become an odd-odd nucleus which is higher in energy. However, if the beta decay happened twice simultaneously, it would transform ^{130}Te into another even-even nuclei which is more stable, and this is what is observed. This process is of great interest because it provides a way to test the particle-antiparticle nature of neutrinos. In 1937, Ettore Majorana proposed that neutral spin-1/2 particles (i.e. neutral fermions) could be their own anti-particles. This is in contrast to Dirac fermions (named after Paul Dirac and satisfies the Dirac equation) where the particle and its anti-particle are distinct. If neutrinos are Majorana fermions, it is possible that $2\nu\beta\beta$ could occasionally proceed without the emission of (anti-)neutrinos, where the neutrinos are absorbed in an intermediate state, and the energy of the decay is carried away only by the two electrons. This is $0\nu\beta\beta$.

In this phase of the experiment, the liquid scintillator is mixed/loaded with an organic tellurium compound to enable the tellurium to mix homogeneously with the scintillator cocktail. Out of the handful of elements considered by SNO+ to search for neutrinoless double beta decay, tellurium was chosen due to a few factors. ^{130}Te has a relatively high natural abundance of 34%. As such, it does not have to be isotopically enriched. It is also optically transparent, which allows scintillation light

to reach the PMTs. SNO+ intends to load 0.5% tellurium by mass initially but has plans to increase the concentration, which highlights another advantage of this method: scalability.

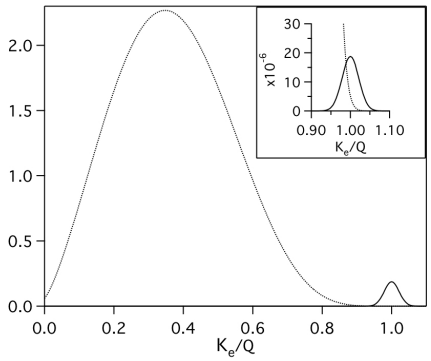

(a) Comparison of the peaks for $2\nu\beta\beta$ and $0\nu\beta\beta$. Inset shows the signals more realistically scaled. [49]

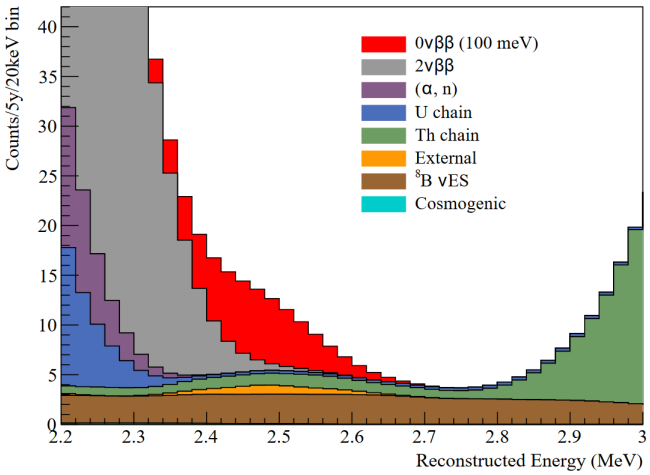

(b) Estimated signal and backgrounds from Monte Carlo, assuming 0.5% Te.

Figure 2.9: Expected signal for $0\nu\beta\beta$.

In terms of a signal, SNO+ expects to see a small bump at the end of a large two

neutrino double beta decay signal, shown in Figure 2.9(a). Figure 2.9(b) shows what SNO+ expects to see, if there is a detection. Current half-life limits are $> 4.0 \times 10^{24}$ years [50]. For reference, the $2\nu\beta\beta$ half-life for tellurium is 8.2×10^{20} years. Thus, this is a rare process on top of an already relatively rare process.

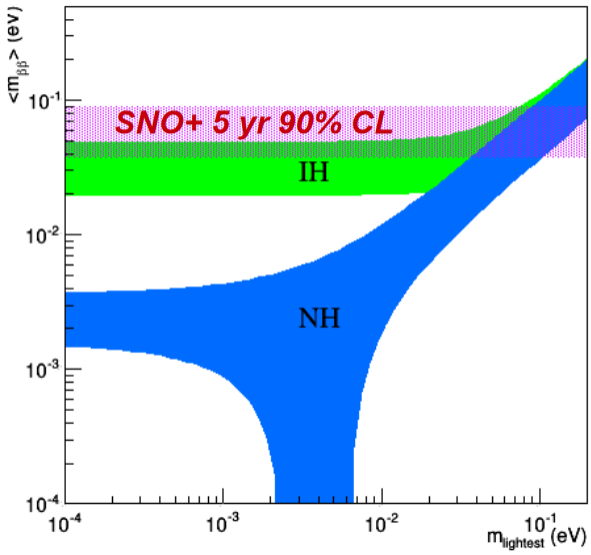

Figure 2.10: Allowed phase space of the effective Majorana mass as a function of the lightest neutrino mass using mass differences inferred from neutrino oscillation measurements [51].

Discovering $0\nu\beta\beta$ could also aid in determining the absolute neutrino mass scale. Figure 2.10 shows the phase space of possible effective Marjorana mass scale as a function of the lightest neutrino mass, depending on the mass hierarchy. At the target 0.5% Te concentration, SNO+ would be able to begin to probe the inverted hierarchy band. Increasing tellurium concentration would increase the experiment's sensitivity and exposure time, which will allow SNO+ to push further into the inverted hierarchy band. More detailed information can be found in [52], [53], [44].

Chapter 3

Introduction to SNO+ Analysis

Be aware and do not trust statistics in the tails of distributions.

Data Reduction and Error Analysis for the Physical Sciences; P.Bevington, D.K.Robinson

This thesis presents two distinct analyses: measurement of internal backgrounds and setting a limit on "invisible" neutron decay lifetime. This chapter describes the common steps in an analysis of the SNO+ data, and the analysis techniques used in both analyses.

3.1 Event reconstruction and data cleaning

Thanks to the properties of Cherenkov light described in Chapter 2, the number, and physical and temporal distribution of PMT hits associated with an event include enough information to allow the position, direction, and energy of an energetic electron to be reconstructed. However, not all reconstructed events are of interest as they could originate from unwanted physics processes, which would be backgrounds in our signal extraction. Such events are reduced in the data set by performing selection cuts on the reconstructed event classifiers to define a fiducial volume / region-of-interest.

The following list gives an overview of the common cuts applied to both analyses to reject mis-reconstructions and instrumental/electronics backgrounds. Other analysis-specific fiducial volume cuts are applied in addition to these, which will be elaborated in their specific chapters.

1. Valid fits (fitValid, waterFit): This checks if event reconstruction converged. It is possible for reconstruction to converge but give nonsensical results and so further selection cuts still have to be applied.

2. In-time hits ratio (ITR): Ratio of number of PMTs triggered within a set time window to the total PMTs triggered in an event. For example, instrumental background events tend to be spread out in time and thus give a lower ITR value.

3. inTimeHits100: the number of triggered PMTs that trigger N100 trigger within a 89ns window. The trigger thresholds were changed midway in the water phase (at run ID 104613). Runs before that run ID have a cut at inTimeHits100 $\geq$ 23. After that run ID, it is inTimeHits100 $\geq$ 10. These numbers were chosen based on a study [54] that shows the triggers being nearly 100% efficient with these cuts.

4. nhitsCleaned: number of PMTs triggered at least once in an event and pass the channel and hit cleaning cuts. This was set at nhitsCleaned $>$ 15, to reject low energy events.

5. data cleaning: even before reconstruction is performed, some events are flagged as background events based purely on PMT and timing information. These are

mainly aimed at flagging various unwanted instrumental backgrounds. Each event is flagged with a hexadecimal mask, which is then compared to in the analysis. For the record, the analysis mask used is 0xFB0000017FFE, the details of which can be found in [34].

3.2 Monte Carlo Simulations

In order to predict the expected distributions of the different signal and backgrounds in the different observables, Monte Carlo simulations of the various background and signal models are generated using GEANT4 (a simulation package developed at CERN) through a collaboration-developed wrapper called RAT (Reactor Analysis Tools) [55]. The RAT simulation includes full photon propagation, from generation via Cherenkov processes, through to detection on the PMTs. The detailed data acquisition and trigger systems elaborated in Chapter 2 are also part of the simulation. The decay schemes of all relevant background isotopes are also part of the simulation tool. In addition, several particle generators were developed to simulate other physics events which are backgrounds for the analyses such as solar neutrinos and reactor anti-neutrinos.

RAT communicates with a database that contains calibration constants and parameters describing the detector status during each run. This includes the optical properties of the water, PMT calibration constants, and detector settings such as channel thresholds. Algorithms have been developed to reconstruct event information such as the vertex position, event direction, and deposited energy. The SNO+ MC tool is continuously tuned to match newly available calibration measurements,

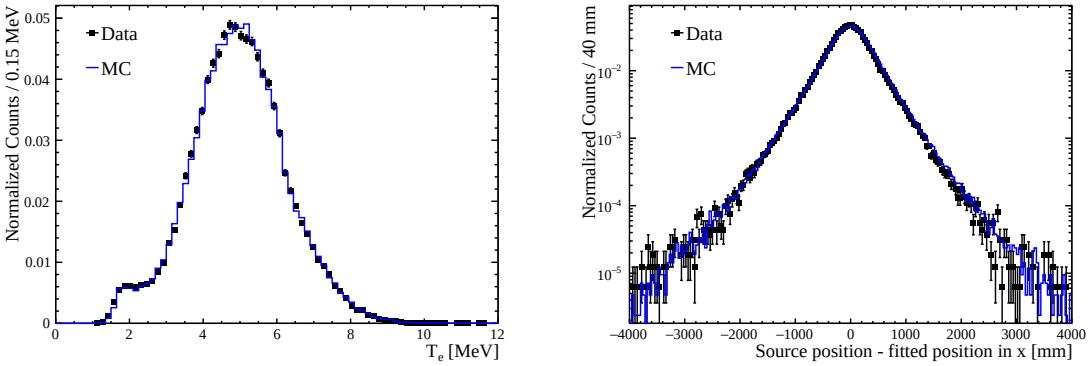

(a) Energy (b) Position

Figure 3.1: Example of data-MC comparison of ^{16}N calibration source used to tune and validate the MC [21].

such as with an ^{16}N calibration source, shown in Figure 3.1 [41].

Monte Carlo simulations of the signal and various backgrounds are used to form their corresponding probability density functions (PDF) by performing selection cuts and binning the surviving events in the various observable spaces. The data is treated with the same selection cuts and binning. The PDFs are then fit to the data in each observable space by minimizing the negative log likelihood and returning the number of events corresponding to each background. There are various backgrounds that fall under the category of 'external backgrounds' and these are combined into a single PDF with weights determined by a separate sideband analysis.

In addition to fitting, the MC simulations were also used to predict background rates in energy sideband analysis. An example would be the internal backgrounds measurements, which operated in an energy sideband [4-5 MeV] to the nucleon decay

region-of-interest (ROI) [5-10 MeV]. Analysis ROI cuts were performed on the simulations of the backgrounds (^{214}Bi and ^{208}Tl for the internal backgrounds) and the ratio of the surviving events to the total generated events is used as the extrapolation factor/detection efficiency of the specific background in the ROI. As in the case of PDF building, this requires sufficient simulated events such as not to be statistically limited.

3.3 Binned Maximum Likelihood Estimation

With a relatively clean data set now in hand and MC predictions of the signal and backgrounds PDFs, it is now possible to extract the signal of interest. Both analyses presented in this thesis utilizes binned maximum likelihood estimation and so a brief overview of that method is given in this section. The "likelihood" is defined as P(data;model) read as "probability of data given the model". The model that gives the highest likelihood for a data set is the most compatible with the data. Usually, the model is given as a probability distribution defined by one or more model parameters, where varying the parameters changes the model under test. Therefore, the goal of the maximum likelihood procedure is to find the set of parameters of a model that maximizes the likelihood compared to the data. For each data point, the probability of that data point given the model under test is computed and these are multiplied together to form the overall likelihood function, assuming each data point is independent from the rest. Mathematically, this is:

$$\mathcal{L}(\overrightarrow{x};\overrightarrow{\theta}) = \prod_{i=1}^{N} f(x_i;\overrightarrow{\theta}) \tag{3.1}$$

where we have a dataset of N data points $\overrightarrow{x} = (x_1, x_2, ..., x_N)$ which are assumed to follow a probablity density function $f(x_i; \overrightarrow{\theta})$. $\overrightarrow{\theta} = (\theta_1, \theta_2, ..., \theta_m)$ is a set of m unknown parameters to be estimated.

It is also useful to define the maximum likelihood estimators as the values of the parameters that globally maximizes the likelihood: $\overrightarrow{\hat{\theta}}$. In addition, the number of observations is itself a Poisson random variable i.e. if the experiment is repeated with identical conditions, the number of observed events N will fluctuate according to a Poisson distribution around the expected/true value ν. The likelihood function is then "extended" to be:

$$\mathcal{L}(\overrightarrow{x}; \nu, \overrightarrow{\theta}) = e^{-\nu} \frac{\nu^N}{N!} \prod_{i=1}^{N} f(x_i; \overrightarrow{\theta}) \tag{3.2}$$

For ease of computation, it is often desirable to work with the logarithm of the likelihood function, since the multiplication operations are converted into summations, and exponentials become simple factors. Therefore the extended likelihood function becomes:

$$ln\mathcal{L}(\overrightarrow{x}; \nu, \overrightarrow{\theta}) = -\nu + Nln\nu + \sum_{i=1}^{N} lnf(x_i; \overrightarrow{\theta}) \tag{3.3}$$

where constants not dependent on the parameters are dropped. In the case where the number of expected events is independent of the parameters $\overrightarrow{\theta}$ to be estimated, the estimated value is equal to the observed value i.e $\hat{\nu} = N$.

Computing the likelihoods for individual events can be computationally slow especially for large number of data points. It is possible to bin the data into a histogram to speed up this process. If the total number of events N is fixed, then the probability distribution for the bins is multinomial. The likelihood function is then:

$$\mathcal{L} = N! \prod_{i=1}^{B} \frac{P_i(\overrightarrow{\theta})^{n_i}}{n_i!} \tag{3.4}$$

where B is the number of bins and n_i is the number of entries in bin i. P_i is the expected probability for an event to appear in bin i and is defined as:

$$P_i(\overrightarrow{\theta}) = \int_{x_i^{low}}^{x_i^{up}} f(x; \overrightarrow{\theta}) dx \tag{3.5}$$

where x_i^{low} and x_i^{up} are the bin limits. In the extended likelihood case, a Poisson term for N observed events when ν events are expected is multiplied to the likelihood to give:

$$\mathcal{L} = e^{-\nu} \frac{\nu^N}{N!} N! \prod_{i=1}^{B} \frac{P_i(\overrightarrow{\theta})^{n_i}}{n_i!} = \prod_{i=1}^{B} e^{-\nu_i} \frac{\nu_i^{n_i}}{n_i!} \tag{3.6}$$

where the following substitutions were used in the last step: $N = \sum n_i$ and $\nu_i = P_i \nu$ such that $\sum \nu_i = \nu$. This can be interpreted to mean that the likelihood is the product of the bin-by-bin Poisson probabilities of observing n_i events in bin i when ν_i events are expected. As usual, it is convenient to work with the log likelihoods, which takes the form (dropping constants not dependent on the parameters):

$$ln\mathcal{L}(\overrightarrow{n}; \nu, \overrightarrow{\theta}) = \sum_{i=1}^{B} n_i \ln \nu_i(\nu, \overrightarrow{\theta}) - \nu \tag{3.7}$$

The analysis of the internal backgrounds performs a fit in one observable space.

However, the "invisible" neutron decay analysis performs fits in five observables. The idea behind fitting simultaneously in many observables is that the various backgrounds could be constrained by the data differently depending on the observable. For example, the ^{8}B solar neutrino background peaks in solar direction space but is indistinguishable from some of the other backgrounds in energy space.

In addition, some backgrounds can be constrained from independent measurements. The constraints are applied as a Gaussian penalty term multiplied to the overall likelihood function (i.e. added to the negative log likelihood). Therefore, the overall final log-likelihood function becomes:

$$ln\mathcal{L} = \sum_{i=1}^{N} n_i ln\nu_i(\nu, \overrightarrow{\theta}_b, \theta_s, \overrightarrow{\Omega}) - \nu_{tot} - \frac{(\overrightarrow{\theta_b} - \hat{\overrightarrow{\theta_b}})^2}{2\sigma_b} \tag{3.8}$$

where $\overrightarrow{\theta} = \theta_s + \overrightarrow{\theta_b}$ i.e. separating the signal and background parts, Ω represents the observables, ν_i is the expected value in each bin. The summation is over all bins. The first term in the summation represents the shape fit. The second term is the extended likelihood term i.e. the total expected number of events. The third term is for the constraints on some of the background parameters.

The fits were done using the ROOT software package, along with the RooFit analysis package, both developed at CERN [56], [57].

Chapter 4

Backgrounds in SNO+

The devil is in the details.

---

first heard from, A. Wright, 2016

Backgrounds are unwanted events (from physics processes or instrumental effects) that trigger the detector. In that regard, what constitutes 'background' and 'signal' depends on the experiment. As an example, SNO was studying ^{8}B solar neutrinos, which are backgrounds for most SNO+ physics programs. For the purposes of this thesis, the focus will be on the backgrounds in the water phase of SNO+, with particular focus on the backgrounds relevant to the nucleon decay search.

4.1 Internal Backgrounds in Water Phase

Internal backgrounds refer to the backgrounds due to trace radioactive impurities present in the actual detector volume and within the region of interest for the physics analysis. This is in contrast to external backgrounds, which are backgrounds that originate outside this volume, and will be addressed separately. The two main

sources of internal backgrounds are from the ^{238}U and the ^{232}Th decay chain. These isotopes and their daughters are naturally present in the environment (dust particles, etc), and physically removing them is key to reducing them. Both of these isotopes and some of their daughters have long half-lifes and would effectively be a constant source of background for the detector. Therefore, being able to measure the concentration of these isotopes in the water is important to inform of any leaks or breakdown in the purification system loop. In addition, these measurements serves as both an input and a cross-check for the nucleon decay analyses. In the latter, the maximum likelihood analysis floats these backgrounds as a parameter in the fit. In the case of the former, it is one of the inputs to the box counting analysis method, which is an independent analysis method which itself is meant as a cross-check to the maximum likelihood analysis.

To understand how the ^{238}U and the ^{232}Th decay chain are the main sources of background, we have to look at their characteristics and decay products. ^{238}U has a half-life of 4.47×10^{9} years and decays 100% of the time to ^{214}Bi after a few intermediate decays. ^{214}Bi is a relatively short-lived isotope with half-life of 19.9 minutes and decays 99.979% of the time via $\beta\gamma$ emission with a Q-value of 3.27MeV. A simplified ^{214}Bi decay scheme is shown in Figure 4.1. Measuring its activity and assuming secular equilibrium, one can get an estimate on the concentration of ^{238}U. Even though the Q-value of ^{214}Bi is outside the nucleon decay energy range (5-10MeV), the tails due to energy misreconstructions could fall within the nucleon decay energy range and therefore the contributions of ^{238}U in this regard must be estimated. However, care has to be taken in assuming secular equilibrium. ^{222}Rn is another daughter of

^{238}U which has a 4 day half-life, and is also abundantly present in the air. Therefore, any air leaks directly into the detector or water transport system could introduce ^{222}Rn and thus break secular equilibrium of ^{214}Bi with ^{238}U. Consequently, all ^{214}Bi activity is converted to an "effective" ^{238}U concentration. The target concentration of ^{238}U is 3.5×10^{-14} gU238/gH_2O, which was set based on levels achieved by SNO.

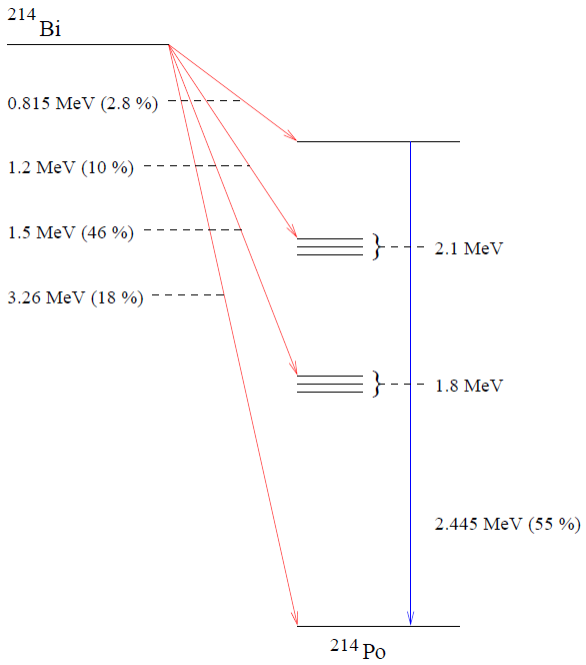

Figure 4.1: The ^{214}Bi decay scheme. Red lines indicate beta transitions and blue lines indicate gamma transitions. Taken from [58].

At this point, it is important to note the nitrogen cover gas system [59]. This system was designed in SNO (and used in SNO+) to fill the space above the liquid in the cavity and the detector with low-radon nitrogen gas. The purpose is to create a buffer against ^{222}Rn naturally present in the laboratory air from diffusing into the water. Because the Rn target in the SNO+ scintillator is below that achieved in SNO,

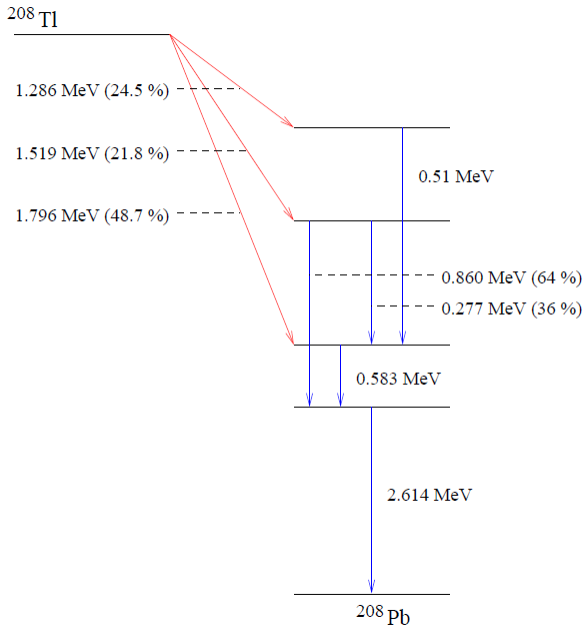

Figure 4.2: The ^{208}Tl decay scheme. Red lines indicate beta transitions and blue lines indicate gamma transitions. Taken from [58].

a new "sealed" cover gas system was designed for the AV in SNO+ [60]. The system was installed around September 2014 but wasn't fully commissioned and operational until August 2018 [61], [62]. Therefore, in the early part of the water phase, the AV cover gas was functioning at reduced efficiency, resulting in additional Rn in the water. This is the data set analyzed in this section of the thesis. However, the cover gas system was commissioned in August 2018, resulting in a significant reduction in the water background levels. The analysis of the resulting very low background data set will be explored in detail in Chapter 5.

^{232}Th is another long lived isotope at 1.40×10^{10} years half-life which goes through multiple decays into ^{208}Tl. In the water phase, the daughter nucleus ^{208}Tl is the one of interest as it β-decays with a half-life of 3.05 mins and with a Q-value of about

5.0MeV to ^{208}Pb. The decay scheme is shown in Figure 4.2. As with the case of ^{214}Bi, the energy tails of this decay could fall into the nucleon decay search region, and so the decay rate should be constrained via a sideband analysis. ^{208}Tl rates are normally quoted in terms of ^{232}Th concentration assuming secular equilibrium. The target concentration of ^{232}Th is 3.5×10^{-15} gTh232/gH_2O.

In order to estimate the concentration of ^{238}U and ^{232}Th, *ex situ* assays can be performed. The general idea of the *ex situ* assays is to chemically capture and concentrate a sample containing a daughter isotope of those chains through a multi-stage procedure. The activity of the sample is then measured. It would be desirable to perform an *in situ* assay which can be used as a cross-check and as a more regular check of the parent isotope concentration, as the *ex situ* assays are performed relatively infrequently.

Fortunately, it is possible to use the SNO+ detector itself to count and separate the two isotopes. As only the "tails" of the ^{214}Bi and ^{208}Tl spectra enter the analysis energy region, it is challenging to separate these based on their energy since the spectral shape of these two isotopes look similar in energy space. The basic idea is that we can utilize the difference in isotropy of Cherenkov light produced by the decay of ^{214}Bi and ^{208}Tl in order to estimate their activity. As mentioned above, ^{214}Bi decays nearly 100% of the time via β-decay. About 19% of those decays involve decaying directly to the ground state of ^{214}Po. The rest of the time, it decays into an excited state of ^{214}Po which de-excites releasing gammas of various energies. However, most

of these gammas are low energy, below the minimum amount to emit Cherenkov radiation via Compton scattering. Therefore, the Cherenkov light emitted would be due only to the β, for which the triggered PMTs would form a single ring pattern. On the other hand, ^{208}Tl always β-decays into an excited state of ^{208}Pb which de-excites via γ emission. The energies of the γ's in this process are mostly above the Cherenkov threshold and thus generate Cherenkov radiation via Compton scattering, along with the β emitted in the initial decay. Thus, the light detected in the event would be smeared out by the superposition of multiple rings. Therefore, the light from ^{208}Tl decay is more isotropic than that from ^{214}Bi decay.

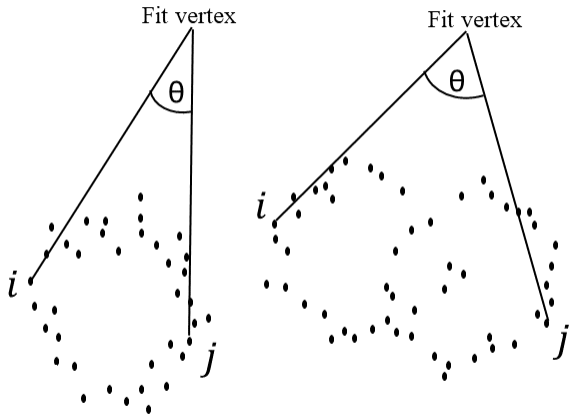

Figure 4.3: Sketch of layout and parameters used in calculating β_{14}.

This difference in Cherenkov light isotropy for the two parent nuclei was exploited in SNO to perform *in situ* water assays. To quantify the isotropy of light, a classifier called β_{14} was developed and is re-implemented for SNO+ [63], [64]. It is a linear combination of Legendre polynomials of the 1st and 4th order, which themselves are

functions of the angles between triggered PMTs in an event. Figure 4.3 gives a rough sketch of the layout. The formula is:

$$\beta_{14} = \beta_1 + 4\beta_4, \text{where } \beta_l = \frac{2}{N(N-1)} \left[\sum_{i=1}^{N-1} \sum_{j=i+1}^{N} P_l(cos\theta_{ij}) \right] \tag{4.1}$$

where N is the number of triggered PMTs, and Figure 4.3 shows how the angles are determined, and i and j sum over the pairs of triggered PMTs. A more isotropic event would have larger values of θ and thus lower value of β_{14} as demonstrated in Figure 4.4.

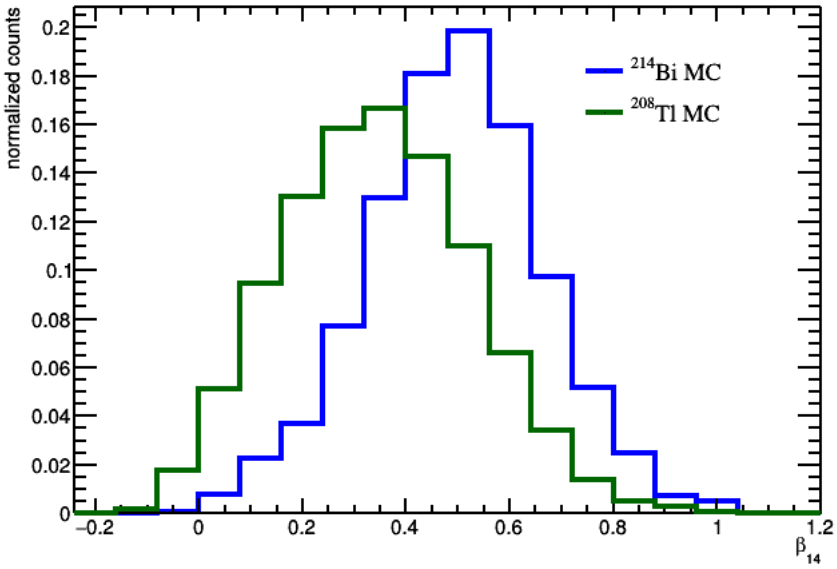

Figure 4.4: β_{14} MC spectra of ^{214}Bi and ^{208}Tl decay.

4.2 Internal Backgrounds: *In situ* analysis

An *in situ* energy sideband analysis of the internal backgrounds was done by the author in order to determine the internal background rate. This information was

used as a check of detector water cleanliness, as well as an input to the nucleon decay analyses. The classifier β_{14} was used to discriminate between ^{214}Bi and ^{208}Tl. It was assumed that these were the two dominant internal backgrounds, an assumption that will be addressed shortly. Due to the absence of the cover gas in the first data set, the background activity varied during this time. Therefore, this first data set was split into six time periods where the background rate was more or less stable, shown in Figure 4.5. These "time bins" were analyzed individually for ^{214}Bi and ^{208}Tl activity. Not shown in Figure 4.5 is the low background data set with the operational cover gas system, labeled 'time bin 7'. Due to some slight differences in the analysis method, the analysis of time bin 7 is covered separately in Section 4.4.

A binned maximum likelihood fit of the Monte Carlo to the data was performed in β_{14}-space. The fit parameters are then converted into ^{214}Bi and ^{208}Tl activity, which is then converted into ^{238}U and ^{232}Th concentration. The number of expected events in the nucleon decay region of interest is then extrapolated from this number via Monte Carlo.

4.2.1 Event selection

For the water phase data, a blinding scheme was implemented that blinded events that are above nhit 39 from analysis. However, a portion of the data (about first 13 days) was left completely unblinded in order to perform verification checks and determining selection cuts. The energy and radial position selection cuts for the internal backgrounds analysis were determined by varying a specific selection cut (say energy)

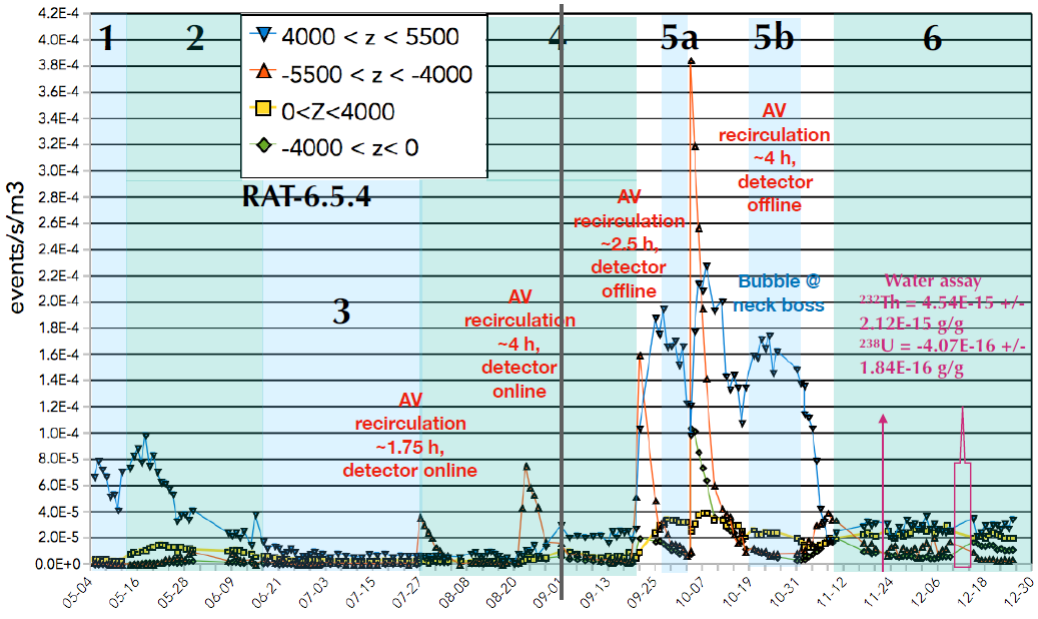

Figure 4.5: The event rate in the SNO+ detector as a function of time. Looking at the yellow squares and green diamonds, which together monitors a 4m radius around the center of the detector, we can see that even though the event rate of the outer regions of water varies considerably, that region is more or less steady. The time bins are labeled 1,2,3,4,5a,5b,6. Taken from [34] Section 8.4.4.

of both data and Monte Carlo while keeping the others fixed. The Monte Carlo pdfs are then fit to the data, and the χ^2/DoF was noted each time. A larger deviation of the χ^2/DoF from 1 would indicate that the Monte Carlo is not fully describing the data and hence hint at contamination from external backgrounds. Table 4.1 and Table 4.2 show the results of varying the energy cut, and Table 4.3 and Table 4.4 show the results of varying the radial position cut. The final selection cuts were settled based on a balance of dataset purity and number of events to achieve sufficient statistics. The position selection cuts was also corroborated with detailed event rate monitoring based on reconstructed position by Lozza (SNO+ collaborator) [34]. In Figure 4.5, it was shown that an internal region of the detector stayed relatively constant even

though the rate of a more outer region of the detector fluctuated wildly (recall the lack of cover gas mentioned previously).

Lower E cut (MeV)	events/yr ^{214}Bi	events/yr ^{208}Tl	χ^2/D.o.F.
4.0	$(3.57 \pm 0.46) \times 10^7$	$(6.07 \pm 2.50) \times 10^5$	13/12
3.5	$(4.97 \pm 0.32) \times 10^7$	$(4.72 \pm 1.85) \times 10^5$	21/12
3.0	$(6.58 \pm 0.32) \times 10^7$	$(4.86 \pm 1.80) \times 10^5$	24/12

Table 4.1: Time bin 3 results of fits as the lower energy cut is reduced in 0.5 increments for posz ≥ 0.

Lower E cut (MeV)	events/yr ^{214}Bi	events/yr ^{208}Tl	χ^2/D.o.F.
4.0	$(4.19 \pm 1.80) \times 10^6$	$(1.21 \pm 1.11) \times 10^5$	4/12
3.5	$(4.43 \pm 1.12) \times 10^6$	$(2.67 \pm 0.76) \times 10^5$	16/12
3.0	$(7.43 \pm 1.12) \times 10^6$	$(2.82 \pm 0.74) \times 10^5$	13/12

Table 4.2: Time bin 3 results of fits as the lower energy cut is reduced in 0.5 increments for posz < 0.

Radial cut (mm)	events/yr ^{214}Bi	events/yr ^{208}Tl	χ^2/D.o.F.
4000	$(3.85) \times 10^7$	$(1.37) \times 10^6$	1.32
4500	$(5.49) \times 10^7$	$(2.30) \times 10^6$	1.55
5000	$(8.76) \times 10^7$	$(3.80) \times 10^6$	1.88
5500	$(1.36) \times 10^8$	$(7.22) \times 10^6$	3.29

Table 4.3: Fit results with increasing radial cut for posz > 0, using runs 102800-103338. Energy cut is fixed at 2.0 MeV.

Table 4.5 summarizes the event selection cuts used for each time bin. The 'top' and 'bottom' of time bin 2 refers to the top half and bottom half of the detector, respectively and this is reflected in the z position cut column (z-cut). The upper

Radial cut (mm)	events/yr ^{214}Bi	events/yr ^{208}Tl	χ^2/D.o.F.
4000	$(1.50) \times 10^7$	$(6.35) \times 10^5$	2.20
4500	$(2.00) \times 10^7$	$(9.18) \times 10^5$	3.10
5000	$(3.52) \times 10^7$	$(1.08) \times 10^6$	3.61
5500	$(6.86) \times 10^8$	$(1.40) \times 10^6$	5.61

Table 4.4: Fit results with increasing radial cut for posz < 0, using runs 102800-103338. Energy cut is fixed at 2.0 MeV.

energy cuts were chosen to match those required by the nucleon decay box analysis, which in turn was obtained by a "box optimization" procedure. This procedure, done by Askins [65], seeks to maximize the signal-to-background ratio in the nucleon decay ROI by adjusting the thresholds on energy, $\cos\theta_{sun}$ (angle of event relative to the sun) and radius. However, the radial cut in Table 4.5 was chosen specifically for this internal background analysis to exclude external background contamination.The z-position cut was chosen to exclude particular regions of the detector that had higher event rate due to Rn ingress (known internally as "hotspots").

Timebin	Energy	z-cut	Livetime (days)
1	<5.75	z <4000	5.05
2 (top)	<5.95	z $\geq$ 0	14.85
2 (bottom)	<5.45	z $<$ 0	14.85
3	<5.85	-	30.68
4	<5.95	z >-4000	29.44
5	<5.85	z <0	11.54
6	<6.35	-	23.19

Table 4.5: List of time bin specific cuts for **internal background box**. A lower energy cut of 4.0MeV is also applied for all. In addition to the cuts above, cuts that are common over all time bins are: valid fit, valid waterFit, itr >0.55, nhitsCleaned $\geq$ 15, inTimeHits100 $\geq$ 10 (runID $\geq$ 104613), inTimeHits100 $\geq$ 23 (runID <104613), posr <4300.

4.2.2 Contamination

It is possible for other sources of events to show up in the internal backgrounds ROI that are not accounted for in the internal background fit (recall the fit only fits for internal Bi and Tl). A MC study was used to estimate the number of such events to fall into the internal backgrounds ROI. The class of events considered are events originating from the AV and ^{8}B solar neutrino events.

AV events

These events come from U and Th decays on the inner surface of the AV. These events would normally be rejected by the selection cuts. However, misreconstruction of the event classifiers can cause some events to fall into the internal backgrounds ROI. A MC study was performed in order to estimate the amount of contamination in the internal background region. The selection cuts of time bin 3 was chosen and applied to MC events of Bi and Tl on the AV surface to obtain the fraction of AV events that would fall into the internal backgrounds ROI. Bonventre [34] performed a likelihood-based fit to determine the rate of surface AV Bi and Tl events. In particular, for time bin 3, the following results were obtained:

- ^{214}Bi AV: $(1.54 \pm 12.4) \times 10^{7}$ counts/year
- ^{208}Tl AV: $(0.00 \pm 1.96) \times 10^{5}$ counts/year

Using the MC of the AV events, the number of events expected in the internal backgrounds ROI is estimated to be:

- ^{214}Bi AV: 0.61 ± 4.90 events

- ^{208}Tl AV: 0.00 ± 0.14 events

Therefore, the total number of AV events in the internal background region would be 0.61 ± 4.90. The total number of data events in the internal backgrounds region for this time period was 156 events. Therefore, about (0.39 ± 3.14) % of data events could be due to events on the surface of the AV. The large uncertainty is due to the systematics associated with the fits done in [34]. Therefore, the contamination is negligible within the uncertainties. Similar levels were seen in all the other time bins leading to the conclusion that the contamination in the internal backgrounds ROI is negligible overall.

Solar neutrino events

Another source of background contamination are the solar neutrinos events (^{8}B neutrinos). Solar neutrinos events are expected to have a distribution pointing at $cos(\theta_{sun})$ = 1, while the background events are expected to have a flat distribution in $cos(\theta_{sun})$. Again, a MC study was used to estimate the contamination level in the internal backgrounds region of interest. As before, the cuts for time bin 3 were used. From the MC events, the number of expected solar neutrino events are (taking oscillations into account):

- ν_e solar : 1.49 ± 0.04 events
- ν_μ solar : 0.50 ± 0.01 events

This gives a total of 2.00 ± 0.04 events expected in time bin 3. Again, there were a total of 156 events in this time period, which gives a contamination level of (1.28

$\pm$ 0.03) %, which is negligible.

In summary, the contamination of events from the acrylic vessel and solar neutrinos into the internal backgrounds region of interest is negligible. Therefore, it is reasonable to just consider Bi and Tl in the fits.

4.2.3 Results

The selection cuts were applied to both data and MC (except data cleaning, which was not applied to MC, since the MC does not simulate all the possible instrumental noise). Both were binned into histograms in β_{14}-space. The MC is then fitted to the data using maximum likelihood method in ROOT, and the results were converted into Bi and Tl activity in the full detector using MC cut efficiencies. This activity was then converted to equivalent U and Th concentrations assuming secular equilibrium. The shift-and-refit method as elaborated in the following subsection was applied to obtain the systematic uncertainties, and the statistical uncertainties were taken from the fit results. A plot of one of the time bins is shown in Figure 4.6 and the numerical results of all timebins are shown in Table 4.6.

4.2.4 Systematic Uncertainties

The systematic uncertainties that were taken into account in the analysis are:

- Uncertainty in energy scale

Time bin	Concentration	
	$g^{238}U/gH_2O$ $[\times 10^{-13}]$	$g^{232}Th/gH_2O$ $[\times 10^{-15}]$
1	$(1.89\pm0.18_{(stat)}+0.38_{(sys)}-0.37_{(sys)})$	$(5.85\pm5.18_{(stat)}+4.03_{(sys)}-10.1_{(sys)})$
2 (top)	$(4.82\pm0.30_{(stat)}+1.16_{(sys)}-1.00_{(sys)})$	$(34.5\pm13.6_{(stat)}+11.2_{(sys)}-43.6_{(sys)})$
2 (bot)	$(0.35\pm0.09_{(stat)}+0.09_{(sys)}-0.07_{(sys)})$	$(2.73\pm4.17_{(stat)}+1.27_{(sys)}-4.32_{(sys)})$
3	$(0.86\pm0.07_{(stat)}+0.24_{(sys)}-0.16_{(sys)})$	$(8.32\pm3.12_{(stat)}+3.02_{(sys)}-10.27_{(sys)})$
4	$(1.93\pm0.09_{(stat)}+0.58_{(sys)}-0.44_{(sys)})$	$(9.43\pm4.10_{(stat)}+6.48_{(sys)}-20.53_{(sys)})$
5	$(5.32\pm0.37_{(stat)}+1.94_{(sys)}-1.42_{(sys)})$	$(29.0\pm17.1_{(stat)}+24.7_{(sys)}-67.8_{(sys)})$
6	$(6.72\pm0.21_{(stat)}+2.62_{(sys)}-2.07_{(sys)})$	$(67.1\pm10.0_{(stat)}+38.7_{(sys)}-95.7_{(sys)})$

Table 4.6: Results from time bins 1-6.

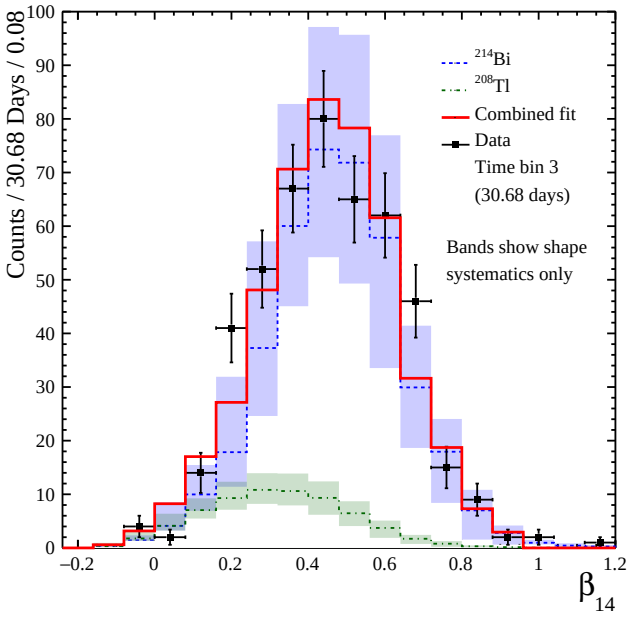

Figure 4.6: Plot showing the fit results in β_{14}-space for time bin 3. The colored bands only show the effect of the systematics on the PDF-shapes and do not reflect the absolute magnitude of the systematics.

- Uncertainty in energy resolution
- Shift in β_{14}
- Uncertainty in trigger efficiency cut

- Uncertainty in $cos\theta_{sun}$
- Radial position scale uncertainty
- Radial position resolution uncertainty
- Radial position shift uncertainty

Since the AV is shifted upwards with respect to the PSUP center, the reconstructed position coordinates (given in the PSUP reference) have been transformed to AV coordinates: posz' = posz$_{PSUP}$ - 108 mm. The new posz' was then used to calculate a new posr'. All the coordinates in the internal backgrounds section are given in the AV reference frame. Also, a low-energy correction was done on all the events to correct the energy reconstruction. The effect was more pronounced on events at lower energies.

The general idea in evaluating each systematic is to shift the parameter in question by 1σ of the associated systematic uncertainty and perform the analysis cuts and fits. The difference in the fit results from the case where no systematic was applied is taken as the systematic uncertainty. In the subsections that follow, the nucleon decay (ND) region-of interest (ROI) values are given alongside the values for the internal backgrounds ROI as they are used to determine the systematic uncertainty associated with the extrapolation of the internal backgrounds into the ND ROI, which is described in a later section in this chapter.

Energy scale and energy resolution

In order to estimate the energy scale and resolution uncertainty, Lebanowski and Luo utilized the ^{16}N calibration data and Monte Carlo [66]. MC simulations of pure electrons were performed in order to get a spectrum of the reconstructed electron energy. This spectrum is convolved with a Gaussian which is then fit to the ^{16}N calibration data and MC independently. The parameters of the Gaussian were allowed to float in the fit. The difference in the fitted mean and sigma of the Gaussians between MC and data, along with fit uncertainties, was taken as the systematic on the energy scale and resolution, respectively for mean and sigma. Since the ^{16}N calibration was performed in various parts of the detector, the detector was divided up into regions in order to perform a volume-weighted estimation. More details can be found in [66] and [34].

The energy scale uncertainty was determined to be 2.0% for the nucleon decay region-of-interest (ROI) and 1.4% for the internal water [66]. Using the appropriate number, the energy of the Bi and Tl MC events was scaled up and down event-by-event. After scaling, the MC was used to re-build the PDFs, and the fit was repeated. The difference in the fit result from the case using unshifted MC is taken as the systematic.

Similarly, the energy resolution uncertainty was evaluated based on information in [66]. The method to apply this systematic was to shift the energy of the MC event-by-event by a random number chosen from a Gaussian with mean, $\mu = 0$ and width, $\sigma = \sigma_E * \sqrt{(1+\delta)^2 - 1^2}$, where $\sigma_E = \sqrt{E}$ and E is the energy of that particular

event after the low energy correction, and δ is 0.018 for the ND ROI and 0.011 for internal water region. As before, the difference from the unsmeared case is taken as the systematic uncertainty.

β_{14} shift

Bayes compared the difference in β_{14} between the data and MC of ^{16}N calibrations [67]. A plot of this comparison for the central N16 run (source at center of the detector) is shown in Figure 4.7. From the plot, the difference in the mean between data and MC is -0.0310±0.0042. In order to evaluate the systematic associated with β_{14} shift, the upward shift was done using only +0.0042 and the downward shift was done using -0.0310-0.0042. This was applied as an absolute shift event-by-event on the Bi and Tl MC for both the internal backgrounds and ND ROI. The shifted MC was then fitted to the data and any difference from the unshifted case was taken as the systematic.

Uncertainty in trigger efficiency

This was applied based on work done by LaTorre and Kaptanoglu [68], [54], [34]. This was only applied to time bin 3, since the predetermined inTimeHit100 cut for this time bin did not make the triggers 100% efficient based on laser timing calibration data, but is 100% efficient based on Nhit monitor and laserball analysis. inTimeHit100 is checked event by event and an appropriate weighting is applied for events with inTimeHit100 of 23,24,25. For inTimeHit100>25, the triggers are 100%

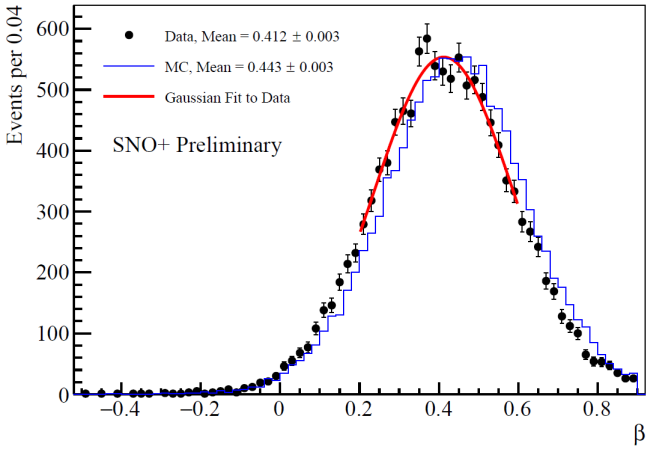

Figure 4.7: Plot from Bayes for central N16 run. The data points are black dots and the corresponding MC is the blue histogram. Red line is the Gaussian fit to the data. Taken from [67].

efficient so a weight of 1 was applied. This applies to both the internal backgrounds and ND ROI.

Radial Position uncertainties

Following work done by Leming [69],[34], the systematic uncertainties were given independently in the x,y,z coordinates. An important note is that for the nucleon decay analysis, these position uncertainties are applied only at the final limit-setting stage to avoid double counting. Since the cut is done in radius, the uncertainties are first combined using the following formula:

$$\sigma_r = \sqrt{\sigma_x^2 + \sigma_y^2 + \sigma_z^2}$$

To determine the position systematics, as in the case of energy, a data-MC comparison of the ^{16}N calibration data was performed in position-space for each source deployment position. The MC was convolved with a Gaussian, with the mean representing the average offset of data and MC, and the sigma representing the resolution of the reconstruction algorithm. In addition, there is an additional systematic due to a potential bias in the actual source deployment position in the detector. This is represented as a position scaling which is determined to proportional to the distance of the reconstructed event from the center of the detector.

For *radial shift* uncertainty, the numbers were given in actual position units. For the upward shift, $(posr + \sigma_r)$ was done event-by-event. Likewise, for the downward shift, $(posr - \sigma_r)$ was done instead.

For *radial resolution smearing* uncertainty, the σ_r was computed first as above. Then a random number was picked from a Gaussian with mean=0 and with width given by σ_r. This number is then applied as a shift event-by-event i.e. $(posr + \sigma_r)$. However, this is treated as a two-sided uncertainty, where the final result is applied as both an upper and lower uncertainty.

For *radial scaling* uncertainty, the scaling itself had a radial dependence. To properly take this into account, the uncertainties were combined with the following uncertainty instead:

$$\sigma_r = \frac{x^2\sigma_x^2 + y^2\sigma_y^2 + z^2\sigma_z^2}{r^2}$$

Parameter	Uncertainty
x shift (mm)	+16.4 / -18.2
y shift (mm)	+22.3 / 19.1
z shift (mm)	+38.1 / -16.7
x scale (%)	+0.91 / -1.01
y scale (%)	+0.92 / -1.02
z scale (%)	+0.91 / -0.99
x resolution (mm)	104
y resolution (mm)	98.2
z resolution (mm)	106.2

Table 4.7: Position systematics, taken from [69]. They are applied to both the internal backgrounds and ND ROI.

For the internal backgrounds analysis, the numbers used are summarized in Table 4.7.

Direction systematic

Again, using the ^{16}N calibration source, a systematic on the reconstructed event direction can be determined. This was performed by Leming [69],[34]. The internal backgrounds analysis does not utilize reconstructed direction or quantities that derive from it, such as $cos\theta_{sun}$ i.e. the angle representing the direction of the event relative to the sun. However, it does come in later in determining the extrapolation from the internal background sideband into the nucleon decay region of interest, since nucleon decay uses the solar angle as a fit observable. From [69], the value determined was +0.08/-0.13 %. More details are available in [69],[34].

4.2.5 Fitter Validation

In order to validate the fitter, the bias and pull from an ensemble of fake data sets were calculated and plotted. To generate a single fake data set, the binned MC

of both Bi and Tl was scaled to some expected value and then Poisson-fluctuated bin-wise. The resulting data set is then fit to the unfluctuated PDFs of Bi and Tl. The difference of the fit result from the expected value is taken as the *bias*. The ratio of the bias to the 1σ fit uncertainty returned by ROOT is taken as the *pull*. An unbiased fitter would return a bias distribution with a Gaussian centered around 0, and the pull distribution would be a standard normal distribution. The bias and pull distribution of both the Bi and Tl parameters are shown in Figure 4.8 and Figure 4.9. From both sets of figures, we can see that the bias and pull distributions are as expected, giving confidence that the fitter is working properly.

4.2.6 Extrapolating into Nucleon Decay Region of Interest

A MC based study was used to estimate the fraction of internal background events that is expected to fall into the nucleon decay region of interest (ROI), which was used as an input to the counting analysis. The counting analysis counted the number of events that fell within a determined ROI. The amount of various class of backgrounds that fell into this ROI was then subtracted from the total events and the number of remaining events was used to set an upper limit on nucleon decay. One of these background classes was the internal backgrounds and in this application, there was no need to distinguish between Bi and Tl events, since only the total is relevant. However, as mentioned in at the beginning of the chapter, the discrimination was useful as a determination of background contributions in the detector, as well as a cross-check for the nucleon decay likelihood analysis, since the internals are floated independently in the likelihood. In addition, the scaling factor for both Bi and Tl

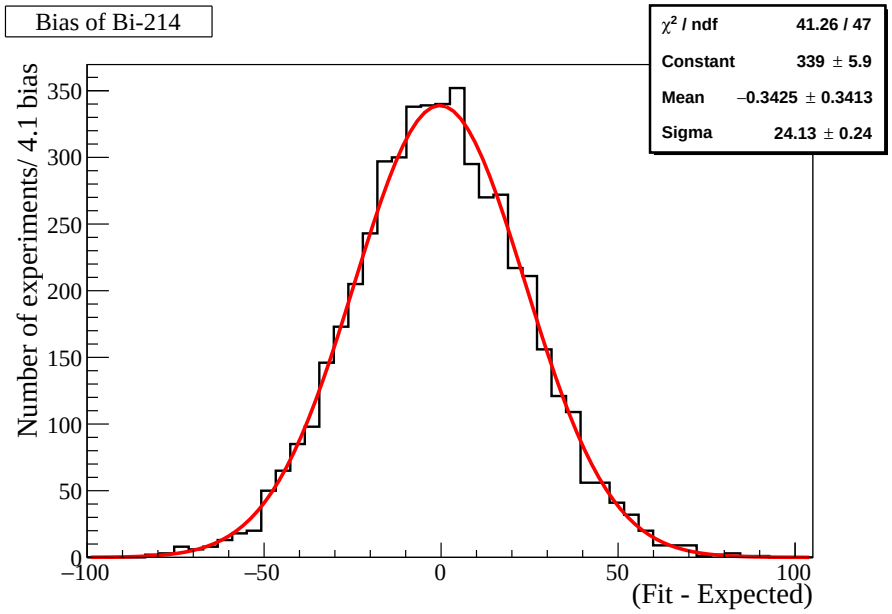

(a) Bias distribution for Bi-214

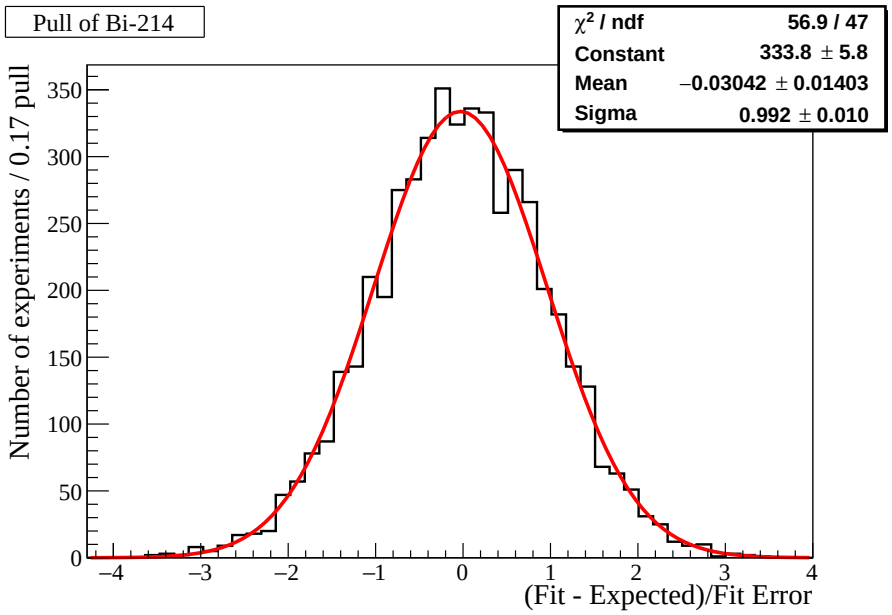

(b) Pull distribution for Bi-214

Figure 4.8: Bias and pull distribution of the ^{214}Bi fit parameter for 5000 fake data sets. The Gaussian fit is shown in red, with the fit results displayed on the plots.

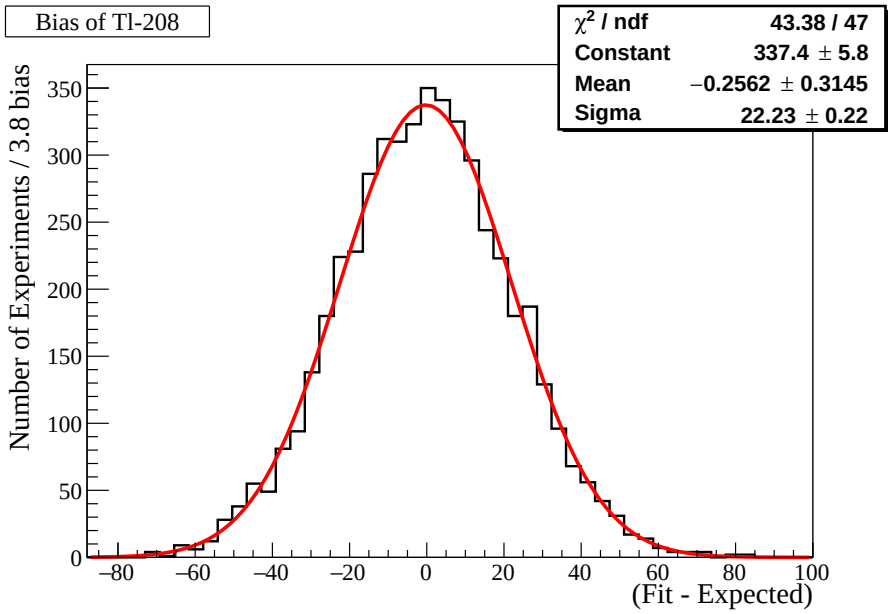

(a) Bias distribution for Tl-208

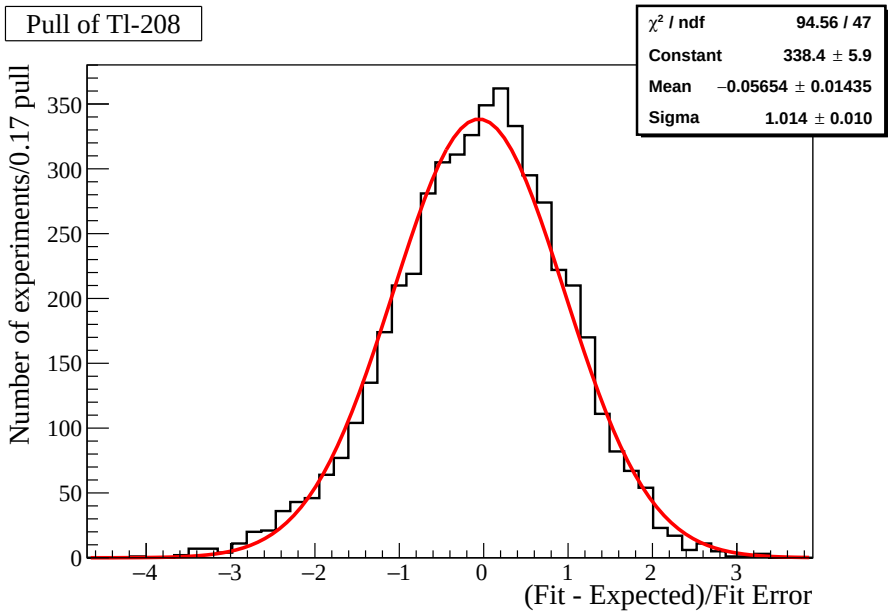

(b) Pull distribution for Tl-208

Figure 4.9: Bias and pull distribution of the ^{208}Tl fit parameter for 5000 fake data sets. The Gaussian fit is shown in red, with the fit results displayed on the plots.

were different, which means that without separating the U and Th contributions, it would not be possible to perform the extrapolation. The topic of nucleon decay, as well as an analysis based on maximum likelihood is explored in greater extent in Chapter 5.

The MC events (which were simulated for all energies) were selected based on the selection cuts listed in Table 4.8. An extrapolation factor was calculated as the ratio of MC events surviving the cuts to the total MC events. This extrapolation factor is then used to determine the number of internal background events in the stated ROI. The results of this extrapolation is shown in Table 4.9. In the results, the statistical uncertainty is a combination of the counting statistical uncertainty and the fit uncertainty from the internal backgrounds analysis. The systematic uncertainty is obtained using the same shift method outlined in the previous section. However, the systematics in this case is due to the shifting/smearing moving events in or out the ROI, which would change the extrapolation factor.

Timebin	Energy	Posr	Sunct	Z-cut	Livetime (days)
1	>5.75	<5450	>-0.80	z <4000	5.05
2 (top)	>5.95	<4750	>-0.75	z $\geq$ 0	14.85
2 (bottom)	>5.45	<5050	>-0.75	z <0	14.85
3	>5.85	<5300	>-0.65	-	30.68
4	>5.95	<5350	>-0.70	z >-4000	29.44
5	>5.85	<5550	>-0.80	z <0	11.54
6	>6.35	<5550	>-0.70	-	23.19

Table 4.8: List of timebin specific cuts for the **ND ROI box**. An upper energy cut of 9.0MeV is also applied for all. In addition to the cuts above, cuts that are common over all time bins are: valid fit, valid waterFit, itr >0.55, nhitCleaned $\geq$ 15, inTimeHits100 $\geq$ 10 (runID $\geq$ 104613), inTimeHits100 $\geq$ 23 (runID <104613), -0.12 $<\beta_{14}$ <0.95.

Time bin	Events in ND ROI [counts]	
	^{214}Bi	^{208}Tl
1	$0.313\pm0.04_{(stat)}+1.24_{(sys)}-1.22_{(sys)}$	$0.029\pm0.001_{(stat)}+0.013_{(sys)}-0.048_{(sys)}$
2 (top)	$0.361\pm0.11_{(stat)}+1.48_{(sys)}-1.47_{(sys)}$	$0.071\pm0.008_{(stat)}+0.24_{(sys)}-0.26_{(sys)}$
2 (bot)	$0.229\pm0.025_{(stat)}+0.73_{(sys)}-0.73_{(sys)}$	$0.042\pm0.002_{(stat)}+0.064_{(sys)}-0.089_{(sys)}$
3	$0.545\pm0.086_{(stat)}+2.51_{(sys)}-2.49_{(sys)}$	$0.139\pm0.008_{(stat)}+0.33_{(sys)}-0.37_{(sys)}$
4	$0.800\pm0.150_{(stat)}+2.58_{(sys)}-2.56_{(sys)}$	$0.106\pm0.007_{(stat)}+0.108_{(sys)}-0.245_{(sys)}$
5	$0.465\pm0.12_{(stat)}+2.05_{(sys)}-2.02_{(sys)}$	$0.108\pm0.008_{(stat)}+0.103_{(sys)}-0.253_{(sys)}$
6	$0.392\pm0.180_{(stat)}+2.46_{(sys)}-2.42_{(sys)}$	$0.187\pm0.022_{(stat)}+0.218_{(sys)}-0.333_{(sys)}$

Table 4.9: Results from time bins 1-6, counts in the ND ROI. Numbers are corrected for the live time of the particular time bin.

4.2.7 Comparing ex situ assays with in situ analysis

Due to the variation with time of the internal backgrounds (mainly due to Rn contamination), a comparison with the ex-situ assays (Ra and Rn) is only possible if they are taken in the same period. Details of the assay technique are given in [34]. In the middle of timebin 6, two ex-situ assays (Ra and Rn) were conducted. These numbers can be used as a cross-check of the internal backgrounds analysis. Unfortunately, it was determined by the assay group that the Rn assay had too many potential sources of contamination since the setup was not working as intended, so the number quoted below is treated as an upper limit [70].

The results of this particular set of assays are the following:

Ra assay, December 2017 50 t: gU/gH2O $= (-4.07 \pm 1.84) \times 10^{-16}$, gTh/gH2O $= (4.54 \pm 2.12) \times 10^{-15}$ [71]

Rn assay, November 2017: gU/gH2O $= < (2.89) \times 10^{-11}$.

Later on, however, the Rn assay skid was repaired and a new Rn assay was performed [72]. As noted, the time period when this assay was done is a few months

after the end of time bin 6. Furthermore, this assay was done on the water in the PSUP region of the detector and not inside the detector volume itself. However, Lozza [73] was tracking the event rate of the detector using selection cuts on reconstructed quantities, including the PSUP region where the ex situ assay was done. By making the reasonable assumptions that the PSUP water is representative of the water in the detector (the water came from the same purification plant) and that the rate observed by Lozza is due entirely to ^{222}Rn decay, we can extrapolate back to what the ex situ assay would have observed in time bin 6 [74]. It is also assumed that the water in both regions (detector and PSUP) have not changed much since time bin 6. After doing this calculation, I arrived at the concentration of Rn from the *ex situ* assay at time bin 6 of gU/gH2O = $(1.07 \pm 0.32) \times 10^{-13}$.

From Table 4.6, the average concentration of equivalent U and Th are (statistical and systematic uncertainties combined in quadrature):

- gU/gH2O = $(6.71 \pm 3.31) \times 10^{-13}$
- gTh/gH2O = $(6.72 \pm 10.36) \times 10^{-14}$

It is noticed that the concentration of U measured by the two *ex situ* assays disagree. The most likely reason is that the Rn assay is sensitive to Rn ingress in the detector whereas the Ra assay is not (due to being above Rn in the decay chain).

The Th values given by the internal backgrounds analysis is consistent with zero given the uncertainties. Thus, a 95% upper confidence limit would give gTh/gH2O $< 1.70 \times 10^{-13}$. This upper limit is consistent with the Ra assay results.

For U, since the internal analysis measures Bi activity and assumes secular equilibrium to obtain and equivalent amount of U concentration in water, it is also sensitive to Rn ingress like the Rn assay. Comparing with the predicted *ex situ* concentration, the *in situ* analysis agrees within the order of magnitude. Specifically, it is within 2σ agreement, and considering the assumptions made in calculating the predicted U concentration, this is acceptable.

Therefore, the *ex situ* assays and *in situ* analysis are consistent with each other. Due to the complicated and laborious nature of the assays, these were the only set of measurements that could be meaningfully compared with the *in situ* analysis.

4.3 External backgrounds in Water Phase

So far, this chapter dealt with the analysis of the internal backgrounds i.e. the backgrounds in the detector volume. A few words should be said about the backgrounds external to the detector volume i.e. the external backgrounds. These consists mainly of U and Th events originating from the acrylic vessel, PSUP water, hold-down/hold-up ropes, and PMTs. To ascertain the cleanliness of the water in this region, *ex situ* assays like those mentioned previously are conducted whenever possible. As was done by Zummo and Bonaventre [34] using two different methods (counting in the former, maximum likelihood fit in the latter), these external backgrounds were estimated and were found to be within expected levels. The author's work on the internal backgrounds did not use these numbers, since the selection cuts were specifically aimed to remove external backgrounds from the internal background

analysis region. Despite this, the contamination due to the AV surface events was estimated in Section 4.2.2.

4.4 Internal Backgrounds: Extended Water Phase

Following the commissioning of the low Rn nitrogen cover gas, a steady, low background extended water data set was collected from October 2018 - July 2019. This amounts to about 190 days livetime of low background data which can be used for further water analysis. The internal backgrounds analysis detailed in the previous sections was repeated with the same procedure for this new data set. The results of the internal background analysis will be used to estimate the sensitivity of a new nucleon decay limit for this data set.

4.4.1 Cuts

The cuts listed here are the same as what was done previously, except the upper energy range is set to be at the low edge of the nucleon decay ROI. Therefore, it is possible to constrain the internal backgrounds in the likelihood analysis, since this analysis would be a sideband analysis to the likelihood-based nucleon decay analysis.

- $4.0 <$ energy < 5.0 MeV
- posr < 4300mm
- nhitsCleaned ≥ 15

- itr > 0.55
- -0.12 $< \beta_{14} <$ 0.95
- fitValid, waterFit
- DC Mask: 0xFB7FFFF97FFE (to preserve blindness)
- livetime: 190.33 days

4.4.2 Results

After applying the selection cuts above and fitting the MC to the data, the results are [1]:

- Number of data events surviving: 109
- ^{214}Bi activity, [ev/yr] $= (1.30 \pm 0.26_{(stat)} + 0.46_{(syst)} - 0.35_{(syst)}) \times 10^6$
- ^{208}Tl activity, [ev/yr] $= (1.28 \pm 1.34_{(stat)} + 0.66_{(syst)} - 2.09_{(syst)}) \times 10^4$
- gU/gH2O: $(3.64 \pm 0.74_{(stat)} + 1.28_{(syst)} - 0.99_{(syst)}) \times 10^{-15}$
- gTh/gH2O: $(3.08 \pm 3.22_{(stat)} + 1.60_{(syst)} - 5.00_{(syst)}) \times 10^{-16}$

This is about an order of magnitude lower than the previous data set (Table 4.6). The plot of the fitted spectrum is shown in Figure 4.10.

[1] These numbers differ slightly than what was presented at the Neutrino 2020 conference due to a minor bug that was discovered after the fact [75].

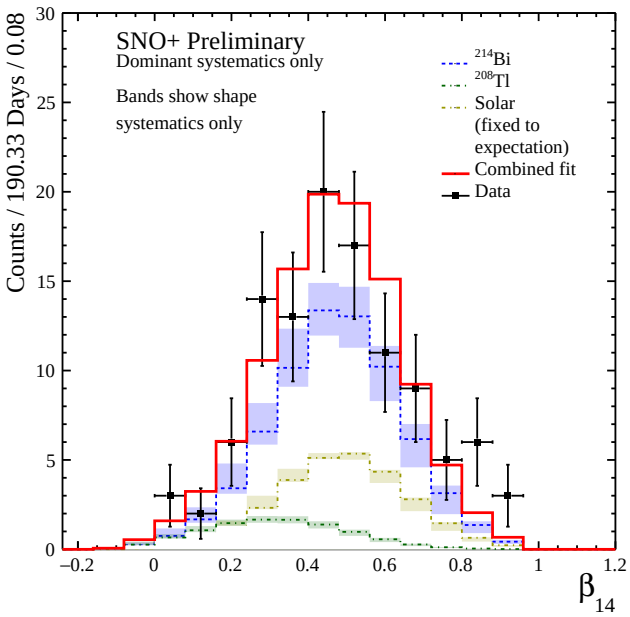

Figure 4.10: Plot showing the fit results in β_{14}-space for low background, extended water phase data set. The colored bands only show the effect of the systematics on the PDF-shapes and do not reflect the absolute magnitude of the systematics.

4.4.3 Solar Contamination

As noted above, only about 109 data events survived the cuts. This means that contamination from solar neutrinos might not be negligible, unlike before. One major source of contamination are events due to solar neutrino electron recoil. Estimating from the solar flux and MC, about 22.2 ν_e and 6.8 ν_μ solar neutrino interactions were expected in the internal background ROI, to give a total of about 29.0 solar neutrino events. This is about 27% of the data events and thus is non-negligible unlike before. To account for this, the β_{14} spectrum of the combined solar MCs was included in the fit, with the solar fit parameter fixed to the number of events estimated here. This essentially performs a direct subtraction in β_{14} space. This is shown in Figure 4.10.

As expected, the solar neutrinos look like ^{214}Bi in β_{14} space, due to the Cherenkov light of both processes originating from single electron recoils.

4.4.4 Systematics

The application of the systematics follows exactly as described in Section 4.2.4. In this extended data set, not all systematics have been fully evaluated at the time of writing. There were a myriad of changes in the RAT processing software since the original water data set (eg: changes to detector modelling and reconstruction algorithms). Thus, re-analysis of the ^{16}N calibration was still in progress. Therefore, only preliminary numbers for the dominant systematics were applied, which were for β_{14} and energy, shown in Table 4.10.

The one difference is the inclusion of an additional systematic related to the uncertainty of the solar flux and oscillation parameters. The solar flux and oscillation parameters were shifted upwards and downwards by their 1σ errors as reported in literature [44]. The fit parameter is fixed to a new, post-shifted value each time and the fit re-done. The difference in the fit values from the unshifted result is taken as a systematic. The total solar flux used is $(5.25 \pm 0.16_{(stat)} + 0.11_{(syst)} - 0.13_{(syst)}) \times 10^6 cm^{-2} s^{-1}$, taken from [76].

Systematic type	(shift-central)	
	^{214}Bi [ev/yr] ($\times 10^6$)	^{208}Tl [ev/yr] ($\times 10^4$)
shift β_{14} up	-0.03	0.25
shift β_{14} down	0.29	-1.99
scale energy up	-0.13	-0.21
scale energy down	0.15	0.17
smear energy (symmetric)	0.32	0.59
shift solar up	-0.03	0.02
shift solar down	0.03	-0.02

Table 4.10: Preliminary partial systematics for the extended low background water data set.

Chapter 5

Nucleon Decay Analysis

All the science is in the error (analysis). The rest is opinion.

A. Broderick, 2019

This chapter describes a search for "invisible" nucleon decay modes in SNO+ performed by the author, focusing on the neutron mode. Section 5.1 introduces the motivation for such an analysis. Section 5.2 until the end describes the inputs to the analysis along with a detailed treatment of the systematic uncertainties. The chapter concludes with a final result.

5.1 Motivation/Introduction

As pointed out in Chapter 1, some GUT models have been excluded but there are others that remain viable. GUT models such as one based on minimal SU(5) extension to the Standard Model by Georgi-Glashow have been excluded, since it predicts a proton lifetime of 10^{31} years [77], [78]. However, there are some models that have yet to be excluded, such as 4D SUSY GUT with dimension 6 operators

that predict a lifetime for the mode $p \to \pi^0 e^+$ to be $\sim 10^{35\pm1}$ [79]. Yet another model attempts to use 6D universal extra dimension (UED) models to simultaneously explain the smallness of neutrino mass and proton decay, which predicts the decay of nucleons into three leptons as the final states (which include 3 neutrinos). This model predicts a nucleon decay lifetime of $\tau \gtrsim 10^{48}$ years [13]. In addition, there are models that predict dinucleon decay, where as the name suggests, pairs of nucleons decay simultaneously [11]. As we can see, there are lots of models available to test. Table 5.1 gives the current best limits for some decay modes. For further information, the reader can refer to review articles [8], [10], and page 1673 of [80].

Mode	90% C.L lifetime [yr]	Source
$p \to \mu^- e^+ e^+$	1.9×10^{34}	[15]
$p \to \pi^0 e^+$	1.4×10^{34}	[19]
$p \to \bar{\nu} K^+$	5.9×10^{33}	[19]
$nn \to \pi^0 \pi^0$	4.1×10^{32}	[19]
$n \to inv$	5.8×10^{29}	[81]
$p \to inv$	3.6×10^{29}	[21]

Table 5.1: A selection of some nucleon decay modes and their current lifetime limits.

It was stated in Chapter 1 that water Cherenkov detectors make sensitive experiments for a nucleon decay search, due to their scalability. SNO+ had a long period where it was filled with water which allows a limit to be set for nucleon decay, as mentioned in Chapter 2. Specifically, SNO+ intended to set a limit on the "invisible" nucleon decays. A method to detect such decays has been proposed whereby the nuclear de-excitation of the nucleus after a neutron or proton has decayed is measured [20]. Depending on the nuclear shell the decaying nucleon originated from, the de-excitation mode, energy and probability of that process happening (branching

ratio) will be different. This is the nucleon decay signal that SNO+ is searching for. Specifically, SNO+ looks for the de-excitation of ^{15}O* and de-excitation of ^{15}N*, depending on whether a neutron or a proton decayed, respectively. There are various de-excitation modes depending on the energy level of the decaying nucleon but the mode with the highest branching ratios are ^{15}O* de-exciting via emitting a 6.18MeV gamma and ^{15}N* de-exciting via emitting a 6.32 MeV gamma. Many cosmogenic backgrounds lie in this energy range but SNO+ is uniquely situated 2km underground and thus shielded from almost all of this background.

Mode	SNO+ limits [yrs]	Existing limits [yrs]
n	2.5×10^{29}	5.8×10^{29} [81]
p	3.6×10^{29}	2.1×10^{29} [31]
pp	4.7×10^{28}	5.0×10^{25} [14]
pn	2.6×10^{28}	2.1×10^{25} [82]
nn	1.3×10^{28}	1.4×10^{30} [81]

Table 5.2: SNO+ published results compared to the existing limits at the time of its publication. Extracted from [21].

SNO+ has published the results of such a search, summarized in Table 5.2. Looking at the results, SNO+ obtained world-leading limits in all "invisible" nucleon decay modes except in neutron and dineutron decay. The aim of the analysis presented in this chapter is to develop a methodology in an attempt to improve those limits using the same dataset, with a focus on neutron decay.

From now on, only neutron decay is considered as it is the focus of this thesis but the analysis method developed in the rest of this chapter can easily be used to search for "invisible" proton and dinucleon decay. Table 5.3 gives the neutron decay

modes of interest to SNO+. The sum of all the branching ratio values, B(k), gives the total theoretical efficiency which is applied alongside the acceptance efficiency. Thus, $\epsilon_{theory} = 0.53$. Not listed in this table is the possibility that the decay occurs directly to the ground state without any excited states, and this has a branching ratio of 0.25. Also not listed are other various low energy γ cascade states, which collectively have a branching ratio of 0.22.

Hole	(k)	E_γ [MeV]	E_p [MeV]	E_n [MeV]	B(k)
$(p_{3/2})^{-1}$	^{15}O	6.18	0	0	0.44
$(s_{1/2})^{-1}$	^{14}N	0	~24	0	0.02
	^{14}N	7.03	~17	0	0.02
	^{13}C	0	~14.5 + 1.6	0	0.01
	^{14}O	0	0	~18	0.02
	^{13}O	0	0	~11.5	0.02

Table 5.3: Deexcitation modes (k) of neutron holes $(j)_n^{-1}$ with $j = p_{1/2}, p_{3/2}$, and $s_{1/2}$ in ^{15}O. E_γ, E_p, and E_n are the kinetic energies for the de-exciting γ ray, proton, and neutron, respectively. B(k) is the branching ratio of the mode k. Extracted from [20].

For the various nucleon decay modes, the RAT MC event generator produces the decay products as the atom de-excites, after one of the nucleons has decayed producing no visible products [1]. The predicted energy and branching ratios of the decay products (mainly gammas) are taken from [20]. This is done similarly for di-nucleon decays with the branching ratios taken from [11]. Since the focus of this thesis is developing an analysis methodology using the neutron decay mode, only the neutron decay simulations were used. However, the analysis will be repeated for the

[1] The nucleon decay generator was first added into the RAT Github repository in tag 4.6.0 commit number 695 [55].

other decay modes by substituting in the relevant signal PDF simulations. An example comparing the energy PDFs of two of the decay modes (neutron and proton) is shown in Figure 5.1.

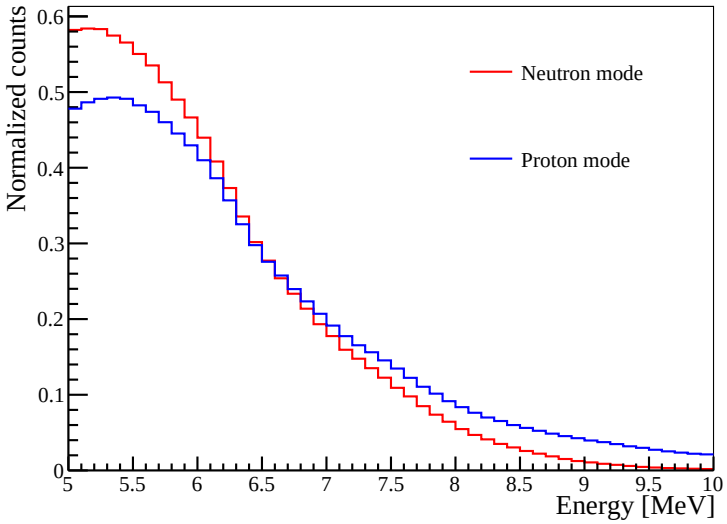

Figure 5.1: Plot comparing the PDFs of the "invisible" neutron and proton decay signal modes.

5.2 Overview of Analysis

The goal is to perform the analysis using an extended binned maximum likelihood procedure, as elaborated previously in Chapter 3. In this case, the likelihood is minimized simultaneously over five different observables. The simulated background events are binned in the selected five observables to produce 1-dimensional probability density functions/distributions (PDFs). Ideally, an analytical form of the PDFs would be used but taking into account all the possible physics effects to properly model the detector response would be intractable. By simulating millions of events,

we can build histograms of these PDFs would take these effects into account. In addition, since we are considering five observables, it would be ideal to perform a single fit in 5-dimension space to properly account for correlations. However, the extremely large number of simulated events needed to build smooth PDFs in that space, as well as the computing memory needed to fit that many bins in 5D space makes this approach unfeasible. In short, we have to perform a simultaneous maximization of the likelihood (minimizing negative log likelihood) across five 1D observables with PDFs built by binning simulated events. One minor disadvantage is that event correlations between observables are washed out by projecting into 1D but the different PDF shapes of the backgrounds in various observable spaces are still preserved and utilized.

The five observables chosen are: energy, direction, isotropy, volume-weighted radial position, and solar direction (E, $\hat{U} \cdot \hat{R}$, β_{14}, R^3, $\cos\theta_{\mathrm{sun}}$). E is the energy of the event reconstructed from knowing an event's position and the number of PMTs triggered (Nhits) by that event. $\hat{U} \cdot \hat{R}$ is the projection of a particle's reconstructed direction unit vector onto the corresponding event position unit vector relative to the center of the detector. Event isotropy (β_{14}), introduced in Chapter 4, is a measure of the isotropy of an event. It is also used as an observable. The position of an event within the detector can also be determined by charge and timing information of the triggered PMTs. This is then volume-weighted with respect to the radius of the acrylic vessel: $\mathrm{R}^3 = (\mathrm{R}/\mathrm{R}_{\mathrm{AV}})^3$. The solar direction, $cos\theta_{sun}$, is the reconstructed direction of an event relative to the sun at any given time and is calculated using an algorithm developed by SNO.

As highlighted in Chapter 3, some backgrounds can be constrained from independent measurements and this is elaborated in the following section.

5.3 Constrained parameters

This subsection describes how some parameters are constrained.

5.3.1 Solar events

Energy-averaged elastic scattering cross-sections for solar neutrinos are available in literature [83]. The ^{8}B solar neutrino flux is well known from experiment and calculation [44]. The number of available electron targets in the detector volume can be calculated. From these, we have:

$$\Phi_{^8B} = 5.79 \times 10^6 \nu/cm^2/s$$

$$\sigma_{\nu_e} = 6.08 \times 10^{-44} cm^2$$

$$\sigma_{\nu_{\mu,\tau}} = 1.04 \times 10^{-44} cm^2$$

$$n_e = 3.023 \times 10^{32} \text{ electrons}$$

Thus, the expected full volume solar neutrino rates, R, based on flavor are calculated (using $R = \Phi_{^8B}\sigma n_e$, with the appropriate σ substituted) to be:

$$\nu_e = 9.19 \text{ events/day}$$

$$\nu_{\mu,\tau} = 1.57 \text{ events/day}$$

The uncertainty on $\Phi_{^8B}$ is measured to 2.2% (0.13×10^6 $\nu/cm^2/s$), which is used as the width of the Gaussian constraint. Uncertainties in the survival probabilities have not been taken into account in the values above but are applied in the analysis. The survival probability of the solar neutrinos assumes the BS05OP solar model [36].

5.3.2 Reactor events

These are reactor anti-neutrinos originating mostly from the three nearby nuclear reactors, shown in Chapter 2. The full volume rate has been estimated via Monte Carlo in previous studies, which gave a full volume rate of 0.57 ± 0.57 events/day [34].

5.3.3 Atmospheric events

In the atmosphere, neutrinos are created when cosmic rays, primarily protons, interact with nuclei in the atmosphere. In these interactions, mesons, such as pions and kaons, are produced, which decay mainly into muons. Neutrinos are produced both in the pion and kaon decays in the subsequent muon decay. These neutrinos, typically in the 100 MeV to 10 GeV range, can interact with an oxygen nucleus via neutral-current interactions and liberate a nucleon [21]. This process creates an excited oxygen nucleus which de-excites through various channels, most of which consist of γ-rays that end up in the nucleon decay region of interest. Studies were done previously with GENIE software and the expected number of events was extrapolated into detector volume via RAT MC [84], [85]. The atmospheric events that we are interested in are those that share a signal with the neutron decay mode, that is the de-excitation gamma associated with ^{16}O losing a neutron. Therefore, we model

this background using the same simulations as that of neutron decay. A total of 0.226 ± 0.025 events/day are expected in the full volume detector.

5.4 Data set separation

As was done in Chapter 4, the data set was divided into independent time periods ("time bins") due to varying detector conditions. The data of each time bin would then be fit independently and combined statistically by multiplying their likelihood curves to obtain an overall result. However, the separation of the time periods was done differently for this analysis. When performing this analysis, it was found that due to the limited statistics in each individual time bin, the minimizer suffered from convergence issues when floating the energy systematics as described in Section 5.14. Since time bins 1, 2 and 3 as defined in Chapter 4 were similar in background rate and trigger efficiency, it was decided to combine these three time bins into a single time bin. The other time bins (4,5,6) were kept separate as their background levels varied widely between them and a trigger efficiency change occurred in the middle of time bin 4.

5.5 Fiducial volume optimization

In order to ascertain the effectiveness of the cuts used in [21], the author looked at the data at an energy sideband to the nucleon decay ROI, which is between 4 - 5 MeV. The analysis cuts in [21] were applied and it was found that there is still an excess of events at high z-position, shown in Figure 5.2. This corresponds to a region of high activity at the region below the neck of the detector ("hotspot") which can

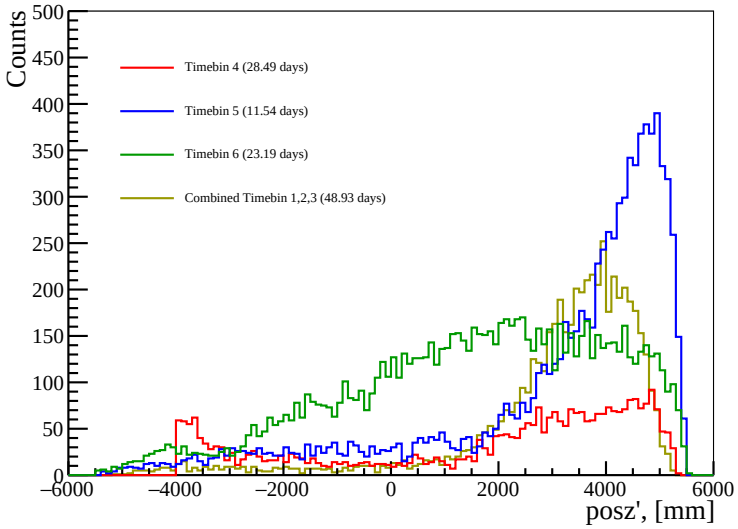

Figure 5.2: Energy sideband of the data with selection cuts from [21] applied.

leak into the analysis window. It was assumed in the published analysis that this particular class of background was minimized with the applied selection cuts, and so no PDF was generated for it. The effect of this leakage shows up as tension in the fits, particularly in the $\hat{U} \cdot \hat{R}$ and R^3 observable spaces. There is an excess of events at high R^3 and at -1 $\hat{U} \cdot \hat{R}$ in the data, shown in Figure 5.3 and Figure 5.4. The high R^3 excess makes sense, since the "hotspot" is just below the neck of the detector and would look like an external background. However, the external background PDF peaks in the opposite $\hat{U} \cdot \hat{R}$ region. However, our ability to model the "hotspot" was uncertain. To reduce this effect, and to improve the signal-to-noise ratio, the fiducial volume was re-optimized.

To do this, we need to define a proxy measure of the sensitivity. Let N_S be the unknown number of signal counts, N_B the number of background counts, and N_T

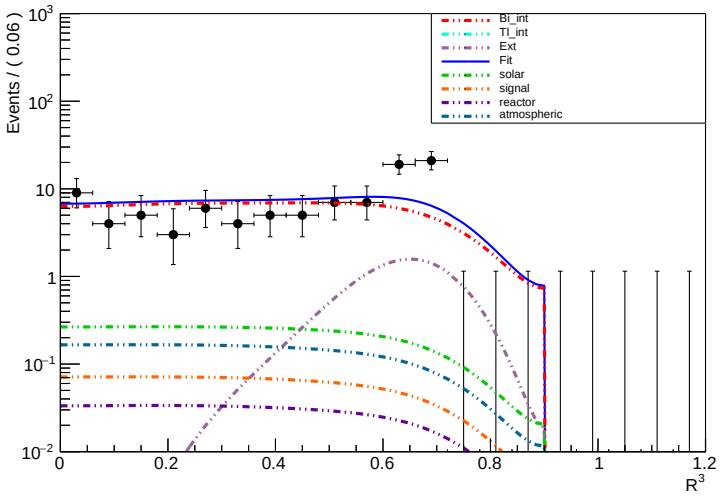

Figure 5.3: R^3 for time bin 4 before optimization. Note the excess at high R^3.

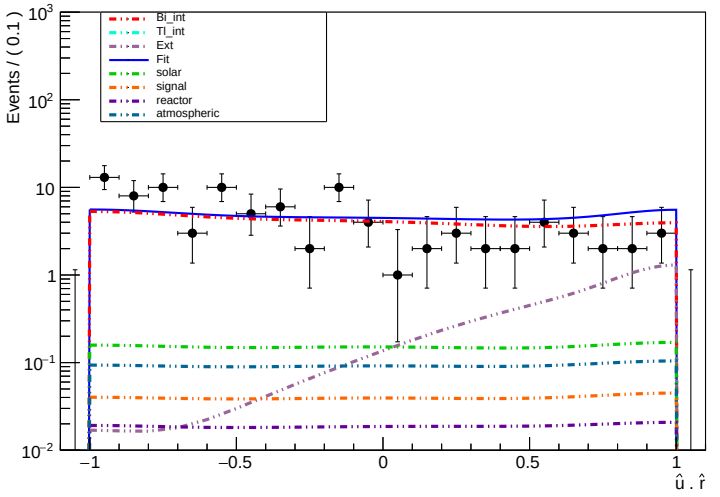

Figure 5.4: $\hat{U} \cdot \hat{R}$ for time bin 4 before optimization. Note the excess at -1, and that the externals peak in the opposite direction.

the total counts. Therefore, we have $N_S = N_T - N_B$. Assuming that N_T and N_B is large, then they will follow Gaussian distributions. Thus, the uncertainty on N_S will also be Gaussian distributed with standard deviation $\sigma^2_{N_S} = \sigma^2_{N_T} + \sigma^2_{N_B}$. Furthermore,

assuming the only fluctuations are coming from counting statistics (Poisson), we have that $\sigma_{N_B} = \sqrt{N_B}$ and $\sigma_{N_T} = \sqrt{N_T}$. Now, we can define an approximate measure of the sensitivity:

$$\begin{aligned}\frac{\sigma_{N_S}}{N_S} &= \frac{\sqrt{\sigma_{N_T}^2 + \sigma_{N_B}^2}}{N_S} \\ &= \frac{\sqrt{N_T + N_B}}{N_S} \\ &= \frac{\sqrt{N_S + 2N_B}}{N_S}\end{aligned}$$

Since we are looking for small signal in a region of large background, we have that $N_S \ll N_B$. Therefore,

$$\frac{\sigma_{N_S}}{N_S} = \frac{\sqrt{2N_B}}{N_S} \tag{5.1}$$

We then make the reasonable approximation that N_S is proportional to the volume of the detector region we are considering. Making this substitution in the expression above gives the final form of the measure of sensitivity, dropping constants:

$$\frac{\sigma_{N_S}}{N_S} = \frac{\sqrt{N_B}}{V} \tag{5.2}$$

As the z-position and radial position cuts are varied, the number of events passing these cuts in the energy side-band are counted and the volume re-calculated. The aim is to determine a set of fiducial volume cuts that minimize the sensitivity parameter. The volume is calculated as a sphere with a cap subtracted, illustrated in Figure 5.5. Sensitivity contour plots of each of the time bins are generated and the optimal cuts

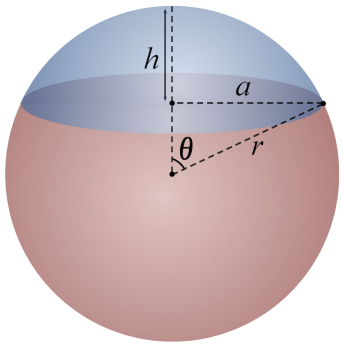

Figure 5.5: Sphere with a cap subtracted. r is the radius of the sphere, a is the radius of the base of the cap, h is the height of the cap.

can be read off, shown in Figure 5.6, Figure 5.7, and Figure 5.9. After applying these cuts, time bin 4 exhibited an excess of events in the lower half of the detector, shown in Figure 5.10. Therefore, the cuts for time bin 4 were further adjusted, this time introducing a lower z-position cut as well. The final result of the whole procedure is shown in Figure 5.11. As can be seen, the events are more or less uniform in the individual time bins. It can also be seen the that backgrounds of time bin 6 are orders of magnitude higher than all the other time bins. A systematic must still be assigned to account for residual "hotspot" events, a point which will be elaborated in Section 5.13, and it was found that this systematic was very large for time bin 6. Therefore, it was decided to exclude time bin 6 from the analysis entirely.

5.6 Event Selection Cuts

Taking the results of the fiducial volume optimization above, the final selection cuts for each time bin are listed in Table 5.4, along with the livetime.Table 5.5 shows the signal acceptance efficiency after selection cuts, which were determined

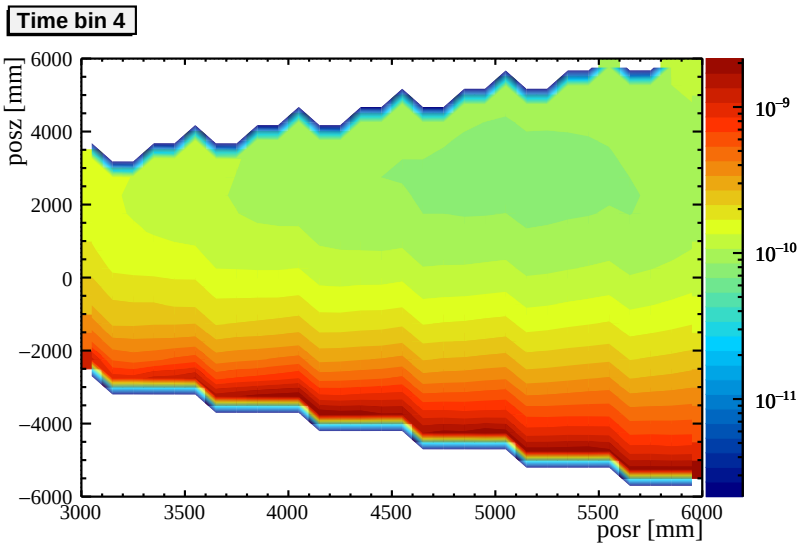

Figure 5.6: Sensitivity contour map for time bin 4. Color-axis gives the relative values of the sensitivity parameter in arbitrary units. x-axis corresponds to posr < X. y-axis corresponds to -6000 < posz < Y.

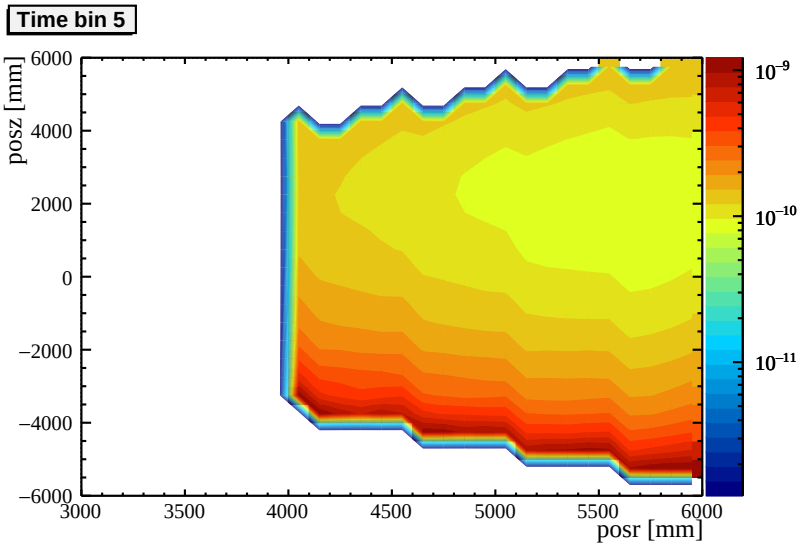

Figure 5.7: Sensitivity contour map for time bin 5. x-axis corresponds to posr < X. y-axis corresponds to -6000 < posz < Y.

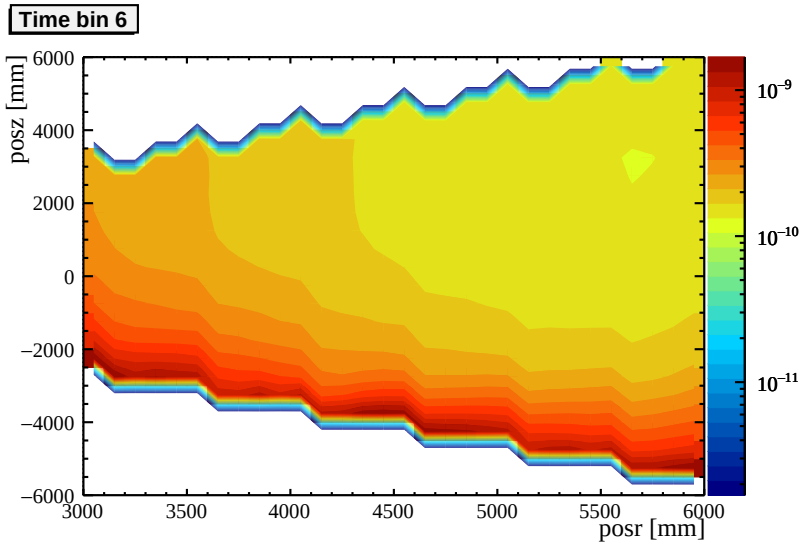

Figure 5.8: Sensitivity contour map for time bin 6. x-axis corresponds to posr < X. y-axis corresponds to -6000 < posz < Y.

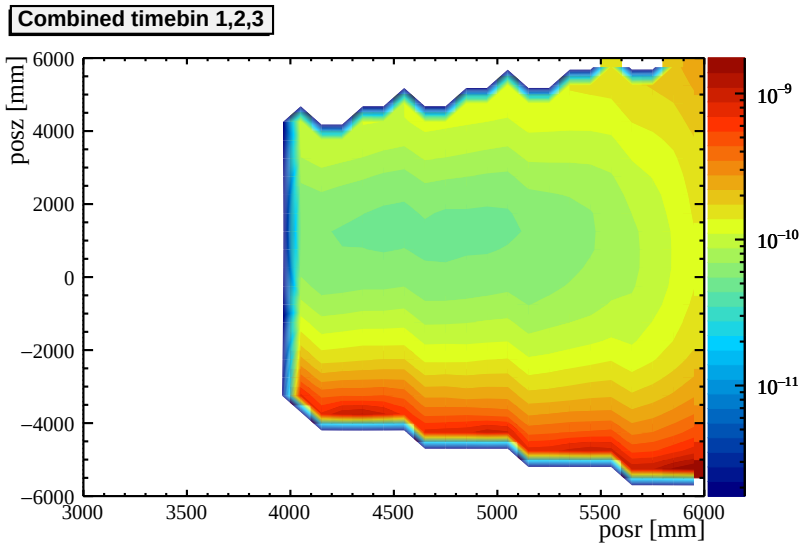

Figure 5.9: Sensitivity contour map for combined time bins 1,2, 3. x-axis corresponds to posr < X. y-axis corresponds to -6000 < posz < Y.

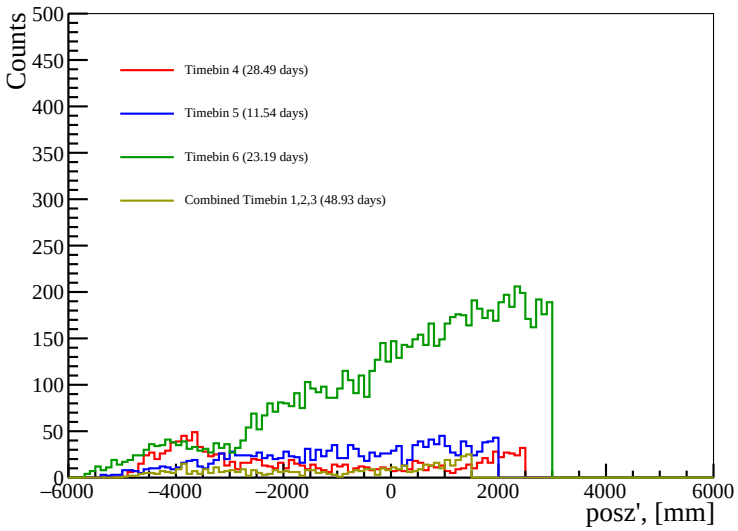

Figure 5.10: Energy sideband of the data after optimization procedure.

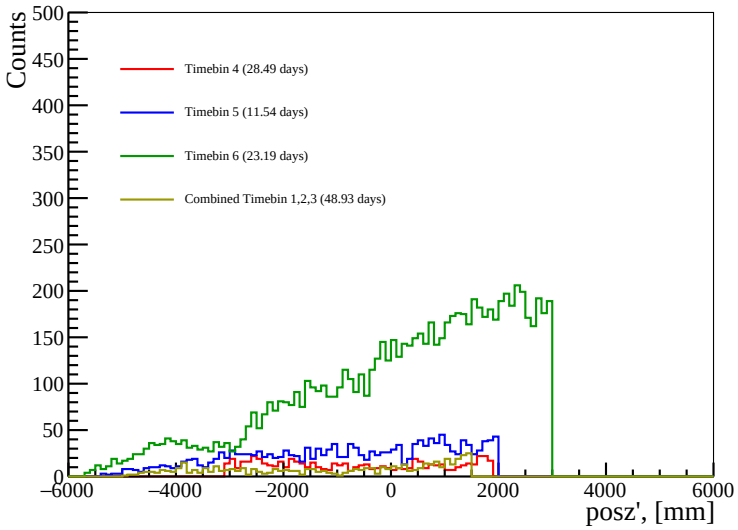

Figure 5.11: Energy sideband of the data after further optimization of time bin 4.

from Monte Carlo. Other selection cuts (described previously in Chapter 4) include data cleaning, valid fits and ITR > 0.55 . A $cos\theta_{sun}$ cut was chosen to minimize solar neutrino background contamination and was based on the optimization done by Askins [65]. In addition, there is a sacrifice associated with applying data cleaning, as first introduced in Chapter 4. This was found to be around 3% across all time bins and so was included in the livetime values [34].

Time bin	R(mm)	z(mm)	$cos\theta_{sun}$	Livetime (days)
4	5100	[-3100, 1900]	[-0.70, 1]	28.49
5	5400	[-6000, 2000]	[-0.80, 1]	11.15
Combined 1,2,3	5100	[-6000, 1500]	[-0.70, 1]	48.93

Table 5.4: Event selection cuts that differ between time bins along with their live-times.

Time bin	Efficiency
4	0.0930
5	0.1315
Combined 1,2,3	0.0979

Table 5.5: Signal acceptance efficiency for the time bins. $\epsilon_{theory} = 0.53$ defined in the beginning of this chapter has been included.

5.7 Background Expectation

After determining the fiducial volume of each time bin, it is possible to estimate the individual contributions of each class of background in the respective time bins. The internal Bi and internal Tl full-volume rates can be found in Chapter 4. The full volume rates for solar neutrinos, reactor neutrinos and atmospheric backgrounds were described in Section 5.3. External backgrounds rates are obtained from [34]. Since one data set is a combination of time bins 1,2 and 3, the background estimates from

those three time bins were weighted by livetime and averaged to obtain an estimated rate in that combined dataset. Table 5.6, Table 5.7, and Table 5.8 summarizes the expected background rates for each time bin.

The PDFs of the background classes listed in the tables were constructed by applying the selection cuts listed previously to the simulated events of each background class. The surviving events were then binned into 1D histograms. The PDFs of external Bi, external Tl, Bi AV, and Tl AV were combined at the expected rates shown in the tables, since we do not expect to be able to resolve each individual component due to the low efficiency. Solar neutrino PDFs were combined based on the survival probability and the ratio of the cross-sections. The PDF for the neutron decay signal was used as a proxy for the atmospherics, since the atmospheric background of interest mimics identically the neutron decay signal, as described in Section 5.3.

There are some possible contamination sources that have not been fully evaluated, like contamination from ^{208}Tl events from PMTs and events that 'leak' from the data cleaning cuts. Since it was decided from the beginning that a limit would be set, these can be neglected for now, at the cost of potentially setting a worse limit if there was any significant amount of these types of contamination. Although these uncertainties are poorly defined in initial estimates, the overall contribution is shown to be small [34].

Background class	Full-rate (events/day)	Efficiency, ϵ	ROI rate (events/day)
Internal Bi	1.882×10^5	4.926×10^{-6}	0.9272
Internal Tl	1.077×10^3	7.866×10^{-5}	0.08469
Solar ν_e	9.195	5.31×10^{-3}	0.0488
Solar ν_μ	1.573	9.89×10^{-3}	0.01556
External Bi	9.981×10^4	6.118×10^{-8}	6.106×10^{-3}
External Tl	2.175×10^4	2.320×10^{-7}	5.046×10^{-3}
Bi AV	1.035×10^4	9.636×10^{-8}	9.973×10^{-4}
Tl AV	0	2.212×10^{-6}	0
Reactor	0.57	0.01423	8.112×10^{-3}
Atmospherics	0.226	0.1754	0.0396

Table 5.6: Time bin 4 expected backgrounds.

Background class	Full-rate (events/day)	Efficiency, ϵ	ROI rate (events/day)
Internal Bi	5.192×10^5	6.987×10^{-6}	3.6275
Internal Tl	3.307×10^3	1.151×10^{-4}	0.3806
Solar ν_e	9.195	1.14×10^{-2}	0.1048
Solar ν_μ	1.573	2.11×10^{-2}	0.0332
External Bi	2.032×10^5	2.906×10^{-7}	0.0590
External Tl	3.326×10^4	1.268×10^{-6}	0.0422
Bi AV	2.037×10^4	3.227×10^{-7}	6.5734×10^{-3}
Tl AV	0	9.725×10^{-6}	0
Reactor	0.57	0.02052	0.01170
Atmospherics	0.226	0.2481	0.0561

Table 5.7: Time bin 5 expected backgrounds.

5.8 Kernel Density Estimation (KDE)

Some classes of backgrounds (in particular, the external backgrounds) lacked sufficient Monte Carlo to build smooth PDFs, where the statistical uncertainty on these distributions can't be neglected. The most direct way to solve this issue would be to

Background class	Full-rate (events/day)	Efficiency, ϵ	ROI rate (events/day)
Internal Bi	1.682×10^5	4.951×10^{-6}	0.8329
Internal Tl	1.463×10^3	8.025×10^{-5}	0.1174
Solar ν_e	9.195	5.69×10^{-3}	0.0523
Solar ν_μ	1.573	1.05×10^{-2}	0.0165
External Bi	4.285×10^6	5.965×10^{-8}	0.2556
External Tl	1.265×10^5	2.552×10^{-7}	0.0322
Bi AV	3.591×10^5	1.055×10^{-7}	0.0379
Tl AV	1.512×10^4	2.676×10^{-6}	0.0405
Reactor	0.57	0.0147	8.391×10^{-3}
Atmospherics	0.226	0.1848	0.0418

Table 5.8: Combined time bins 1,2,3 expected backgrounds.

simulate more Monte Carlo events but this was not possible to due to resource limitations. Therefore, Kernel Density Estimation (KDE) was employed in an attempt to smooth out the PDFs. An example of this is shown in Figure 5.12. As can be seen, in the region where the bins are well-populated, the KDE PDF does not differ much from the original. However, at the tail end of the distribution, where the bins are sparsely populated and there are sudden drops in the histogram, the KDE method attempts to smooth it out, producing a smooth and continuous PDF. This method does change the shape of the PDFs and so a systematic uncertainty would have to be assigned for this difference, which is discussed in Section 5.13.

Formally, the Kernel Density estimator is defined to be:

$$\hat{p}_n = \frac{1}{nh} \sum_{i=1}^{n} K\left(\frac{X_i - x}{h}\right)$$

where $K(x)$ is called the kernel function that is generally any smooth, symmetric

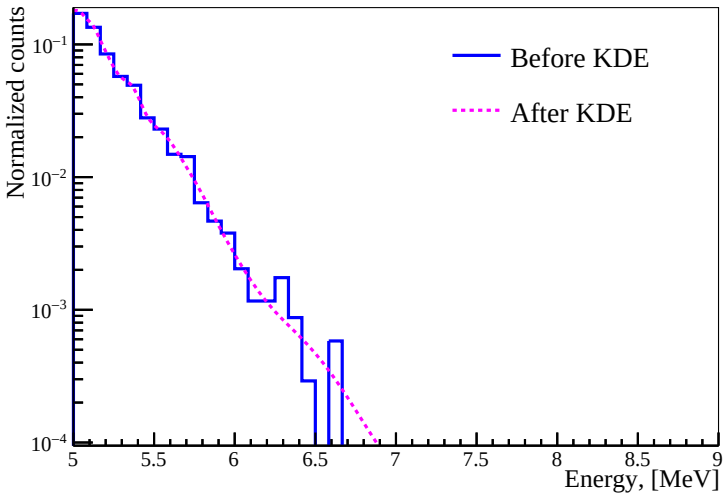

Figure 5.12: Application of KDE to a PDF of internal Bi.

functions such as a Gaussian. $h > 0$ is called the smoothing bandwidth that controls the amount of smoothing. X_i is each bin in the histogram. In essence, the algorithm smooths each of the bins into small density bumps and sum all of these bumps to obtain the final density estimate [86]. For this analysis, RooFit's kernal density estimation function was utilized (`RooKeysPdf`) [87].

5.9 Example fit

In order to give an example of putting together everything presented so far, a fit was done to time bin 4 with and without KDE smoothing. The best-fit values are shown in Table 5.9. As can be seen, the values are consistent between the two methods. The fit spectra in all the observable spaces, with and without KDE, are shown in Figure 5.13, Figure 5.14, Figure 5.15, Figure 5.16, and Figure 5.17.

Parameter	No KDE [counts]	KDE [counts]
Atmospherics	$1.13^{+1.24}_{-1.24}$	$1.13^{+1.24}_{-1.24}$
Solars	$1.83^{+0.04}_{-0.04}$	$1.83^{+0.04}_{-0.04}$
Reactors	$0.23^{+0.23}_{-0.23}$	$0.23^{+0.23}_{-0.23}$
Internal Bismuth	$1.31^{+0.39}_{-0.44}\times10^{1}$	$1.63^{+0.50}_{-0.57}\times10^{1}$
Internal Thalium	$1.68^{+3.56}_{-2.44}$	$-9.5^{+49.4}_{-33.9}\times10^{-1}$
Externals	$2^{+140}_{-116}\times10^{-2}$	$-1.07^{+1.67}_{-1.39}$
Signal	$0.97^{+2.68}_{-2.03}$	$1.53^{+3.04}_{-2.30}$
Total Events	18.96	19.00

Table 5.9: Best-fit values for the various fit parameters without and with KDE smoothing. The dataset had 19 events.

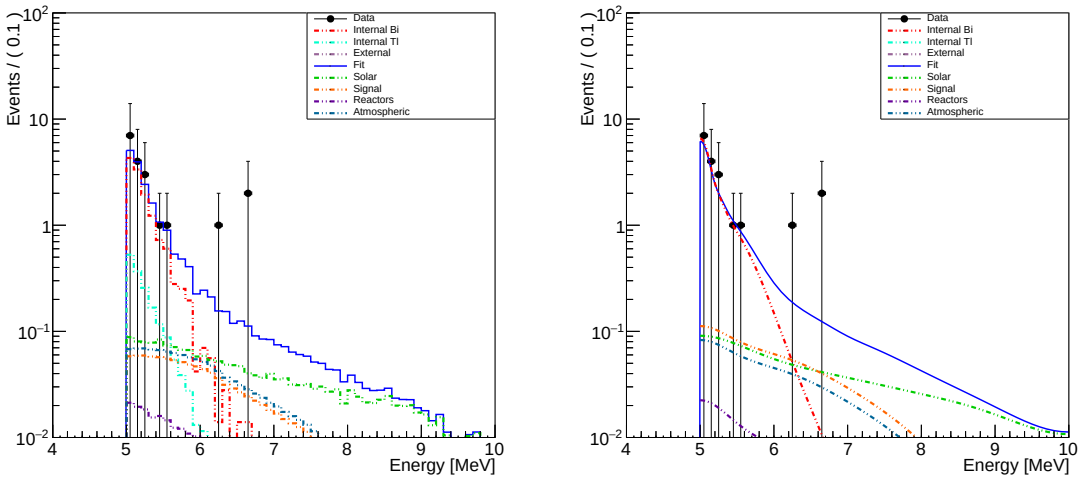

(a) Without KDE

(b) With KDE

Figure 5.13: Best-fit energy spectra for time bin 4 with and without KDE smoothing.

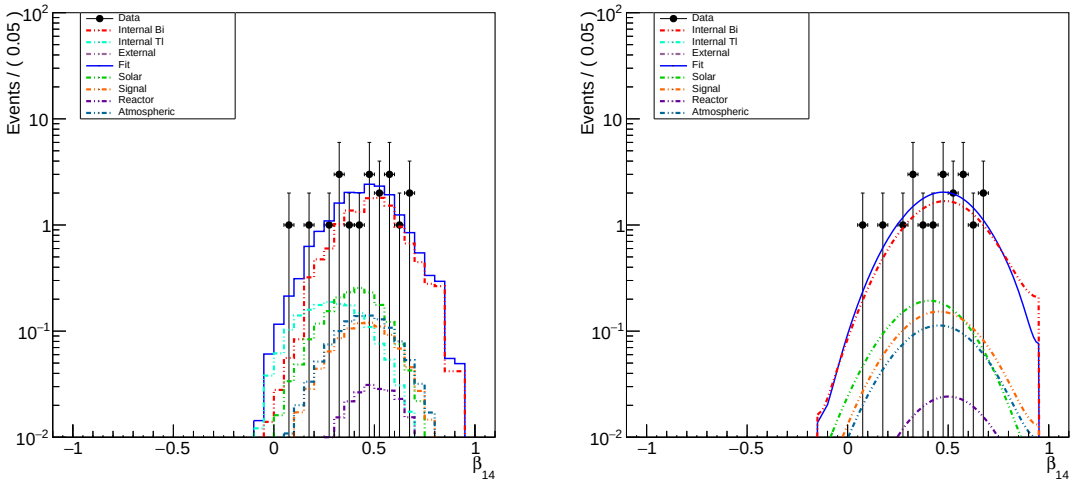

(a) Without KDE (b) With KDE

Figure 5.14: Best-fit β_{14} spectra for time bin 4 with and without KDE smoothing.

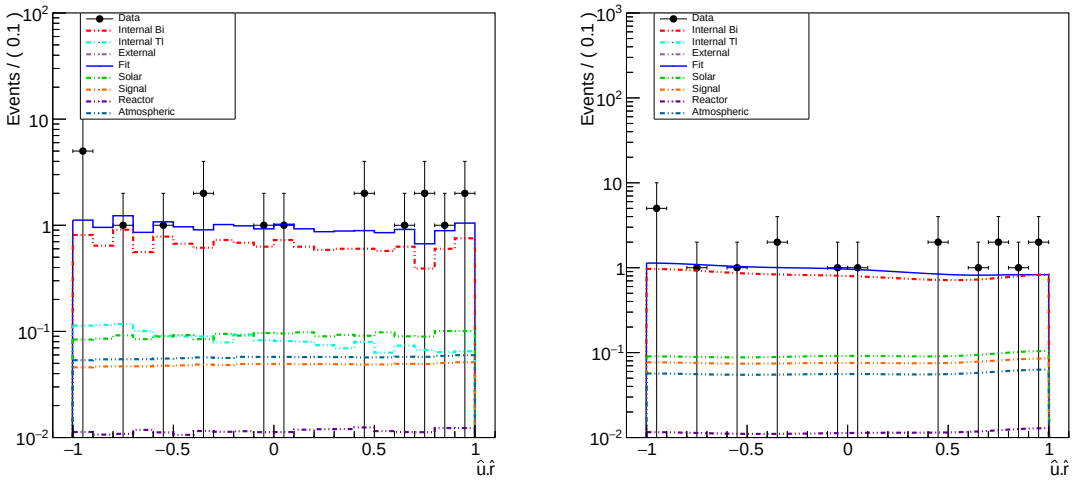

(a) Without KDE (b) With KDE

Figure 5.15: Best-fit $\hat{U} \cdot \hat{R}$ spectra for time bin 4 with and without KDE smoothing.

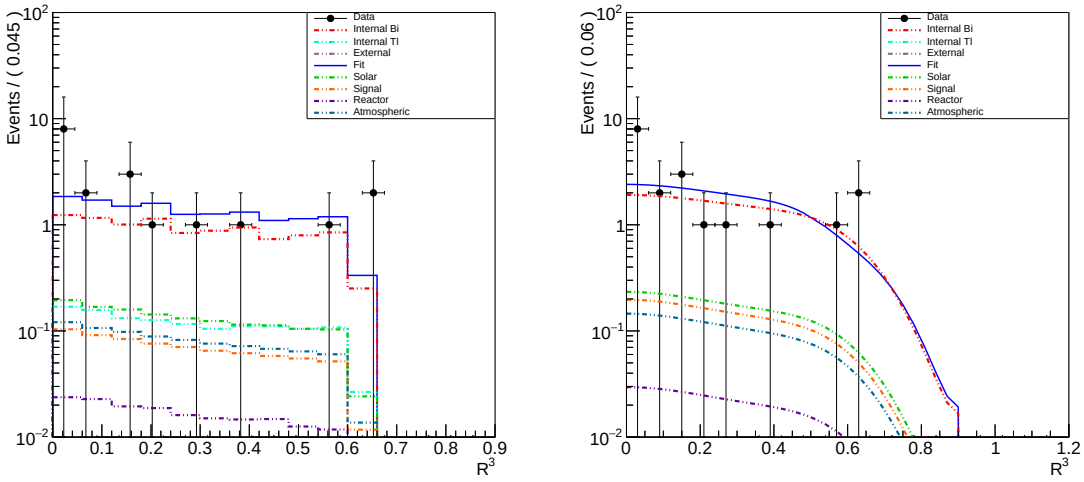

(a) Without KDE (b) With KDE

Figure 5.16: Best-fit R^3 spectra for time bin 4 with and without KDE smoothing.

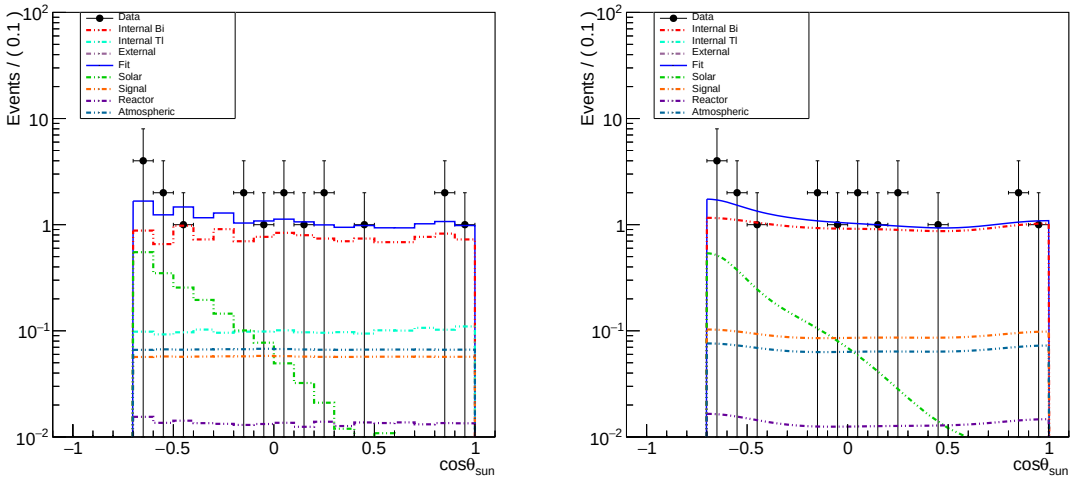

(a) Without KDE (b) With KDE

Figure 5.17: Best-fit $\cos\theta_{\text{sun}}$ spectra for time bin 4 with and without KDE smoothing.

5.10 Profile Likelihood Ratio

In order to properly combine the results of each individual time bin and to compute an upper limit for nucleon decay, a profile likelihood ratio curve was generated for each time bin. From the maximum likelihood estimate method above, we have obtained a result that can be rephrased into the statement "The number of nucleon decay signals is X". We now want to compare this to other possible values of the signal i.e. how does the obtained result compare to other possibilities. We can define the null hypothesis to be "The number of nucleon decay signals is Y" i.e. a value of Y that is chosen to be the "what if the signal value is Y".

Now we need a way to quantitatively compare the two competing hypotheses. According to the Neyman-Pearson Lemma, the likelihood ratio is a powerful measure of the compatibility of the two hypotheses. Since it is a function of the data, it is a test statistic. It has the form:

$$Q(x) = \frac{\mathcal{L}(\theta_0|x)}{\mathcal{L}(\theta_1|x)} \tag{5.3}$$

where x $\equiv$ data, and $\theta_0, \theta_1 \equiv$ parameters that maximize likelihood under null hypothesis (0) or alternate hypothesis (1). Computationally, it is more convenient to work with the negative log likelihood ratio. Taking the negative log of both sides of the equation gives:

$$-\,logQ(x) = -[\ell(\theta_0) - \ell(\theta_1)] \tag{5.4}$$

where $\ell(\theta_0)$ and $\ell(\theta_1)$ represent the log-likelihoods under the two hypotheses.

In our fits, there is really only one parameter we are interested in i.e. the number of signal events. However, we cannot ignore the other parameters when estimating the signal events i.e. they are a nuisance. Hence, they are generally called "nuisance parameters". The frequentist method of handling these nuisance parameters is done through a method called "profiling," where the parameter of interest is scanned through its parameter space while all the parameters are allowed to fit freely at each particular value of the parameter of interest. This has the effect of integrating away all the nuisance parameters and projecting onto the parameter of interest.

Taking this together with the likelihood ratio, we can form a probability density of the signal parameter by scanning over the possible values of the signal parameter, and computing the likelihood ratio at each point. Specifically, for each possible signal value, a fit was performed with the signal rate fixed to that value and the other parameters floated as usual, and the "best-fit" likelihood obtained for that signal rate. Since the absolute value of the likelihood does not really have meaning, we are in essence calculating the relative probability of a particular set of fit parameters relative to the global maximum likelihood. After normalizing that distribution to unit area, we can integrate up to a specified confidence level (90% in this case) which will give an upper limit. By integrating up to a value X, we are calculating the total probability that the parameters have a value less than or equal to X. Usually, the likelihood is linked to the χ^2 distribution in the asymptotic limit and the edge limits on the χ^2 distribution are mapped onto a standard Gaussian to obtain a certain confidence level. The procedure used here does not make asymptotic assumptions by

generating the equivalent of the standard Gaussian and integrating directly without need of mapping. In addition, this analysis only considers the physical likelihood space of strictly positive signal rates. In practice, the likelihood space below zero is cut before the remaining likelihood curve is normalized. While negative signal rates are not strictly forbidden in frequentist statistics, a check was done and it showed that only considering positive signal rates set a more conservative limit.

To illustrate this, the profile likelihoods corresponding to the fits in Section 5.9 are shown in Figure 5.18 and Figure 5.19. Again, the 90% upper limit shown in the figures are calculated using only the positive signal rates. The statistical uncertainty of the distribution was found by integrating around the peak to obtain an area of 68% using the Feldman-Cousins rank-ordering method [88].

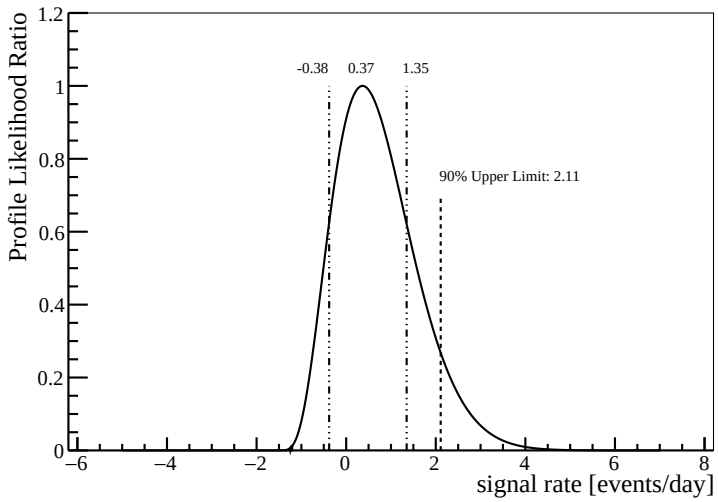

Figure 5.18: Profile likelihood of the signal for time bin 4 without KDE smoothing.

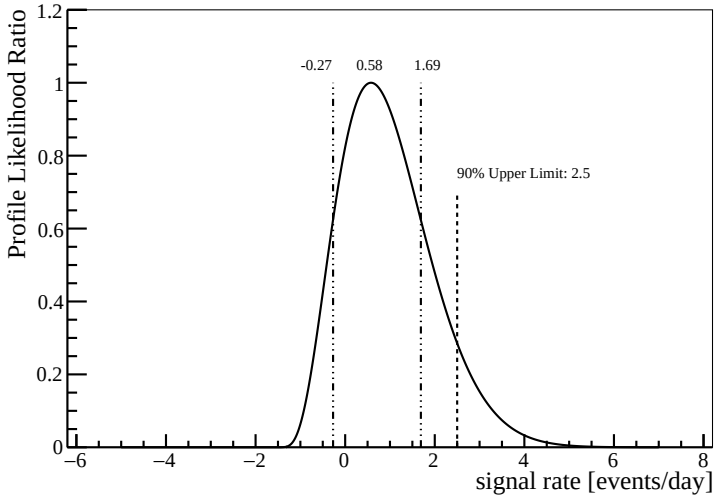

Figure 5.19: Profile likelihood of the signal for time bin 4 with KDE smoothing.

5.11 Results

After the selection cuts were performed on both the data and MC, the fits were performed on each time bins independently. The fitted number of signal events is corrected with the signal acceptance efficiency after selection cuts, for each time bin, shown in Table 5.5. This is further weighted by the livetime of each time bin to obtain a full-volume signal rate. The likelihood ratio distributions for each time bin was generated by profiling over this signal rate. These distributions were then combined to give an overall profile likelihood ratio distribution. The 90% upper limit is then computed from this combined distribution and converted to a lower limit on neutron decay lifetime. The statistics only profile likelihoods are shown in Figure 5.20. The statistical uncertainty of the distribution was found by integrating around the peak to obtain an area of 68% using the Feldman-Cousins rank-ordering method [88]. The best-fit spectra of the observables for time bin 5 and combined time bins 1,2,3 are in Appendix A. The best-fit spectra for time bin 4 were shown previously in Section 5.9.

In order to translate the upper limit on the signal rate to a lifetime limit on neutron decay, we need the number nucleons that can undergo the decay. The formula to calculate this value is:

$$N_{Nucleons} = 0.9976 \times 8 \times \frac{4\pi R^3}{3} \times \frac{\rho(T,P)}{m_{H_2O}}$$

$N_{Nucleons}$ is the number of individual nucleons within ^{16}O nuclei in the detector. The natural abundance of ^{16}O is 99.76% and is taken into account in the first term in the equation. There are a total of 8 each of neutrons and protons in ^{16}O which is

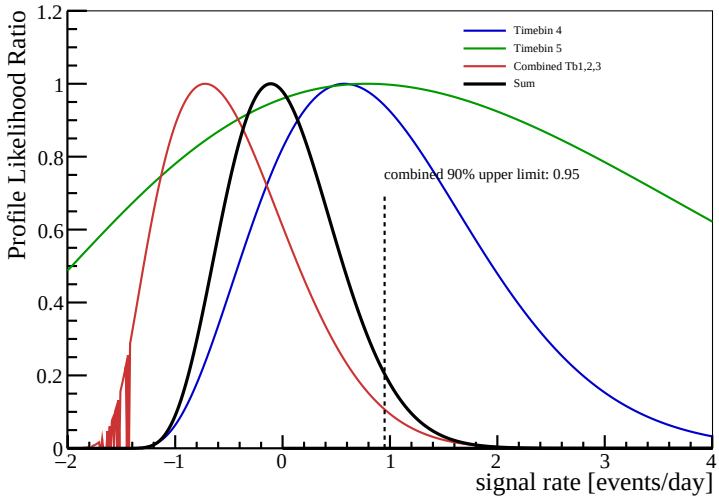

Figure 5.20: Profile likelihood ratios of the individual time bins (colored) and the combined profile. The 90% upper limit is 0.95 events/day. The combined best-fit value and 68% statistical uncertainties are $0.01^{+0.44}_{-0.57}$ events/day.

reflected in the second term. The third term is the full volume of the detector. Any change in fiducial volume is accounted for in the efficiency cuts. $\rho(T, P)$ is the density of water which is a function of its temperature, T and pressure, P. This was taken to be (999.5 $\pm$ 0.5) kg m^{-3}, to account for the 15% higher atmospheric pressure underground and estimated average temperature of the water in the AV [34]. The molar mass of water is known to be 18.015 g/mol which translates to a mass of 2.99146$\times$ 10^{-26} kg for each water molecule. Putting all these numbers together gives a value of $N_{Nucleons} = 2.41 \times 10^{32}$.

To obtain a lower limit on the neutron decay lifetime, we use the relation

$$\tau > \frac{N_{Nucleons}}{S_{90\%}}$$

where $S_{90\%}$ is the 90% upper limit in events/year. Taking the numbers obtained above, we obtain a statistics-only lower limit on the lifetime of the neutron invisible decay modes of $\mathbf{6.95 \times 10^{29}}$ **years**. However, systematic uncertainties have yet to be included and will be the subject of the Section 5.13

5.12 Analysis Verification

A few checks were done to verify that the algorithm is working as intended. The first check was to determine if the profile likelihood distributions were being generated properly. Interestingly, the method of profiling the likelihood ratio described earlier is employed by ROOTs' MINOS algorithm in order to determine asymmetric fit errors of the fit parameters [89]. However, a key difference is that MINOS assumes Wilk's Theorem, that says in the large sample limit, the distribution is comparable to a χ^2 distribution. In practice, MINOS varies the fit parameter being profiled until its likelihood value changes by 0.5 from the best fit value. Thus, we can use MINOS to verify that the widths (defined to be the distance between the upper and lower 68% errors) of the profiles generated using the author's algorithm are close to that returned by MINOS. This test was done on time bin 4, where the author's algorithm returned a fit result for the signal of 0.58 +1.69 - 0.27 events/day to obtain a width of 1.96 (Figure 5.18). For the same fit, MINOS returned a fit value of 0.58 + 1.15 - 0.87 events/day which is a width of 2.02 . Thus, we can see that though the upper and lower errors differ (expected due to large sample limit assumptions in MINOS), the widths of the distributions are nearly identical. Therefore, the author is confident the algorithm is working as intended.

Another check is to determine if the likelihoods are being combined properly. First, three Gaussians were generated, each with semi-arbitrary means and with widths equivalent to the square-root of their means. These three Gaussians represent the profile likelihoods, and are then combined using the author's script. Figure 5.21 shows the result of this combination, along with the 68% error bars.

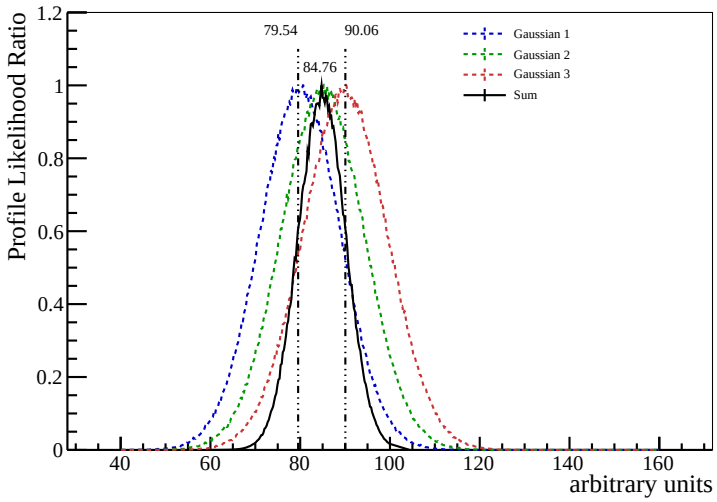

Figure 5.21: Combination of three Gaussians of known mean and width. The result is: 84.76 + 5.30 - 5.22.

This was cross-checked with a second method, where the means of the Gaussians were plotted on a graph, with error bars equivalent to the widths of the Gaussians. A straight line was fit through those points and this is shown in Figure 5.22. If the author's algorithm is working as intended, the mean and 68% error bars from the algorithm should correspond to that obtained from the straight line fit to the points. As can be seen, they agree extremely well, confirming that the author's algorithm is

working.

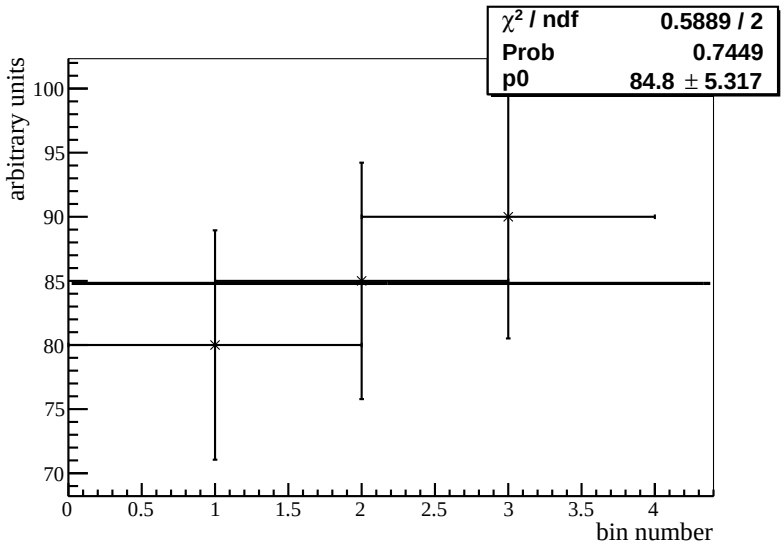

Figure 5.22: Straight-line fit to the three Gaussians. The fit result is: 84.80 ± 5.32

A final check was done by comparing with fits done by a collaborator, Morgan Askins, who performed the analysis presented in the published paper, where unbinned maximum likelihood estimation was used. Besides the difference in algorithms, Askins also uses a different software package as the author (NLopt minimizer) and does not apply KDE smoothing. After ensuring we have the exact same PDF shapes, we performed a fit on a single dataset with agreed on conditions and constraints. Even with identical initial conditions, the total number of events fitted out by the author and Askins differed slightly from each other relative to the total number of data points, shown in Table 5.10. This difference, though seemingly minor, was enough to cause our fits to settle at different best-fit values.

Parameter	Fit (Author)	Fit (Askins)
Atmospherics	$1.68^{+0.18}_{-0.18}$	$1.68^{+0.17}_{-0.18}$
Solars	$2.88^{+0.06}_{-0.06}$	$2.87^{+0.03}_{-0.06}$
Reactors	$0.35^{+0.35}_{-0.35}$	$0.35^{+0.34}_{-0.34}$
Internal Bismuth	$227.09^{+21.31}_{-21.98}$	$239.58^{+21.56}_{-21.56}$
Internal Thalium	$53.41^{+19.25}_{-17.93}$	$51.71^{+18.10}_{-16.55}$
Externals	$20.70^{+7.89}_{-7.59}$	$11.37^{+5.79}_{-4.86}$
Signal	$3.80^{+6.50}_{-5.17}$	$1.23^{+6.47}_{-4.74}$
Total Events	309.9	308.8

Table 5.10: Fit to a data set with a total of 310 events. Note that the intervals are calculated differently in the two fits. In both cases the intervals are found by profiling against the other parameters. In the author's case these are ROOT's "MINOS" errors, which profile and then use Wilk's theorem to assign intervals for fixed values of the likelihood ratio. In Askins' case the errors are similarly profiled, but the interval is the region bounded through a Feldman-Cousins approach.

To investigate this, Askins adjusted his algorithm to a binned fit and after repeating the fit, he obtained the exact same total events as the author. This led us to conclude that the difference came not from the underlying algorithms but from the binned vs unbinned likelihoods methods. While this shows that the author's code is reliable, we are still uncertain about the reason the results differed between binned and unbinned fits. A plausible hypothesis is that by binning the dataset into five 1D spaces, the binned likelihood is evaluated by assuming the bins are independent. However, with five 1D observable spaces which may be correlated, the bins are not completely independent. The unbinned likelihood evaluates the likelihood event-by-event and so does not suffer from this artifact. Additional details are given in [90].

5.13 Systematic Uncertainties

In order to propagate the systematic uncertainties in the observables, the shift-and-refit method was used. As described in Chapter 4, PDFs of the observables are shifted/smeared event-by-event by some specified amount determined by auxilliary measurements performed using N16 calibration data, and the fit to data redone. The difference from the unshifted case is taken as a measure of the systematic uncertainty. For each systematic, the fits to each individual time bin was performed, generating a profile likelihood for each. These were combined and the 90% upper limit was calculated. The difference between this upper limit from the upper limit of the unshifted case is taken as a measure of the systematic.

Unlike Chapter 4, we have three additional systematics to consider in this analysis: systematics due to KDE smoothing, systematics due to insufficient PDF statistics, and systematics from not including a model for the "hotspot". These are discussed in the following subsections. The other systematic uncertainties that were not discussed are treated in the same way as in Chapter 4.

5.13.1 Systematic: KDE

As mentioned at the end of Section 5.8, the smoothing due to applying KDE would change the shape of the PDF significantly, especially at the edges of the distributions. Therefore, to estimate this systematic, an ensemble of fake datasets were generated for each time bin with the source PDF having no KDE applied to it. The fake datasets were generated with the expected background rate of that particular

time bin in order to accurately simulate the statistics of that time bin. The ensembles of each time bin are fitted, and the biases obtained are shown in Table 5.11.

Time bin	Bias [ev/day]
4	0.0646
5	0.0864
Combined 1,2,3	-0.1842

Table 5.11: Fiducial-volume adjusted bias due to KDE smoothing.

To translate this into an overall systematic, the profile likelihoods were shifted before combining into an overall likelihood. The 90% upper limit was then calculated from this overall likelihood and the difference from the nominal case is taken as a systematic. Note that the profiles are shifted depending on the sign of the bias: the profile likelihoods were shifted lower for positive bias but shifted upwards for negative bias.

5.13.2 Systematic: PDF Statistics

As mentioned earlier, there was not enough simulated events for some background classes in order to make PDFs whose statistical uncertainty cannot be neglected. This uncertainty should be estimated as even with KDE, the shapes of the distributions could still differ due to this statistical uncertainty. In order to evaluate this systematic, the contents of the KDE smoothed PDFs (which are binned) are Poisson-fluctuated bin-wise before applying KDE smoothing again. These 'jittered' PDFs were then used to fit to the data and a distribution of the signal fit results was made. This was done for each individual time bin. The width of that distribution i.e. the spread of

the fit results is taken as the systematic. The results are shown in Table 5.12.

Time bin	Width [ev/day]
4	0.142
5	2.614
Combined 1,2,3	0.084

Table 5.12: Width of distribution of fitted signal rate due to fluctuating PDFs.

To obtain an overall systematic, the profile likelihoods of each individual time bin was convolved with a Gaussian with mean=0 and width equal to that in Table 5.12. These smeared likelihoods are combined and the 90% upper limit calculated. As before, the difference of this limit from the nominal case is taken as the overall systematic.

5.13.3 Systematic: Hotspot

As mentioned earlier Section 5.5, an additional systematic has to be assigned for not including a model for the "hotspot". However, due to resource limitations, simulations of these "hotspot" events cannot be generated in a reasonable amount of time required for this analysis. But a decent approximation can still be done. Since this "hotspot" is due to the lack of a cover gas during the data taking period, it is reasonable to assume that its activity is due to the ^{222}Rn decaying ultimately into ^{214}Bi. Therefore, we can utilize the simulations of internal ^{214}Bi as a proxy. To approximately model the distribution of the simulated events in detector space, a cut was done on the truth z-position of the internal ^{214}Bi simulated events. The z-cut was tuned by hand to produce a distribution in the reconstructed z-position of the

surviving data events in the 4-5 MeV energy sideband that resembles the "hotspot" z-distribution for time bin 2, shown in Figure 5.23. After applying the nucleon decay ROI cuts, especially the energy cut, the number of simulated events making it into the ROI is significantly lower. The $\hat{U} \cdot \hat{R}$ and R^3 observables of these surviving events are shown in Figure 5.24 and indeed, they have the same trend as seen in the data i.e. an excess at high R^3 and at $\hat{U} \cdot \hat{R}$ of -1. Notice in the figures that the PDFs formed as a result of lack statistics had a less pronounced excess at -1 $\hat{U} \cdot \hat{R}$ and high R^3.

Regardless, using this proxy as the PDF for the "hotspot", an ensemble of 1000 datasets were created with all the backgrounds at expected rates but seeded with additional events drawn from the "hotspot" PDFs. A livetime of 200 days was used in generating the events in order to get sufficient statistics in the fake datasets. The ensemble was fit with the usual background model without the "hotspot" PDF. A bias of -5.22 signal events was obtained, with 200 "hotspot" events and zero signal events generated, per fake dataset.

Assuming that the characteristics of this hotspot is similar for all the time bins, we can scale this bias to the other time bins. The ensemble was generated using time bin 3 expected background rates. It was also estimated from (posz distribution) that there were approximately 785 "hotspot-like" events in this time bin. To scale this bias to the other time bins, we estimate the number of hotspot-like events in the individual time bins. To do this, the integral of the distributions above zero in Figure 5.24 is subtracted from the integral below zero of that same distribution. This gives a measure of excess events at the top of the detector and we assume all of this

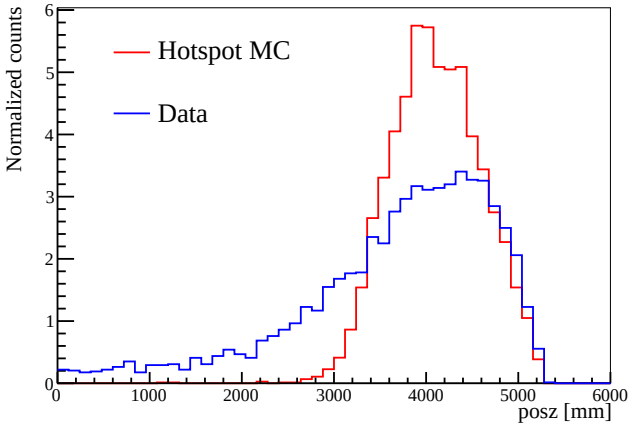

Figure 5.23: "Hotspot" PDF tuned using time bin 2 as a 'calibration', as best as possible.

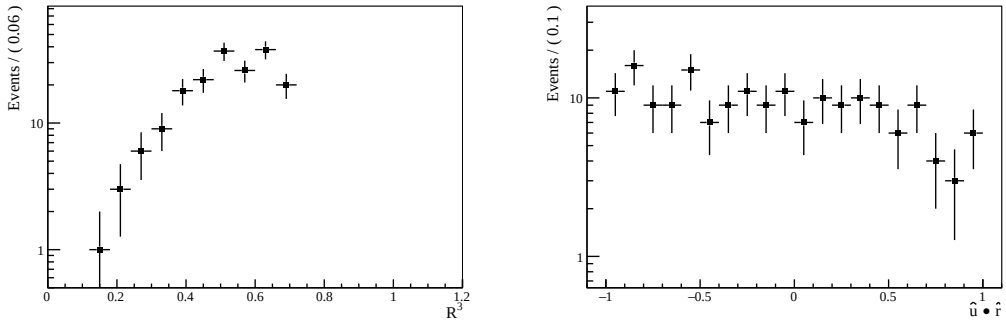

(a) R^3 distribution of "hotspot" PDF. (b) $\hat{U} \cdot \hat{R}$ distribution of "hotspot" PDF.

Figure 5.24: Distribution of "hotspot" PDF in the nucleon decay ROI made from internal Bi MC simulated events.

is due to the "hotspot". Therefore, we can scale the bias obtain from the ensemble test to obtain a rough approximation of the bias due to not including the "hotspot" in the background model for each individual time bin. This is shown in Table 5.13. Given that the "hotspot" effect is rather poorly constrained, including it risks biasing the overall result. As mentioned in Section 5.5, since we do not want to take such a penalty for this systematic, it was decided to exclude time bin 6 from the final analysis.

Time bin	Δ [events]	Bias [events/day]
4	-8	-0.020
5	-89	-0.402
6	-2209	-3.956
Combined 1,2,3	-94	-0.130

Table 5.13: Efficiency adjusted bias due to not including model for "hotspot" background. Δ is excess of events in the top half of the detector compared to the bottom half.

To apply this as a systematic, as in the case for the KDE, the profile likelihoods were shifted before combining into an overall likelihood. The 90% upper limit was then calculated from this overall likelihood and the difference from the nominal case is taken as a systematic.

5.13.4 Breakdown of systematics

The magnitude of the individual systematics as a result from shifting and refitting are shown in Table 5.14. For the last three systematics in the table (PDF Statistics, 'hotspot', KDE correction), the systematic is applied both as a shift and a smearing, essentially doubling the systematic. This was done to take into account the uncertainty in the shift due to the bias as well as imperfect modeling of the systematic uncertainty itself.

Systematic class	90% upper limit [events/day]	systematic value [events/day]
central	0.95	-
smear energy	0.75	± 0.20
scale energy up	0.74	+ 0.21
scale energy down	1.19	- 0.24
shift β_{14} up	0.94	+ 0.01
shift β_{14} down	0.99	- 0.04
scale radial up	0.92	+ 0.03
scale radial down	0.96	- 0.01
shift radial up	0.98	- 0.03
shift radial down	0.91	+ 0.04
smear radius	0.92	± 0.03
shift direction up	0.93	+ 0.02
shift direction down	0.99	- 0.04
PDF Statistics	0.96	- 0.01
'hot spot'	1.00	-0.05 ± 0.05
KDE correction	0.99	-0.04 ± 0.04

Table 5.14: Breakdown of the systematics and their individual contributions. The values in the third column are calculated by subtracting the values in the second column for a particular systematic from the central value. The first value in the third column is a correction in the combined profile whereas the second value is the smearing of the profile.

5.13.5 Combination of systematics

The direct way to combine these systematics would be to quadrature sum all the differences. However, this method does not take into account the upper and lower asymmetry of some of these systematics. In order to account for this asymmetry, the systematic uncertainties are summed using a toy Monte Carlo method. Figure 5.25 shows the distribution after applying this method, which gives 0.312 for the combined systematics. For comparison, directly quadrature summing the second values in the third column in Table 5.14 gives a value of 0.392. This comparison shows that directly

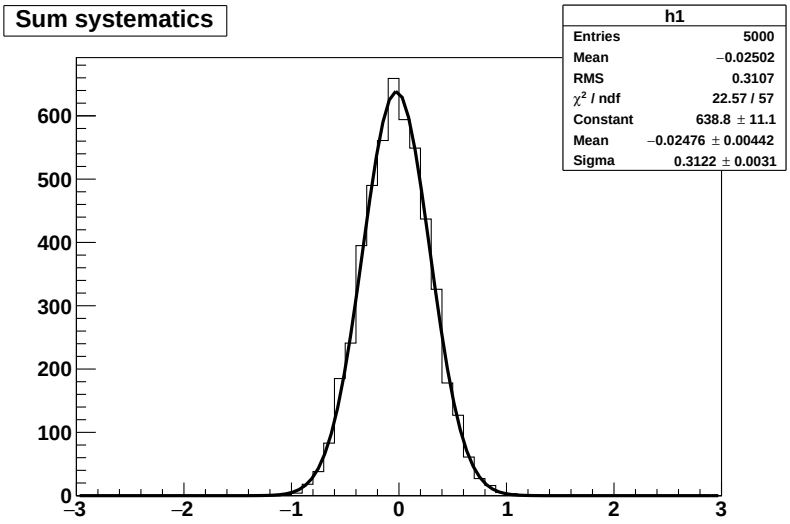

Figure 5.25: Distribution of summed systematic uncertainties using toy Monte Carlo.

quadrature summing over-estimates the total systematic uncertainties by about 20%.

5.13.6 Applying Final Systematics

In order to obtain a final result, we have to shift and smear the combined profile likelihood by the values of the systematics determine in the preceding sections. From Table 5.14, the third column gives a total shift of 0.09 and the combination of the other systematics using the toy Monte Carlo method gives a smearing width of 0.312. Therefore, the combined profile is convolved with a Gaussian with mean 0.09 and width 0.312. The result of this is shown in Figure 5.26.

To obtain a final lower limit on the neutron decay lifetime, we again use the relation

$$\tau > \frac{N_{Nucleons}}{S_{90\%}}$$

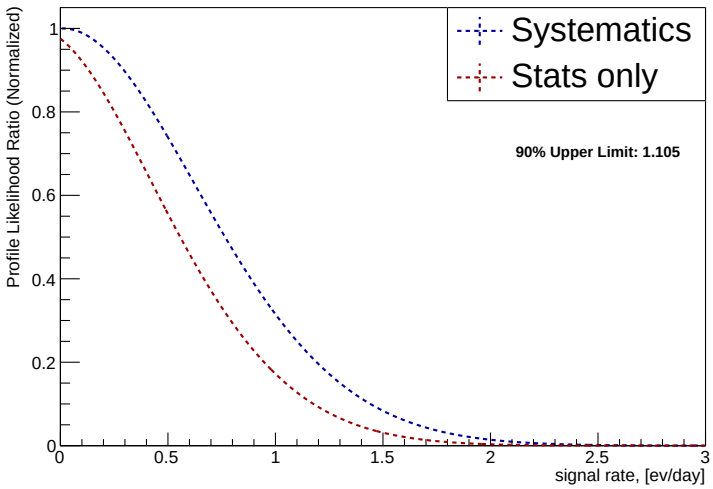

Figure 5.26: Profile likelihood after smearing to include systematic uncertainties. 90% upper limit obtained is 1.105 events/day.

where $S_{90\%}$ is the 90% upper limit in events/year. Taking the value of $N_{Nucleons} = 2.41 \times 10^{32}$ calculated earlier, and the 90% upper limit of the smeared likelihood distribution, we obtain the lower limit on the lifetime of the neutron invisible decay modes including systematics of $\mathbf{5.98 \times 10^{29}}$ **years**. Compared to the previous world-leading value of 5.8×10^{29} years, this is a new world-leading limit.

5.14 Floating Energy Systematics

From the results in Table 5.14, we can observe that the systematics related to energy scale and resolution are the dominant systematics. The estimation of this systematic is also somewhat uncertain due to the nucleon decay ROI being in the tails of the dominant background energy distributions, while the energy systematics are estimated using the peak widths of the calibration data. Recall from Chapter

4 that the energy systematics were determined around the peak of the N16 energy distribution assuming a Gaussian smearing. Therefore, even though the values of the systematics themselves seem reasonable, it may not be representative in the tails of the distributions. This effect is exacerbated due to the fact that only the tails of some background distributions (internal Bi and Tl) make it into the nucleon decay ROI. Thus, evaluating the systematics in the tails of PDFs using values that are not well-modelled in those tails could lead to an over-estimate of the systematics [91].

A solution to this problem is to allow the data to determine the energy scale and resolution systematics. This is done by convolving a Gaussian of variable mean and width with the energy PDFs and allowing the Gaussian parameters to vary in the fit, which represents the energy scale and energy resolution systematics, respectively. Because changing the energy scale and resolution might change the MC events that pass selection cuts and in turn change the shape of the PDFs in other observables, the PDFs of all the other observables would have to be remade after each convolution, which is computationally expensive. However, if the PDFs of those observables do not change much as the energy changes, an approximation that the non-energy PDFs do not need to be remade every time can be made. In order to check the validity of the above assumption, the event energies in the MC were smeared event-by-event using "shift-and-refit" and the magnitudes in Chapter 4, and the other PDFs rebuilt. Since magnitude of the shift is expected to be conservative, and if the non-energy PDFs do not vary much, the assumption would be reasonable, since we are concerned with 1σ level errors. This test was done with internal ^{214}Bi MC, which after event-by-event smearing, was binned in the various observable spaces after the selection cuts were

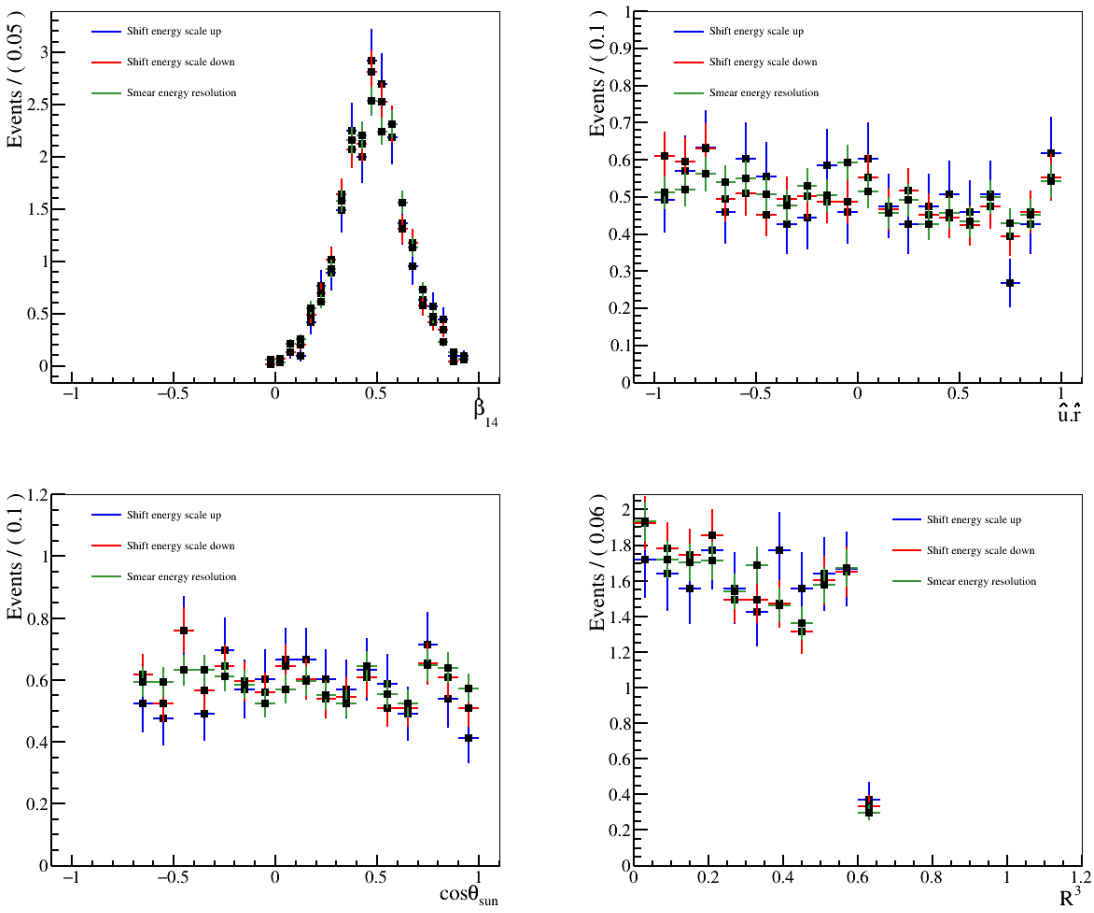

Figure 5.27: Plotting the PDFs of internal water ^{214}Bi after application of energy systematics and selection cuts of the combined time bin 1,2,3.

applied. This is shown in Figure 5.27. By eye, the PDFs look similar and the differences in each individual bin is within the statistical fluctuations of the individual bins.

To verify that the script is able to correctly extract out the parameters of the Gaussian used to smear the PDFs, a bias and pull tests, introduced in Chapter 4, was performed. The PDFs were convolved with a (0,1) Gaussian in energy-space before events were generated from those PDFs. The bias and pull plots of generating

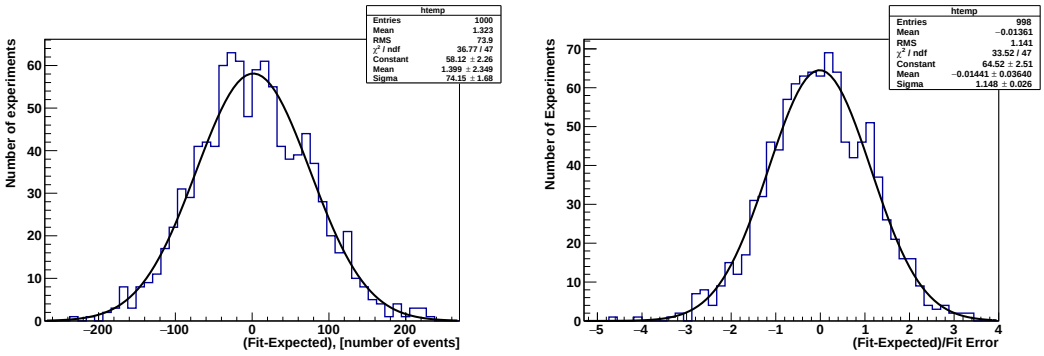

(a) Bias of signal (b) Pull of signal

Figure 5.28: Bias and pull of signal parameter

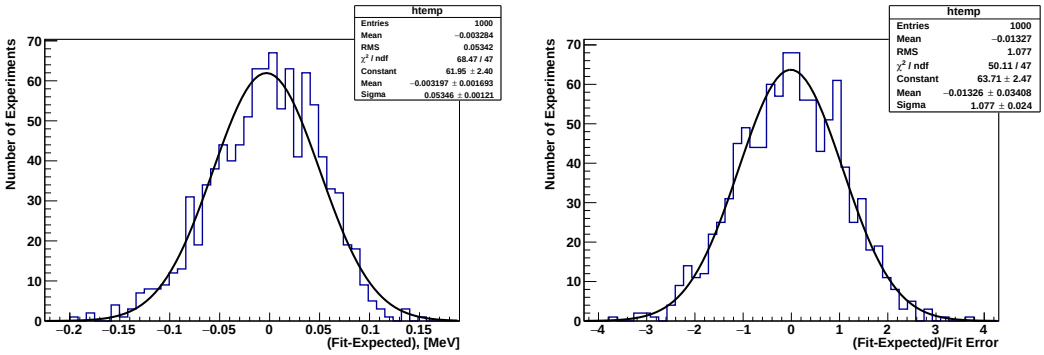

(a) Bias of energy scale parameter (b) Pull of energy scale parameter

Figure 5.29: Bias and pull of energy scale parameter.

and fitting an ensemble of 1000 fake datasets is shown in Figure 5.28, Figure 5.29, and Figure 5.30. This demonstrates that the fit is able to correctly extract the mean and sigma of the Gaussian used to smear the energy PDFs.

5.15 Final Result

The analysis is repeated exactly as described in the preceding sections but with the energy systematics floated unconstrained in the fit. Figure 5.31 shows the individual

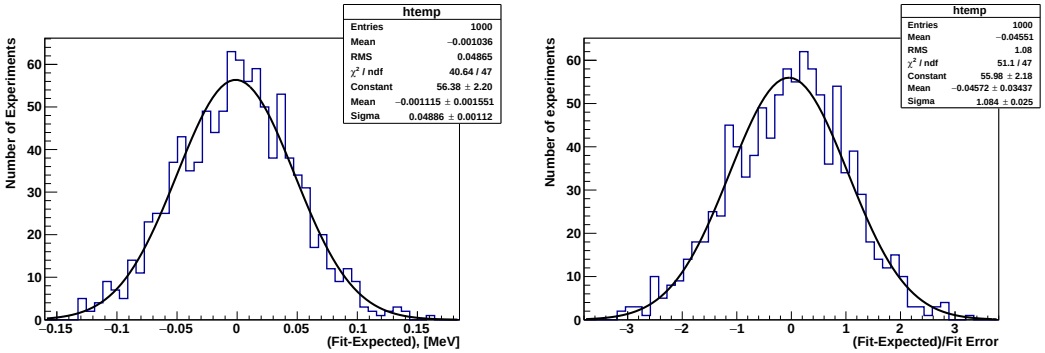

(a) Bias of energy resolution parameter (b) Pull of energy resolution parameter

Figure 5.30: Bias and pull of energy resolution parameter.

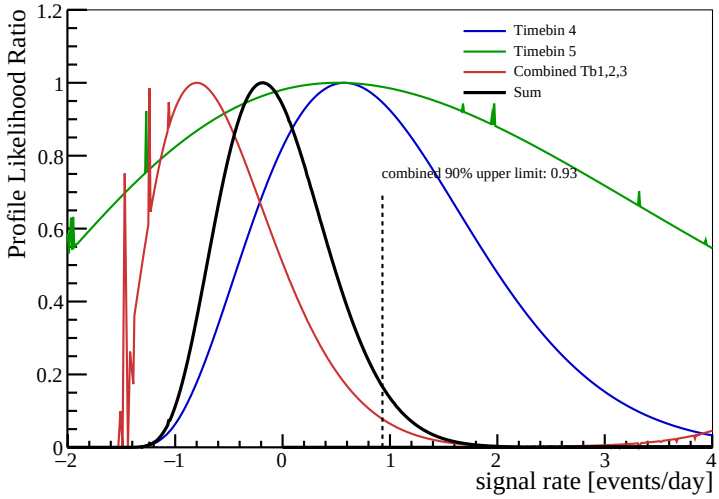

Figure 5.31: Profile likelihood ratios of the individual time bins (colored) and the combined profile. The 90% upper limit is 0.93 events/day. The combined best-fit value and 68% statistical uncertainties are $0.01^{+0.35}_{-0.63}$ events/day.

likelihoods along with the combined likelihood for the central fit. The floated energy systematic values returned for each individual time bin fit was compatible with that obtained from the ^{16}N analysis within fit uncertainties returned by MINOS. It should be noted that in the tails of the distributions, which is most of the backgrounds, the energy scale and energy resolution are highly (anti-)correlated, since both have a similar affect on the PDF shape.

An obvious feature in Figure 5.31 is the fluctuations at the tail ends of the individual likelihoods. Those correspond to bad fits that occurred as the algorithm scanned in that region. A check was done on random points for the combined time bin at very positive signal rates and those points had very negative values for internal Bi, which was unphysical. Tests indicate that these unphysical likelihood values far from the best fit have no effect on the combined likelihood. Table 5.15 shows the breakdown of the systematics. Figure 5.33 shows the profile likelihood after the systematics have been applied.

Taking the value of $N_{Nucleons} = 2.41 \times 10^{32}$ calculated earlier, and the 90% upper limit of the smeared likelihood distribution, we obtain the final lower limit on the lifetime of the neutron invisible decay modes of **6.91×10^{29} years**. It should be noted that this result is about a factor of 2 better than [21] and this could be attributed to the re-optimization of the fiducial volume and the rejection of data sets that had significantly elevated levels of backgrounds (time bin 6). Compared to the statistics-only result calculated earlier, this value is only slightly worse, meaning that the systematic uncertainties are not dominant and instead the result is dominated by

Systematic class	90% upper limit [events/day]	systematic value [events/day]
central	0.93	-
smear energy	-	-
scale energy up	-	-
scale energy down	-	-
shift β_{14} up	0.93	$\pm$ 0.00
shift β_{14} down	0.97	- 0.04
scale radial up	0.87	+ 0.06
scale radial down	0.93	$\pm$ 0.00
shift radial up	0.94	- 0.01
shift radial down	0.91	+ 0.02
smear radius	1.00	$\pm$ 0.07
shift direction up	0.87	+ 0.06
shift direction down	0.96	- 0.03
PDF Statistics	0.94	- 0.01
'hot spot'	0.97	-0.04 $\pm$ 0.04
KDE correction	0.95	-0.02 $\pm$ 0.02

Table 5.15: Breakdown of the systematics and their individual contributions with floating systematics. The values in the third column are calculated by subtracting the values in the second column for a particular systematic to the central value. The first value in the third column is a shift in the combined profile whereas the second value is the smearing of the profile.

statistics. Table 5.16 summarizes all the results obtained so far.

	stats only [$\times 10^{29}$ years]	with systematics [$\times 10^{29}$ years]
no floating systematics	6.95	5.98
floating systematics	7.10	6.91

Table 5.16: Summary of the results obtained for the lower limit of the lifetime for "invisible" neutron decay.

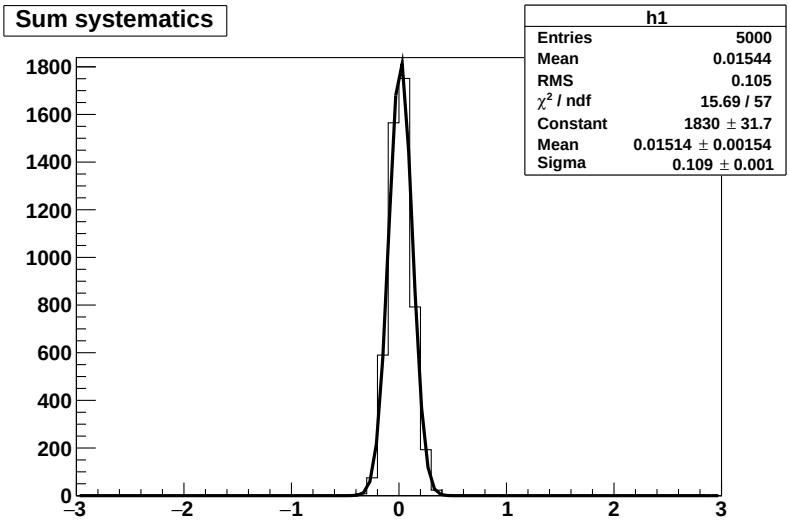

Figure 5.32: Distribution of summed systematic uncertainties using toy Monte Carlo, giving a summed systematic value of 0.109.

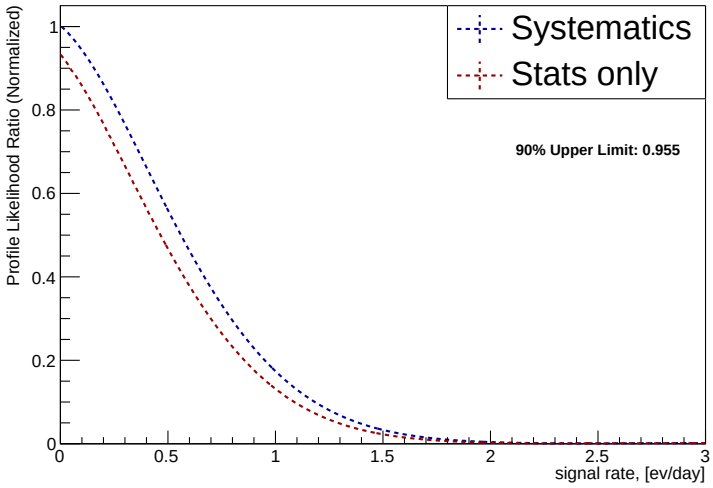

Figure 5.33: Profile likelihood after smearing to include systematic uncertainties. 90% upper limit obtained is 0.955 events/day.

5.16 Future Work

As described in Chapter 4, once the cover gas system was operational, a steady period of low-background water data was taken. This had a livetime of 190.31 days and with internal backgrounds determined to be about an order of magnitude lower than the previous data sets analyzed so far, this low background dataset could potentially set an even better limit. This "new" data set is still blinded; part of the motivation for the "modular" nature of the analysis presented here is to make it straightforward to incorporate the new data into the analysis once blindness is lifted. It would be good to perform a preliminary estimate of the sensitivity of this dataset, where the sensitivity is defined to be the median value of 90% upper limits from an ensemble test (the "90/50" sensitivity).

Background class	Expected rates [$\times 10^4$ events/day]
Bi AV	3.50
Tl AV	0.41
Bi Ext	36.16
Tl Ext	1.07

Table 5.17: Expected rates of the various external background components [92].

To perform this analysis, the fake datasets making up the ensemble were generated with internal background rates from Chapter 4. Since the external background analysis has yet to be finalized, the external background PDFs were combined at nominal rates, shown in Table 5.17. The rates of all the other backgrounds are assumed to be the same (solar neutrinos, atmospheric neutrinos, reactor neutrinos). The fake datasets were fit in exactly the same prescription as has been described so

far (without floating energy systematics) and the distribution of 90% upper limits is shown in Figure 5.34. The sensitivity was found to be 0.487 events/day and converting this value to a lower limit for neutron decay lifetime gives $\mathbf{1.36 \times 10^{30}}$ **years**. Thus, we expect the lower limit of the neutron decay lifetime to further improve by an additional factor of 2.

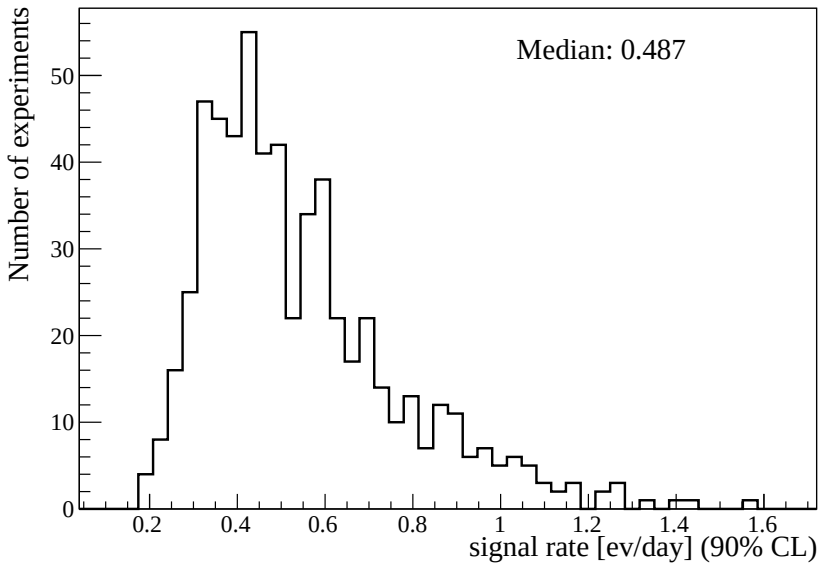

Figure 5.34: Distribution of 90% upper limits from an ensemble size of 600 fake datasets. Systematic effects are not included.

When the blindness restriction is lifted by the collaboration, the analysis described thus far will be repeated. The results will then be statistically combined with this new result to obtained a combined limit by combining the profile likelihoods from both data sets before calculating a new upper limit. However, it is possible to obtain an estimate of the combined sensitivity for the "old" and "new" data by combining the summed profile likelihood in Figure 5.20 and the individual profile likelihoods

from the ensemble test described in the previous paragraph. The 90% upper limit is then computed and binned, and the median calculated. The resulting sensitivity is shown in Figure 5.35. This translates to $\mathbf{1.57 \times 10^{30}}$ **years** lower limit on the lifetime of invisible neutron decay, a further 13% improvement. Therefore, the "old" dataset analyzed in this thesis is expected to have a noticeable contribution to the final analysis once blindness is lifted.

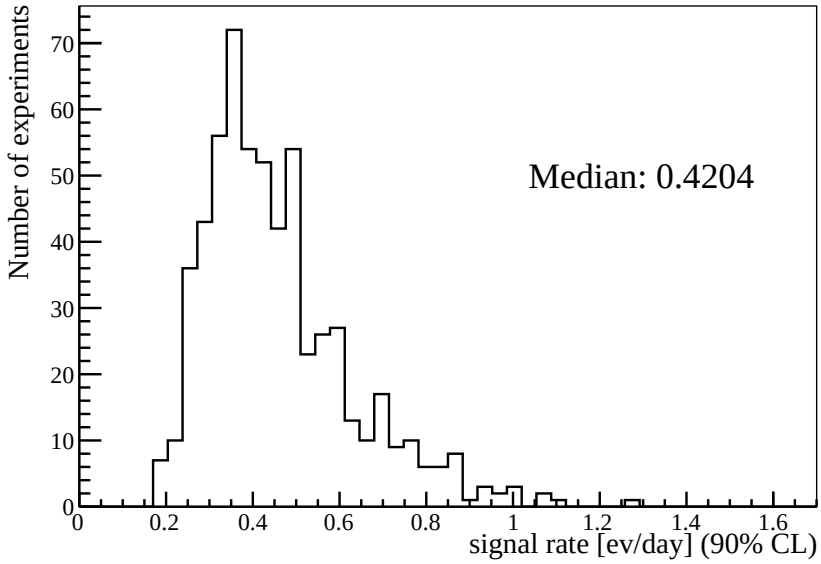

Figure 5.35: Distribution of 90% upper limits from an ensemble size of 600 fake datasets whose profiles are combined with the summed profile in Figure 5.20. Systematic effects are not included.

As mentioned in the introduction of this chapter, the methodology developed in this chapter will also be applied to the other "invisible" nucleon decay modes as well, where similar gains are expected.

Chapter 6

X-Ray Fluorescence (XRF)

Before returning to SNO+, I didn't even know where tellurium was on the periodic table.

A. Wright, 2020

As mentioned in Chapter 1, the main physics goal of SNO+ is neutrinoless double-beta decay using ^{130}Te, an isotope of tellurium, loaded into a liquid scintillator cocktail. However, due to the novelty of the loading method, much research and development had to be done in order to verify its reliability. One major factor to be monitored during in this effort is the concentration of tellurium in the cocktail. A quick and affordable method to check the concentration of tellurium at various stages of the R&D was needed. Furthermore, when the final cocktail is filled into the detector, an expedient method to check the tellurium concentration at various points in the purification/mixing process is an important quality assessment tool. This section will describe the author's work in developing a method to utilize X-Ray fluorescence (XRF) for this purpose. The technique developed by the author has now been taken on by the SNOLAB Scientific Support group, who are working to further refine and more precisely calibrate the measurements for use during the SNO+ tellurium loading

phase.

6.1 Physics of XRF

One of the possible interactions of gamma rays with matter is the photoelectric effect, where an atom or molecule fully absorbs the gamma ray and ejects an electron from one of its orbitals. This leaves the atom in an unstable state. An electron from a higher orbital then falls into the "hole" left behind by the ejected electron and in so doing releases a photon whose energy is the difference between the two orbitals. The energy is characteristic of the atom involved due to unique energy levels. More detailed information can be found in [93] and in [43]

A word on notation of XRF spectral lines. The notation most commonly used is called the Siegbahn notation. A "K emission line" is when an electron falls to the K-shell (principal quantum number 1). The K-line can be divided into K_α and K_β. K_α is when the transition starts from the 2p orbital of the L-shell (principal quantum number 2). K_β emissions, similarly, are by electrons that come from a 3p orbital of the third or "M" shell (with principal quantum number 3).

The 2p orbital of the L-shell is actually a doublet due to spin-orbit interactions, resulting in two slightly different energy levels. This results in two different transitions for K_α: $K_{\alpha 1}$ and $K_{\alpha 2}$, with $K_{\alpha 1}$ coming from a higher energy level than $K_{\alpha 2}$. $K_{\alpha 1}$ tends to be of higher intensity than $K_{\alpha 2}$ and so it would be ideal when measuring low concentrations. In an analogous manner, the L-lines come about as electrons in the M-shell fall into the L-shell. All this is shown in Figure 6.1.

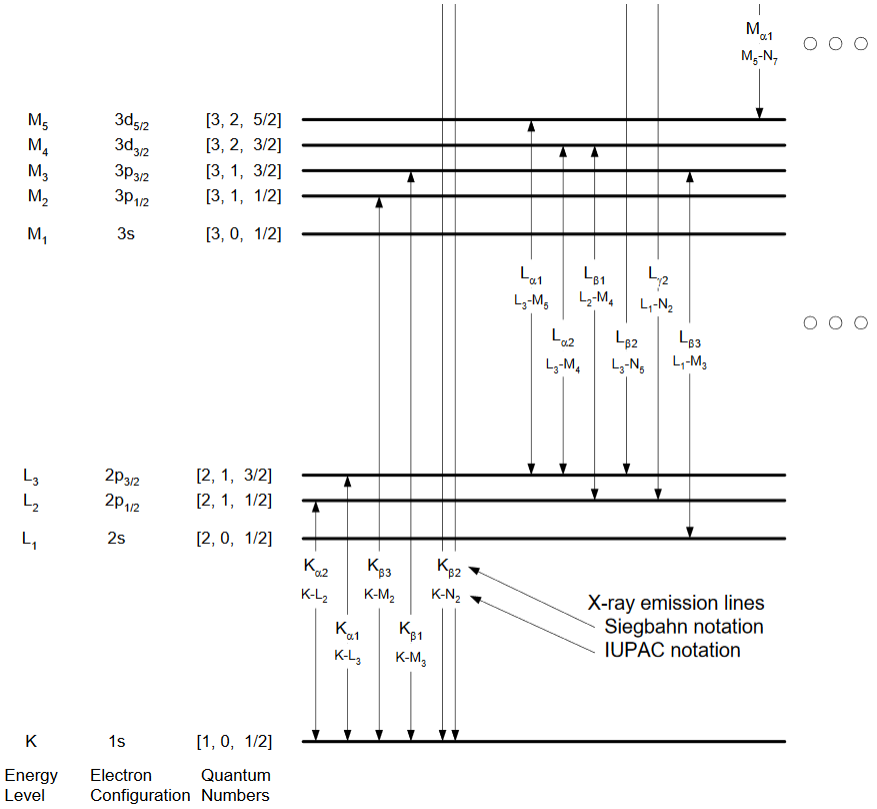

Figure 6.1: Image from [94] elucidating the Siegbahn notation.

6.2 Hardware at Queens

The work here was done together with the invaluable support and guidance of Dr. Herbert Shurvell from the Arts Conservatory Department of Queen's University. The XRF machine used here is a commercial machine by Bruker (Tracer series), shown in Figure 6.2. It is a handheld unit that can be mounted on a stand to perform bench-top analysis. It generates X-rays via a Rh target X-Ray tube, wherein electrons are accelerated towards a Rh target and upon collision some of the electron's kinetic energy is converted into radiation (X-rays in this case). This process is known

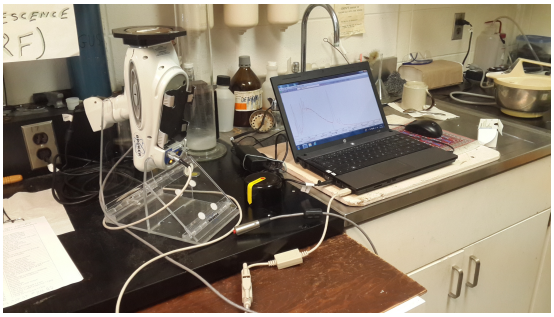

Figure 6.2: The handheld XRF machine in the bench-top configuration. It is attached to a laptop that runs the data acquisition software and displays the energy spectra in real time. The red button is a manual start-stop switch attached to a wire that is about 1m in length. However, during operations, a metal cap covers the window and the sample so the incidences of stray X-rays are minimal to begin with.

Figure 6.3: Picture of the fully assembled sample cup. New cups are used for every sample to avoid contamination.

as bremsstrahlung. The X-rays then irradiate the sample sitting at the sample window, which stimulates atomic emission. The emitted characteristic X-Rays are then collected via a silicon drift detector (SDD) which is Peltier cooled. In our specific XRF machine, the X-ray tube was operated with a tube voltage of 40kV and tube current of 30μA. A higher tube voltage would enable excitation at higher energies (40kV has a theoretical maximum at 40keV) and higher tube current would increase the overall intensity of X-ray generation. The energy resolution of the SDD was on the order of 0.1keV at 4keV.

In order to hold the liquid sample, sample holders along with Mylar sheets were purchased from SCP Science. The sample holders have an outer diameter of about 39.3 mm and the Mylar sheets are 3.6 μm thick. Different dimension holders and Mylar sheets can be used as well but it has to be consistent across analysis and calibration samples. Mylar was used because it is has a low probability of absorbing X-rays. In order to make the cup, a sheet of Mylar (just big enough to cover the diameter of the cup) was torn from the roll and placed over the cup. The ring of the cup was then carefully pushed into place. If the Mylar become creased, the process was repeated [1]. The uneven thickness due to the creases could possibly cause different dispersion effects that can cause systematic variation in samples. An example of a fully assembled sample cup is shown in Figure 6.3

6.3 Procedure

About 1ml of the sample to be analyzed was pipetted into the sample holder. This 1ml was chosen semi-arbitrarily just so that the sample evenly covers the bottom of the cup, for this particular size of cup. A test of different liquid depths in the cup showed no difference in X-ray intensity so we decided to stay with 1ml, which has the benefit of minimal sample usage. This step was done carefully to minimize bubbles which can affect the X-ray attenuation. Any bubbles were carefully popped with the pipette.

[1] Quite uncommon, based on author's experience.

The cup and sample was then placed onto the XRF and scanned. The scan time can be varied but about 20 seconds was found to be sufficient to acquire enough data for analysis. The XRF is attached to a computer which updates the spectra live, so this can be decided on the fly. For samples suspected to have a low concentration of tellurium, the scan time can be increased. During analysis, the counts in the detection channels are normalized to unit time. A background sample was also scanned each time and the spectrum subtracted from the spectrum of the sample under investigation. The reference sample consists of only the matrix the tellurium is in. For example, if were looking at aqueous tellurium, the reference sample would be ultrapure water.

For the analysis, a software called ORIGIN was used. The .csv file generated by the XRF machine is loaded into this software and the graph of the raw spectrum is plotted. The raw counts is divided by the live time of the scan to normalize with respect to scan time. Tellurium has four specific XRF energy peaks, listed in Table 6.1.

Line	Energy(keV)
$L_{\alpha 1}$	3.768
$L_{\beta 1}$	4.029
$K_{\alpha 1}$	27.473
$K_{\beta 1}$	30.993

Table 6.1: List of XRF energies for tellurium, taken from [95]

The $L_{\alpha 1}$ and $L_{\beta 1}$ energy lines are the most intense (shown in Figure 6.4) and so all analysis is done on these two lines. However, the other two energies are checked visually on the spectra to confirm the presence of tellurium. The actual quantification

was done using the lower energy lines.

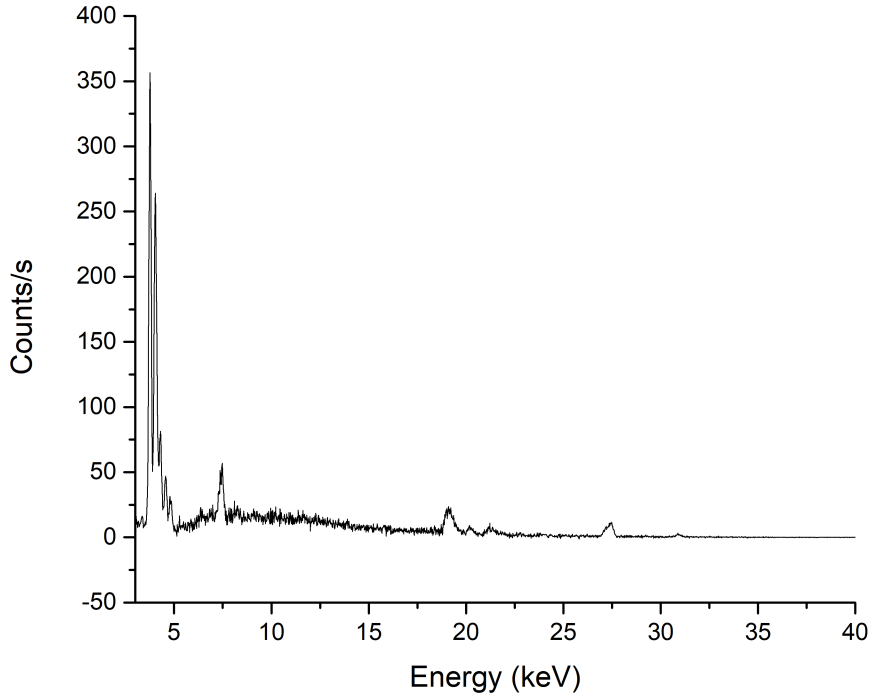

Figure 6.4: XRF spectra of a 0.5% Te sample.

Since we only need the lower energy lines, the data range from 3.2-4.7 keV was isolated from the rest of the spectra. Three Gaussians, one for each peak, was fitted to the three prominent peaks present. Two smaller peaks at about 4.3keV and 4.6keV are also observed in the spectra: these are the higher order emissions of tellurium. The peak at 4.6keV is always very much weaker than the peaks of interest and so it was not fitted.

A sample spectra and the fit are shown in Figure 6.5. The Gaussian formula takes

the form:

$$y = y_0 + \left(\frac{A}{\sqrt{\frac{\pi}{2}}}\right) \exp\left\{-2\left(\frac{x - x_c}{w}\right)^2\right\}$$

where w≡ FWHM , A≡ area under the peak, x_c ≡ mean energy of peak.

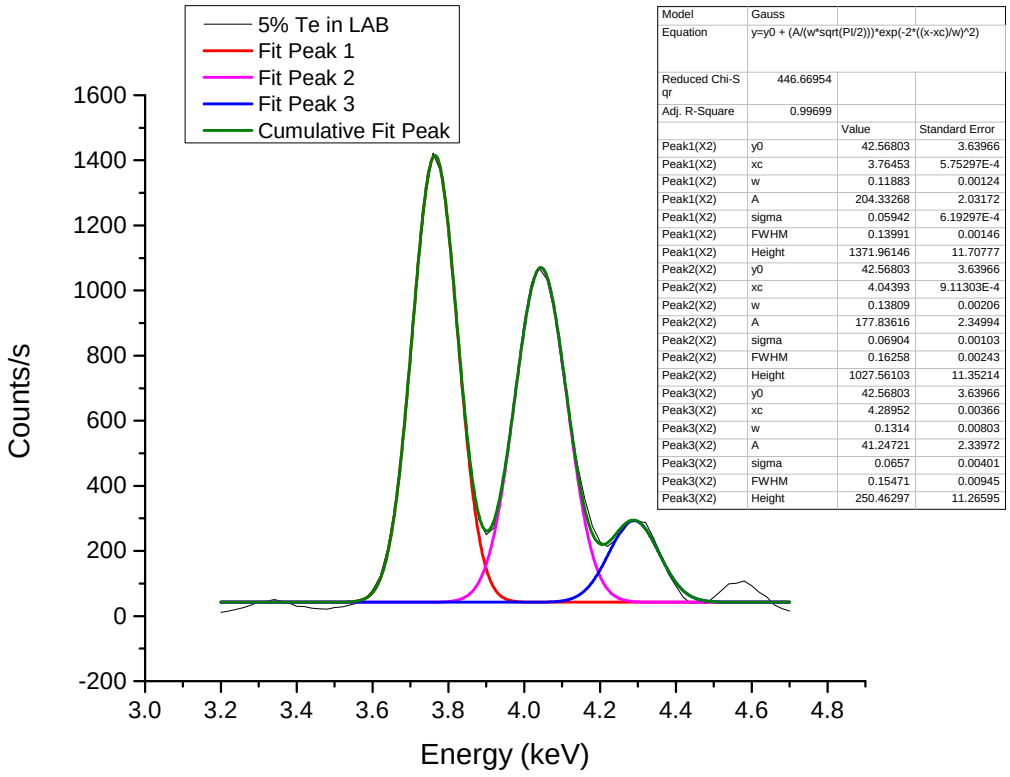

Model	Gauss		
Equation	y=y0 + (A/(w*sqrt(PI/2)))*exp(-2*((x-xc)/w)^2)		
Reduced Chi-Sqr	446.66954		
Adj. R-Square	0.99699		
		Value	Standard Error
Peak1(X2)	y0	42.56803	3.63966
Peak1(X2)	xc	3.76453	5.75297E-4
Peak1(X2)	w	0.11883	0.00124
Peak1(X2)	A	204.33268	2.03172
Peak1(X2)	sigma	0.05942	6.19297E-4
Peak1(X2)	FWHM	0.13991	0.00146
Peak1(X2)	Height	1371.96146	11.70777
Peak2(X2)	y0	42.56803	3.63966
Peak2(X2)	xc	4.04393	9.11303E-4
Peak2(X2)	w	0.13809	0.00206
Peak2(X2)	A	177.83616	2.34994
Peak2(X2)	sigma	0.06904	0.00103
Peak2(X2)	FWHM	0.16258	0.00243
Peak2(X2)	Height	1027.56103	11.35214
Peak3(X2)	y0	42.56803	3.63966
Peak3(X2)	xc	4.28952	0.00366
Peak3(X2)	w	0.1314	0.00803
Peak3(X2)	A	41.24721	2.33972
Peak3(X2)	sigma	0.0657	0.00401
Peak3(X2)	FWHM	0.15471	0.00945
Peak3(X2)	Height	250.46297	11.26595

Figure 6.5: Sample spectrum from 3.2 - 4.7 keV with Gaussian fit. The dark green line represents the total fit while the different color lines each represent a different Gaussian. The mean of each peak is checked to make sure it corresponds to the expected energy. For example, xc for Peak1 matches the energy value for $L_{\alpha 1}$, and so w for Peak1 and A for Peak1 values correspond to the $L_{\alpha 1}$ peak.

From this form, we can read off all the key information, the main one being the

area of the peak fitted at a particular mean energy.

6.3.1 Calibration curves

In order to determine the concentration of Te in an unknown sample, calibrations first have to be made. Tellurium of known amount by mass is diluted into a solvent/cocktail, and samples with different concentrations of tellurium are prepared. Each sample is then analyzed, and intensity (area under the Gaussian fit) vs Te concentration (by mass) is plotted.

It is important that the sample of unknown Te concentration and the calibration samples consists of the same solvent/cocktail. Due to higher order absorption/emission effects, the composition of the solvent the Te is in can affect the intensity of the emitted characteristic X-rays. An example of this can be seen comparing aqueous Te solutions with Te dissolved in LAB-butendiol mixtures. Figure 6.6(a) and Figure 6.6(b) show the two calibration curves. Even though they span roughly the same range, the calibration curves are not identical, as can be seen in the different fit results to an exponential with saturation. The saturation at higher concentrations is due to self-absorption due to the medium the tellurium is in.

Another important point to note is that the calibration curve is only accurate in the range of the calibration samples. So, if an unknown sample lies outside the range of the calibration curve, it will rely on the assumption that the extrapolation from the fitted analytical function is accurate at that range. To mitigate this, more

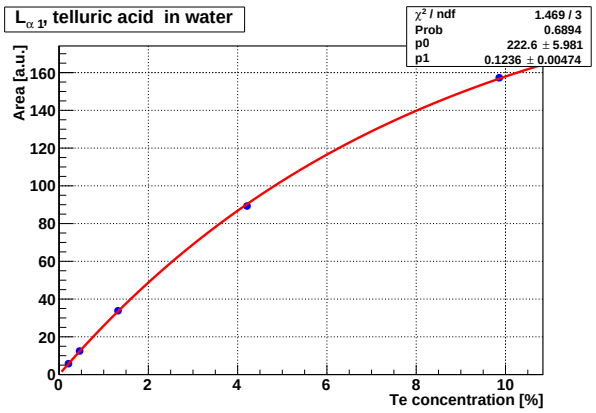

(a) Calibration curve for telluric acid dissolved in water. The plot shows the area under the $L_{\alpha 1}$ peaks.

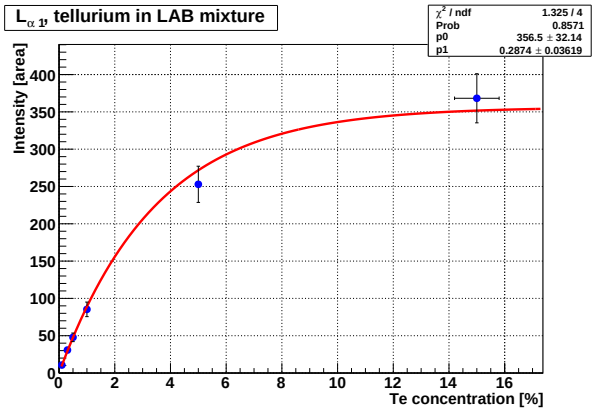

(b) Calibration curve for telluric acid dissolved in LAB-butanediol. As before, the plot shows the area under the $L_{\alpha 1}$ peaks.

Figure 6.6: Comparing two calibration curves: one for water matrix, the other for LAB-butanediol matrix. The fit function used is $p0 * (1 - e^{-p1 * x})$. Some error bars are too small to be seen.

calibration samples would have to be made to cover that range.

6.3.2 Other uses of XRF - Stability

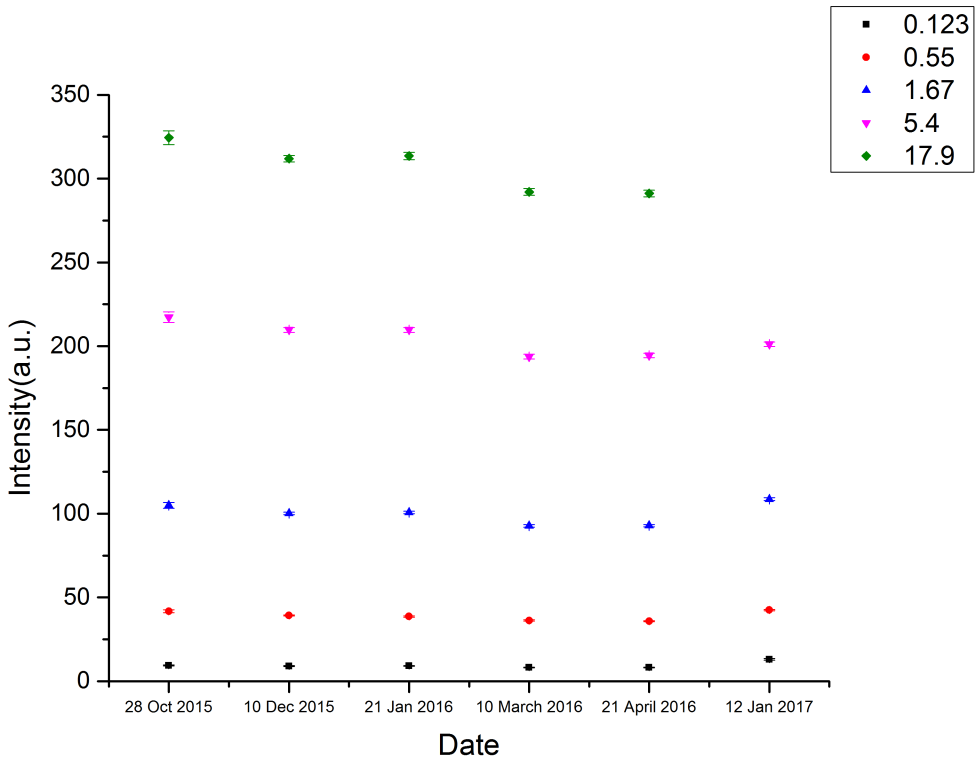

Figure 6.7: Stability test results over a period of time, looking at the $L_{\alpha 1}$ peak. The error bars are statistical only, propagated from the calibration curve.

During the R&D phase on how to load Te into LAB, one of the important factors was the stability of the mixture. Stability here refers to the distribution of Te over a period of time, that is, does the Te stay homogenously mixed in the cocktail? XRF was done on the same samples over a period of time and the concentration of Te

plotted as a function of time, shown in Figure 6.7. As can be seen, the Te concentration is pretty consistent over the time period. However, as R&D progressed, the cocktail and the synthesis procedure has changed dramatically and so this test has been discontinued. However, it was an important result in the early phase of the R&D that prompted further work down this path.

6.3.3 Other uses of XRF - Material Compatibility

Another important aspect of the tellurium-LAB mixture (Te-Diol) was its compatibility with materials that it might come in contact with during transport and processing in SNOLAB. In particular, metals could leach off into the cocktail. To test this, samples of various pure metals were placed in small jars containing the mixture and let sit for a period of time. XRF was done periodically on them to check for deviations from the starting spectrum. Particular attention was paid to the tellurium peaks. Samples of stainless steel, aluminum, steel, copper, and brass were placed in vials and partially filled with the Te-Diol. A vial of the Te-Diol used was also prepared as the reference. Samples were made on 19th November 2015 by Caleb Miller. Scans of the liquid complex were done at certain intervals of time to look for any change in composition of the liquid complex.

From Table 6.2, it is seen that there is a drastic reduction of Te in the copper and brass samples as the samples were left for longer periods, whereas the other samples showed little variation. The copper and brass samples had obvious discolorations (greenish blue) even on 10th Dec 2015. This discoloration grew more concentrated

Date	Area					
	Ref	S.S	Al	Steel	Cu	Brass
10 Dec 2015	176.81 ±1.23	177.26 ±1.24	181.38 ±1.16	182.63 ±1.20	179.99 ±1.25	173.48 ±1.14
29 Jan 2016	175.23 ±1.17	176.13 ±1.15	179.08 ±1.26	178.70 ±1.16	145.93 ±1.00	130.31 ±0.89
8 March 2016	164.41 ±1.05	162.24 ±1.09	-	-	-	-
7 July 2016	167.46 ±1.16	149.71 ±1.06	-	-	-	-

Table 6.2: Areas of $L_{\alpha 1}$ Te peak for the various samples.

as time went on. For the non-copper and non-brass samples (except the reference), there was no discoloration on 10th Dec 2015. On 29th Jan 2016, there was slight but not obvious yellowish discoloration. However, on 7th March 2016, the yellowish discoloration was obvious. The cause of this is still unclear but it is most likely the metals facilitating the oxidation of LAB.

Another metal whose compatibility is more of a concern is nickel. This is due to the fact that the previous SNO neutral current detector (NCD) naming plates were made of nickel, and they are still affixed inside the acrylic vessel. A sample was prepared by Szymon Manecki in the same manner as above but with an original nickel NCD plate. Table 6.3 summarizes the results.

The '9 Feb 2016' sample, along with the reference, was diluted equally with LAB by Szymon in order to make a sufficient amount of sample for the XRF. This was because the sample did not have enough Te-Diol for the XRF measurement. From

Date	Area	
	Ref	Ni
4 Jan 2016	17.95 ±1.69	11.74 ±3.20
9 Feb 2016	16.39 ±2.89	14.90 ±3.46

Table 6.3: Areas of $K_{\alpha 1}$ Ni peak at 7.478 keV.

Table 6.3 , we can see that there is no difference between the reference and the sample, within error. Therefore, we can say that, within error, no nickel is being leached into the Te-Diol.

6.4 Work at SNOLAB

The work describe here was done together with Francine St. Jacques, a chemical technologist at SNOLAB. The results described here are from [96].

The ultimate goal of all the work and procedures developed in the preceding sections was to use XRF as part of the quality checks of the actual synthesis and purification processes to be carried out at SNOLAB. To that end, SNOLAB has purchased a bench-top XRF machine called Epsilon 1 by Panalytical. This machine is more technologically advanced than the handheld device presented in the previous sections, coming with a measurement/analysis software right in the machine itself. In essence, one could make a measurement and get quantitative results without any other external machine. However, the basic procedure is the same as laid out above: create calibration samples with the same matrix as the sample to be analyzed, create

a calibration curve from said samples, and use that calibration curve to analyze the unknown sample.

The goal of the Te-loaded phase of SNO+ is to load 0.5% of Te by mass into the detector. In order to achieve this, the Te-loaded cocktail is to be synthesized into 45 smaller batches of about 0.01% Te by mass. These are then loaded batch by batch into the detector until the desired concentration is achieved. Therefore, XRF is an excellent tool to quickly quantify the Te concentration not only in the final batch but also in the various stages of the purification/synthesis process. With this in mind, the XRF machine has to be able to repeatedly measure a huge concentration range of Te, from the order of 40% during the synthesis process to 0.01% level in the final step.

Similar to what was done in the previous sections, the tests were started with telluric acid dissolved in water, as this is the easiest and quickest kind of sample to make. The main goal with these tests was to verify the machine's accuracy in making measurements and to get an idea of the limit of detection of the machine. This also has an application in the telluric acid purification process, as part of the procedure involves dissolving the telluric acid crystals in ultrapure water. It also serves as a starting point to familiarize the operators with the brand new machine as well as to transfer the author's liquid sampling technique knowledge to the SNOLAB scientific support group.

Calibration samples of 1%, 5%, 10%, 15%, and 20% tellurium in water were made and scanned with the machine. The counting time was 600s per sample, and each

Te conc [%]	Intensity [counts/s]
1	101.17 ± 0.45%
5	381.38 ± 0.26%
10	594.53 ± 0.12%
15	728.64 ± 0.15%
20	826.08± 0.22 %

Table 6.4: Average intensity and corresponding standard deviation (in %) as a function of tellurium concentration in water. As can be seen, the spread in measurements is less than 1%, showing the consistency of the machine.

Te conc [%]	Accuracy [%]
4	2.54 ± 5%
12	2.06 ± 5%
18	2.07 ± 5%

Table 6.5: Average accuracy as a function of tellurium concentration in water. Accuracy is defined as (accepted-measured/accepted) * 100. As can be seen, the average accuracy is about 2% for the different concentrations. The 5% in the table is related to the accuracy of the volumetric flask. The samples were prepared individually and not sequentially diluted.

sample was 5mL. After scanning through the set of samples once, the process was repeated. This process was repeated again about 11 days later, for a total of three measurements per sample. The idea was to get a handle on the spread of the measurements and the consistency of the machine. The results, shown in Table 6.4, demonstrate the level of precision achievable by the machine.

With the calibration sample measurements loaded into the machine's software, more samples were prepared in order to test the accuracy of the machine. Samples of 4%, 12% and 18% were made. Each was scanned four times. The average percent difference from the accepted value is shown in Table 6.5

Once it was demonstrated that the measurements work well with telluric acid in water, the tests progressed into a matrix very similar to the final product: tellurium in 1,2- butanediol (TeDiol). Unlike the aqueous samples, these samples are more time consuming to manufacture as it involves various stages of heating and mixing with nitric acid. As before, the calibration samples of known concentration were prepared and scanned. At this stage, it was found that the concentration of tellurium estimated by XRF changed depending on the location of where the sample was drawn from the main solution (top vs bottom). This effect is shown in Figure 6.8. It was determined that the sample was not well mixed during preparation leading to this effect.

Due to the length of time needed to prepare the samples, the tests were not able to be fully completed by the time the author left SNOLAB. In addition, the chemistry support group that has been supporting this effort had to divert attention to more urgent work. Further work to be done, other than the issue of mixing, is to repeat the precision and accuracy tests as was done for the aqueous tellurium.

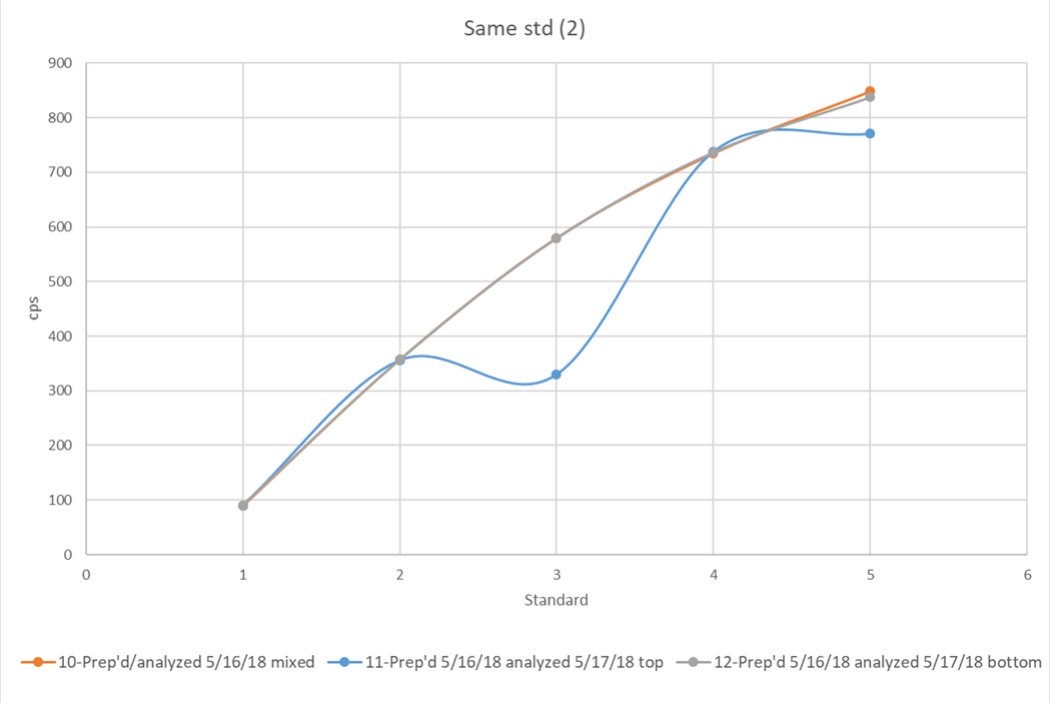

Figure 6.8: Measurement of TeDiol calibration samples. The orange curve is from solution that was prepared and analyzed on the same day. The blue curve is the same sample solution but analyzed the following day and drawn from the top part of the vial. The grey curve is similar but drawn from the bottom instead. This shows that the concentration is changing at the top portion, hinting that the calibration sample stratifies over time and needs to be mixed.

Chapter 7

Conclusion

Get your degree and get out already.

P. Skensved, 2016

An analysis of the internal backgrounds in the water phase of SNO+ was performed in order to provide a direct measurement of the radioactive backgrounds in the water phase. Table 4.6 gives the measured concentrations of U and Th of the data set before the low Rn nitrogen cover-gas was commissioned. These were used as input to the published nucleon decay analysis. After the cover-gas was commissioned, the concentrations of U and Th were measured to be:

- gU/gH2O: $(3.64 \pm 0.74_{(stat)} + 1.28_{(syst)} - 0.99_{(syst)}) \times 10^{-15}$
- gTh/gH2O: $(3.08 \pm 3.22_{(stat)} + 1.60_{(syst)} - 5.00_{(syst)}) \times 10^{-16}$

This is about an order of magnitude improvement over the period before the cover gas was commissioned, which implies that water analyses physics results can be improved with this steady, low background water data. Furthermore, this provided information on the cleanliness of the water prior to liquid scintillator fill.

An "invisible" neutron decay search was performed on the published dataset with improvements to the fiducial volume optimization. In addition, the energy systematics were evaluated by floating them as parameters in the fit instead of using "shift-and-refit". The published lower limit for "invisible" neutron decay was 2.5×10^{29} years. The results of the analysis presented in this thesis leads to a new world-leading limit of 6.9×10^{29} years, an improvement over the published results and previous world-leading value of 5.8×10^{29} years. A sensitivity study was also done for the low background dataset which found the median 90% lower limit on the "invisible" neutron decay to be 1.57×10^{30} years. Therefore, we expect a further factor of 2 improvement on the current results.

Looking ahead to the tellurium phase, a methodology was developed utilizing XRF to quantify the concentration of tellurium in the scintillator cocktail. This was instrumental for tellurium loading and compatibility studies. Since the work presented here, more work to characterize the XRF machine at SNOLAB has been done, making this technique one of the key quality control tests for tellurium loading.

Bibliography

[1] J. Jackson, *Classical Electrodynamics*, Physics textbook (John Wiley and Sons, Inc., 1999), 3rd ed., ISBN 0-471-30932-X.

[2] A. Borrelli, Annalen der Physik **530**, 1700454 (2018), https://onlinelibrary.wiley.com/doi/pdf/10.1002/andp.201700454.

[3] P. W. Higgs, Phys. Rev. Lett. **13**, 508 (1964), URL https://link.aps.org/doi/10.1103/PhysRevLett.13.508.

[4] F. Englert and R. Brout, Phys. Rev. Lett. **13**, 321 (1964), URL https://link.aps.org/doi/10.1103/PhysRevLett.13.321.

[5] S. Chatrchyan, V. Khachatryan, A. Sirunyan, A. Tumasyan, W. Adam, E. Aguilo, T. Bergauer, M. Dragicevic, J. Er, C. Fabjan, et al., Physics Letters B **716**, 30 (2012), ISSN 0370-2693, URL http://www.sciencedirect.com/science/article/pii/S0370269312008581.

[6] D. Kazakov, CERN Yellow Reports: School Proceedings **3**, 83 (2018), ISSN 2519-805X, URL https://publishing.cern.ch/index.php/CYRSP/article/view/827.

[7] P. D. Group, P. A. Zyla, R. M. Barnett, J. Beringer, O. Dahl, D. A.

Dwyer, D. E. Groom, C. J. Lin, K. S. Lugovsky, E. Pianori, et al., Progress of Theoretical and Experimental Physics **2020** (2020), ISSN 2050-3911, 083C01, https://academic.oup.com/ptep/article-pdf/2020/8/083C01/33653179/ptaa104.pdf, URL https://doi.org/10.1093/ptep/ptaa104.

[8] J. Heeck and V. Takhistov, Phys. Rev. D **101**, 015005 (2020), URL https://link.aps.org/doi/10.1103/PhysRevD.101.015005.

[9] K. Babu et al., in *Community Summer Study 2013: Snowmass on the Mississippi* (2013), 1311.5285.

[10] P. Langacker, Physics Reports **72**, 185 (1981), ISSN 0370-1573, URL http://www.sciencedirect.com/science/article/pii/0370157381900594.

[11] K. Hagino and M. Nirkko, Journal of Physics G: Nuclear and Particle Physics **45**, 105105 (2018), URL https://doi.org/10.1088%2F1361-6471%2Faadeb1.

[12] J. M. Cline, in *Les Houches Summer School - Session 86: Particle Physics and Cosmology: The Fabric of Spacetime* (2006), hep-ph/0609145.

[13] R. N. Mohapatra and A. Pérez-Lorenzana, Phys. Rev. D **67**, 075015 (2003), URL https://link.aps.org/doi/10.1103/PhysRevD.67.075015.

[14] Y. Suzuki, Y. Fukuda, K. Hirata, K. Inoue, T. Ishida, T. Kajita, K. Kihara, M. Nakahata, K. Nakamura, A. Sakai, et al., Physics Letters B **311**, 357 (1993), ISSN 0370-2693, URL http://www.sciencedirect.com/science/article/pii/0370269393905823.

[15] M. Tanaka, K. Abe, C. Bronner, Y. Hayato, M. Ikeda, S. Imaizumi, H. Ito, J. Kameda, Y. Kataoka, Y. Kato, et al. (The Super-Kamiokande Collaboration), Phys. Rev. D **101**, 052011 (2020), URL https://link.aps.org/doi/10.1103/PhysRevD.101.052011.

[16] J. Hisano, Tech. Rep. hep-ph/0004266, KEK, Tsukuba (2000), URL https://cds.cern.ch/record/436174.

[17] F. del Aguila and A. Mendez, Z. Phys. C **13**, 347 (1982).

[18] J. Hewett et al., in *Community Summer Study 2013: Snowmass on the Mississippi* (2014), 1401.6077.

[19] M. Miura, Nuclear and Particle Physics Proceedings **273-275**, 516 (2016), ISSN 2405-6014, 37th International Conference on High Energy Physics (ICHEP), URL http://www.sciencedirect.com/science/article/pii/S2405601415005659.

[20] H. Ejiri, Phys. Rev. C **48**, 1442 (1993), URL https://link.aps.org/doi/10.1103/PhysRevC.48.1442.

[21] M. Anderson and et al. (The SNO+ Collaboration), Phys. Rev. D **99**, 032008 (2019), URL https://link.aps.org/doi/10.1103/PhysRevD.99.032008.

[22] J. Boger, R. Hahn, J. Rowley, A. Carter, B. Hollebone, D. Kessler, I. Blevis, F. Dalnoki-Veress, A. DeKok, J. Farine, et al., Nuclear Instruments and Methods in Physics Research Section A: Accelerators, Spectrometers, Detectors and Associated Equipment **449**, 172 (2000), ISSN 0168-9002, URL http://www.sciencedirect.com/science/article/pii/S0168900299014692.

[23] S. Kliewer, *Muons*, https://cosmic.lbl.gov/SKliewer/Cosmic_Rays/Muons.htm.

[24] J. Hubbell and S. Seltzer, *X-Ray Mass Attenuation Coefficients*, https://physics.nist.gov/PhysRefData/XrayMassCoef/ComTab/water.html.

[25] A. Mastbaum, E. Marzec, and R. Bonventre, *Electronics overview*, SNO+ Internal Document-3769 (2016).

[26] D. F. Cowen, T. Ekenberg, J. R. Klein, F. M. Newcomer, R. Van Berg, R. G. Van de Water, P. Wittich, A. Biman, and R. L. Stevenson, IEEE Transactions on Nuclear Science **42**, 925 (1995).

[27] R. Knapik, R. Bonventre, and T. Shokair, Nuclear Physics B - Proceedings Supplements **229-232**, 523 (2012), ISSN 0920-5632, neutrino 2010, URL http://www.sciencedirect.com/science/article/pii/S0920563212003775.

[28] J. Klein and et al, *The sno trigger system* (1997), URL https://snopl.us/detector/documents/trigger.pdf.

[29] R. Knapik, *Sno+ electronics*, SNO+ Internal Document-733 (2010).

[30] E. P. Cherenkova, Nuclear Instruments and Methods in Physics Research Section A: Accelerators, Spectrometers, Detectors and Associated Equipment **595**, 8 (2008), ISSN 0168-9002, rICH 2007, URL http://www.sciencedirect.com/science/article/pii/S0168900208009297.

[31] S. N. Ahmed, A. E. Anthony, E. W. Beier, A. Bellerive, S. D. Biller, J. Boger,

M. G. Boulay, M. G. Bowler, T. J. Bowles, S. J. Brice, et al. (SNO Collaboration), Phys. Rev. Lett. **92**, 102004 (2004), URL https://link.aps.org/doi/10.1103/PhysRevLett.92.102004.

[32] *Operating Experience with Nuclear Power Stations in Member States in 2015*, Operating Experience with Nuclear Power Stations in Member States (CD-ROM) (INTERNATIONAL ATOMIC ENERGY AGENCY, Vienna, 2016), ISBN 978-92-0-155016-3, URL https://www.iaea.org/publications/11091/operating-experience-with-nuclear-power-stations-in-member-states-in-2015.

[33] F. Capozzi, E. Lisi, A. Marrone, D. Montanino, and A. Palazzo, Nuclear Physics B **908**, 218 (2016), ISSN 0550-3213, neutrino Oscillations: Celebrating the Nobel Prize in Physics 2015, URL http://www.sciencedirect.com/science/article/pii/S0550321316000602.

[34] W. P. Group, *Water phase unidoc*, https://github.com/snoplus/Water-Phase-Unidoc.

[35] M. R. Anderson, S. Andringa, M. Askins, D. J. Auty, N. Barros, F. Barão, R. Bayes, E. W. Beier, A. Bialek, S. D. Biller, et al. (The SNO+ Collaboration), Phys. Rev. C **102**, 014002 (2020), URL https://link.aps.org/doi/10.1103/PhysRevC.102.014002.

[36] J. N. Bahcall, A. M. Serenelli, and S. Basu, The Astrophysical Journal **621**, L85 (2005), URL https://doi.org/10.1086%428929.

[37] A. Bellerive, J. Klein, A. McDonald, A. Noble, and A. Poon, Nuclear Physics B **908**, 30 (2016), ISSN 0550-3213, neutrino Oscillations: Celebrating the

Nobel Prize in Physics 2015, URL http://www.sciencedirect.com/science/article/pii/S0550321316300736.

[38] S. Moriyama and et al., Journal of Physics: Conference Series **888**, 012005 (2017), URL https://doi.org/10.1088%2F1742-6596%2F888%2F1%2F012005.

[39] M. Anderson and et al. (SNO+ Collaboration), Phys. Rev. D **99**, 012012 (2019), URL https://link.aps.org/doi/10.1103/PhysRevD.99.012012.

[40] D. Szam, *Solar neutrino chain*, URL https://commons.wikimedia.org/w/index.php?curid=23213257.

[41] S. Andringa and et al., Advances in High Energy Physics **6194250** (2016), URL https://www.hindawi.com/journals/ahep/2016/6194250/.

[42] J. B. Birks, *The Theory and Practice of Scintillation Counting* (Pergamon Press Ltd, 1964).

[43] G. F. Knoll, *Radiation Detection and Measurement* (John Wiley and Sons, Inc., 2000), 3rd ed.

[44] M. Tanabashi, K. Hagiwara, K. Hikasa, K. Nakamura, Y. Sumino, F. Takahashi, J. Tanaka, K. Agashe, G. Aielli, C. Amsler, et al. (Particle Data Group), Phys. Rev. D **98**, 030001 (2018), URL https://link.aps.org/doi/10.1103/PhysRevD.98.030001.

[45] M. Agostini, K. Altenmüller, S. Appel, V. Atroshchenko, Z. Bagdasarian, D. Basilico, G. Bellini, J. Benziger, D. Bick, G. Bonfini, et al. (Borexino Collaboration), Phys. Rev. D **101**, 012009 (2020), URL https://link.aps.org/doi/10.1103/PhysRevD.101.012009.

[46] A. Gando and et al. (KamLAND collaboration), Nature Geoscience **4** (2011).

[47] M. C. Chen, in *Neutrino Geophysics: Proceedings of Neutrino Sciences 2005*, edited by S. T. Dye (Springer New York, New York, NY, 2007), pp. 221–228, ISBN 978-0-387-70771-6.

[48] V. Brdar, M. Lindner, and X.-J. Xu, Journal of Cosmology and Astroparticle Physics **2018**, 025 (2018), URL https://doi.org/10.1088%2F1475-7516%2F2018%2F04%2F025.

[49] *Are neutrinos their own antiparticle?*, URL https://next.ific.uv.es/next/experiment/physics.html.

[50] K. Alfonso, D. R. Artusa, F. T. Avignone, O. Azzolini, M. Balata, T. I. Banks, G. Bari, J. W. Beeman, F. Bellini, A. Bersani, et al. (CUORE Collaboration), Phys. Rev. Lett. **115**, 102502 (2015), URL https://link.aps.org/doi/10.1103/PhysRevLett.115.102502.

[51] T. Kaptanoglu, *Neutrinoless double beta decay with sno+* (2019).

[52] O. Cremonesi, Nuclear Physics B - Proceedings Supplements **118**, 287 (2003), ISSN 0920-5632, URL http://www.sciencedirect.com/science/article/pii/S0920563203013318).

[53] S. M. Bilenky, A. Faessler, T. Gutsche, and F. Šimkovic, Phys. Rev. D **72**, 053015 (2005), URL https://link.aps.org/doi/10.1103/PhysRevD.72.053015.

[54] A. LaTorre, *Measurement of the Trigger Efficiency in SNO+*, Internal Document DocDB-4723-v3.

[55] M. Anderson and et al. (SNO+ Collaboration), *RAT*, https://github.com/snoplus/rat (2020).

[56] R. Brun and F. Rademakers, Nucl. Instrum. Meth. A **389**, 81 (1997), URL https://github.com/root-project/root/.

[57] W. Verkerke and D. P. Kirkby, eConf **C0303241**, MOLT007 (2003), physics/0306116.

[58] H. M. O'Keeffe, Ph.D. thesis, Lincoln College, University of Oxford (2008).

[59] Fatemighomi, Nasim, in *Canadian Association of Physicists Congress - Session F1-5: Future of Cosmic Frontier: Dark Matter III and Dark Energy* (2014), URL https://indi.to/56rbJ.

[60] N. Fatemighomi, R. Ford, C. Jillings, and O. Li, *LAB Cover Gas System Design Specification*, Internal Document DocDB-1960-v3.

[61] N. Fatemighomi, *Cover Gas Commissioning Report, Operational Manual* , Internal Document DocDB-2918.

[62] A. Bialek, *Cover Gas System Status* , Internal Document DocDB-5177.

[63] B. Aharmim, S. N. Ahmed, A. E. Anthony, E. W. Beier, A. Bellerive, M. Bergevin, S. D. Biller, J. Boger, M. G. Boulay, M. G. Bowler, et al. (SNO Collaboration), Phys. Rev. C **72**, 055502 (2005), URL https://link.aps.org/doi/10.1103/PhysRevC.72.055502.

[64] E. W. Beier, *Isotropy classifier*, Internal Document DocDB-2835-v2.

[65] M. Askins, *Nucleon decay box optimization*, Internal Document DocDB-5358.

[66] L. Lebanowski and M. Luo, *Energy calibration and systematics with the n16 source*, Internal Document DocDB-5083-v11.

[67] R. Bayes, *Beta14 plot from central n16*, Internal Document DocDB-5086.

[68] T. Kaptanoglu and A. LaTorre, *Proposal for applying the trigger efficiency*, Internal Document DocDB-5059-v5.

[69] E. Leming, *Position and direction systematics*, Internal Document DocDB-5252.

[70] A. J. Wright, Private Communication.

[71] D. Chauhan, *Water assay results*, Internal Document DocDB-4911-v1.

[72] N. Fatemi-Ghomi, *Water assay update*, Internal Document DocDB-5720.

[73] V. Lozza, *Status of background water phase*, Internal Document DocDB-5372-v13/0331-0320-Progress.

[74] V. Lozza, *Summary of different timebins*, Internal Document DocDB-5144.

[75] I. Lam, *Internal backgrounds - plots and numbers for review*, SNO+ Internal Document-6511-v3 (2020).

[76] B. Aharmim, S. N. Ahmed, A. E. Anthony, N. Barros, E. W. Beier, A. Bellerive, B. Beltran, M. Bergevin, S. D. Biller, K. Boudjemline, et al. (SNO Collaboration), Phys. Rev. C **88**, 025501 (2013), URL https://link.aps.org/doi/10.1103/PhysRevC.88.025501.

[77] H. Georgi and S. L. Glashow, Phys. Rev. Lett. **32**, 438 (1974), URL https://link.aps.org/doi/10.1103/PhysRevLett.32.438.

[78] A. Bueno, A. J. Melgarejo, S. Navas, Z. Dai, Y. Ge, M. Laffranchi, A. Meregaglia, and A. Rubbia, Journal of High Energy Physics **2007**, 041 (2007), URL https://doi.org/10.1088%2F1126-6708%2F2007%2F04%2F041.

[79] S. Raby, *Proton decay* (2002), hep-ph/0211024.

[80] L. Montanet et al. (Particle Data Group), Phys. Rev. D **50**, 1173 (1994).

[81] T. Araki, S. Enomoto, K. Furuno, Y. Gando, K. Ichimura, H. Ikeda, K. Inoue, Y. Kishimoto, M. Koga, Y. Koseki, et al. (KamLAND Collaboration), Phys. Rev. Lett. **96**, 101802 (2006), URL https://link.aps.org/doi/10.1103/PhysRevLett.96.101802.

[82] V. Tretyak, V. Denisov, and Y. Zdesenko, JETP Lett. **79**, 106 (2004), nucl-ex/0401022.

[83] J. N. Bahcall, *Neutrino Astrophysics* (Cambridge University Press, 1989), 1st ed.

[84] C. Andreopoulos et al., Nucl. Instrum. Meth. A **614**, 87 (2010), 0905.2517.

[85] T. Kaptanoglu, *Atmospheric Background Estimate For SNO+ Nucleon Decay*, Internal Document DocDB-5039 (2018).

[86] Y.-C. Chen, *Density Estimation: Histogram and Kernel Density Estimator*, https://faculty.washington.edu/yenchic/18W_425/Lec6_hist_KDE.pdf (2018).

[87] K. Cranmer, Computer Physics Communications **136**, 198 (2001),

ISSN 0010-4655, URL http://www.sciencedirect.com/science/article/pii/S0010465500002435.

[88] G. J. Feldman and R. D. Cousins, Phys. Rev. D **57**, 3873 (1998).

[89] F. James and M. Roos, CERN D506 MINUIT (1989).

[90] M. Askins and I. Lam, *Low Background Nucleon Decay Unidoc*, SNO+ Internal Document in preparation (2020), URL https://www.overleaf.com/project/5eea7ee176cc680001061d6b.

[91] B. Krar, Private Communication.

[92] V. Lozza, *Water processing and production: Low background period*, Internal Document DocDB-6188-v13.

[93] Bruker, *Introduction to x-ray fluorescence analysis* (2016), URL https://www.bruker.com/products/x-ray-diffraction-and-elemental-analysis/x-ray-fluorescence/what-is-xrf.html.

[94] Amptek, *X-ray fluorescence(xrf): Understanding characteristic x-rays*, URL https://www.amptek.com/-/media/ametekamptek/documents/resources/characteristic_xrays.pdf.

[95] A. C. Thomson and D. Vaughan, *X-ray data booklet*, Lawrence Berkeley National Laboratory, URL https://xdb.lbl.gov/.

[96] F. St. Jacques and I. Lam, *Te Analysis Update*, Private communication (2018).

Appendix A

Best Fit Plots

This appendix contains the best fit plots of time bin 5 and the combined time bins 1,2,3 for the "invisible" neutron decay analysis.

A.1 Time bin 5

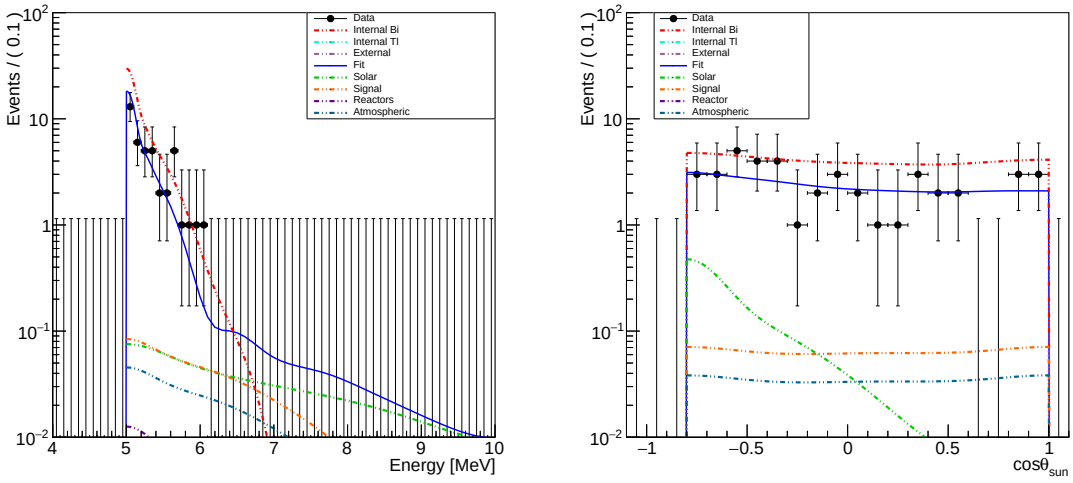

(a) Energy

(b) Solar angle

Figure A.1: Best-fit energy and solar angle spectra for time bin 5.

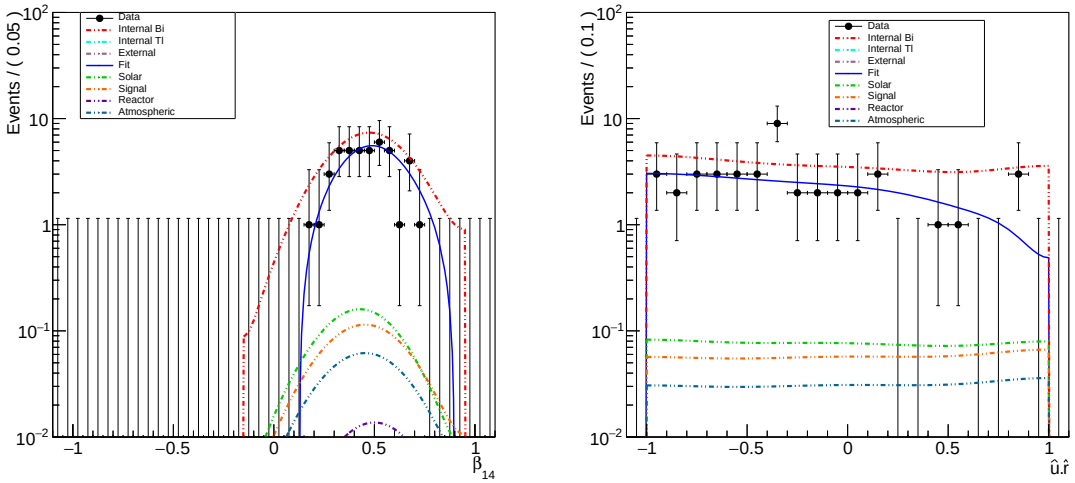

(a) Isotropy, β_{14} (b) Direction

Figure A.2: Best-fit isotropy and direction spectra for time bin 5.

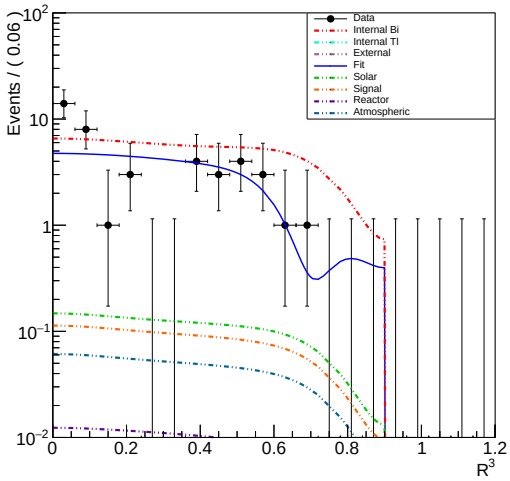

Figure A.3: Best-fit R^3 spectra for time bin 5.

A.2 Combined time bin 1,2,3

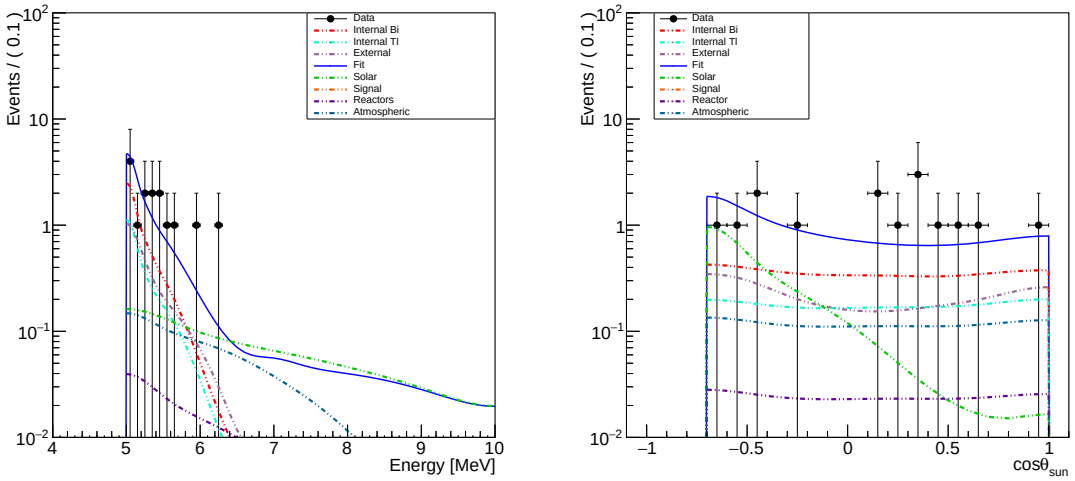

(a) Energy (b) Solar angle

Figure A.4: Best-fit energy and solar angle spectra for combined time bin 1,2,3.

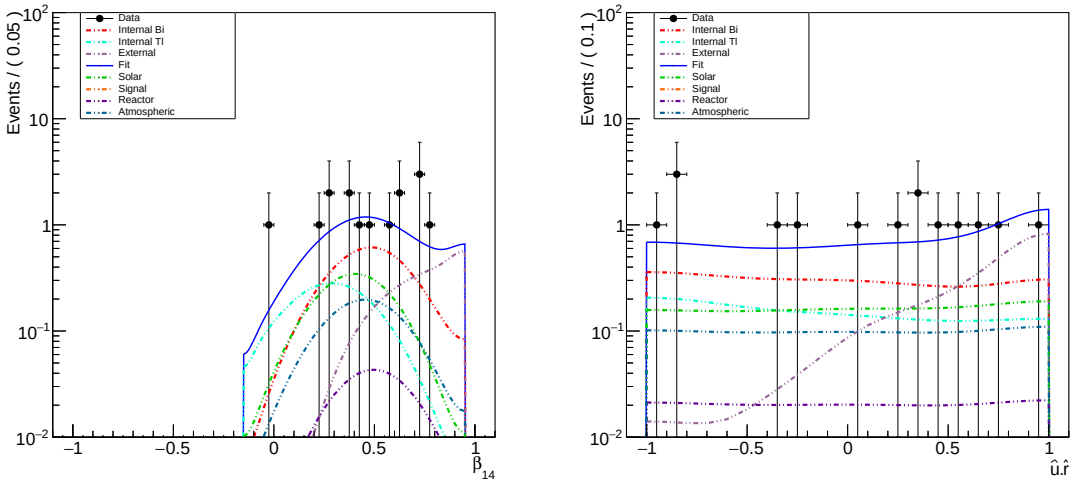

(a) Isotropy, β_{14} (b) Direction

Figure A.5: Best-fit isotropy and direction spectra for combined time bin 1,2,3.

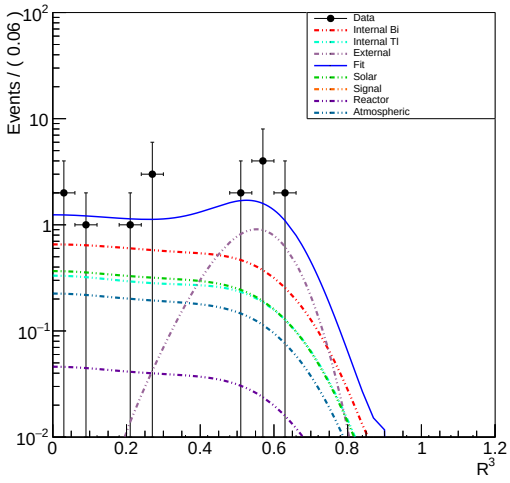

Figure A.6: Best-fit R^3 spectra for combined time bin 1,2,3.

Appendix B

Acronyms

ABS	acrylonitrate-butadiene-styrene
ADC	Analog to Digital Converter
AV	Acrylic Vessel
BEH	Brout-Englert-Higgs
CERN	Conseil europé en pour la recherche nucléaire
CTC	Crate Trigger Card
DB	DaughterBoard
DCR	Deck Clean Room
ECA	Electronics CAlibration
ELLIE	Embedded LED/Laser Light Injection Entity
ES	Elastic Scattering
FEC	Front-End-Card
GEANT	GEometry ANd Tracking
GTID	Global Trigger ID
GUT	Grand Unified Theory
IBD	Inverse Beta Decay

ITR	In Time Ratio
LAB	Linear Alkylbenzene
MC	Monte Carlo
MTC/A	Analog Master Trigger Card
MTC/D	Digital Master Trigger Card
ND	Nucleon Decay
nhits	number of PMT hits of an event
OCA	Optical CAlibration
PCA	PMT CAlibration
PDF	Probability Density Function
PMT	PhotoMultiplier Tube
PSUP	PMT SUPport structure
RAT	Reactor Analysis Tools
ROI	Region-Of-Interest
SNe	SuperNovae
SNO	Sudbury Neutrino Observatory
SUSY	SUper-SYmmetry
TNC	Threaded Neill-Concelman
TOE	Theory of Everything
UPW	Ultra Pure Water
XRF	X-Ray Fluorescence